SPIM

Thèse de Doctorat

école doctorale **sciences pour l'ingénieur et microtechniques**

UFC UNIVERSITÉ DE FRANCHE-COMTÉ

Contribution à la modélisation et au contrôle d'une matrice d'AFM

Hui HUI

SPIM

Thèse de Doctorat

UFC

école doctorale **sciences pour l'ingénieur et microtechniques**

UNIVERSITÉ DE FRANCHE-COMTÉ

N° | X | X | X |

THÈSE présentée par

Hui HUI

pour obtenir le

Grade de Docteur de
l'Université de Franche-Comté

Spécialité : **Mécanique, génie mécanique, génie civil**

Contribution à la modélisation et au contrôle d'une matrice d'AFM

Unité de Recherche :
FEMTO-ST, Département Temps-Fréquence, Université de Franche-Comté

Soutenue le 6 mai 2013 devant le Jury :

MANUEL COLLET	Président	Professeur de Université de Besançon
DAPENG CHEN	Rapporteur	Professeur de Chinese Academy of Sciences, Chine
ERIC COLINET	Rapporteur	HDR, CEA-LETI, Grenoble, France
MURTI V. SALAPAKA	Rapporteur	Professeur de Université du Minnesota, USA
MICHEL LENCZNER	Directeur de Thèse	Professeur des Universités, Université de Technologie Belfort-Montbéliard
SCOTT COGAN	Examinateur	HDR, Université de Besançon
ANDRÉ MEISTER	Examinateur	Ingénieur, Centre Suisse d'Electronique et de Microtechnique, Neuchâtel, Suisse
ABU SEBASTIAN	Examinateur	Ingénieur, IBM Zürich Research Laboratory, Zurich, Suisse

Département Temps-Fréquence
UFR ST Sciences et Techniques

École doctorale SPIM Besançon

Contribution to a Simulator of Arrays of Atomic Force Microscopes

Dissertation

Submitted in Partial Fulfillment of the Requirements
for the Degree of Doctor of Ph.D. in Mechanical Engineering

6 May 2013

Doctoral School of University of Franche-Comté,

By

Hui HUI

Doctoral Committee:

President :	Professor MANUEL COLLET
Reviewers :	Professor MURTI V. SALAPAKA H.D.R. ERIC COLINET Professor DAPENG CHEN
Examiners :	Professor MICHEL LENCZNER Professor MANUEL COLLET Dr. SCOTT COGAN Dr. ANDRÉ MEISTER Dr. ABU SEBASTIAN

INSTITUT FEMTO-ST

ABSTRACT

In this dissertation, we establish a two-scale model both for one-dimensional and two-dimensional Cantilever Arrays in elastodynamic operating regime with possible applications to Atomic Force Microscope (AFM) Arrays. Its derivation is based on an asymptotic analysis for thin elastic structures, a two-scale approximation and a scaling used for strongly heterogeneous media homogenization. We complete the theory of two-scale approximation for fourth order boundary value problems posed in thin periodic domains connected in some directions only. Our model reproduces the global dynamics as well as each of the cantilever motion. For the sake of simplicity, we present a simplified model of mechanical behavior of large cantilever arrays with decoupled rows in the dynamic operating regime. Since the supporting bases are assumed to be elastic, cross-talk effect between cantilevers is taken into account. The verification of the model is carefully conducted. We explain not only how each eigenmode is decomposed into products of a base mode with a cantilever mode but also the method used for its discretization, and report results of its numerical validation with full three-dimensional Finite Element simulations. We show new tools developed for Arrays of Microsystems and especially for AFM array design. A robust optimization toolbox is interfaced to aid for design before the microfabrication process. A model based algorithm of static state estimation using measurement of mechanical displacements by interferometry is presented. We also synthesize a controller based on Linear Quadratic Regulator (LQR) methodology for a one-dimensional cantilever array with regularly spaced actuators and sensors. With the purpose of implementing the control in real time, we propose a semi-decentralized approximation that may be realized by an analog distributed electronic circuit. More precisely, our analog processor is made by Periodic Network of Resistances (PNR). The control approximation method is based on two general concepts, namely on functions of operators and on the Dunford-Schwartz representation formula. This approximation method is extended to solve a robust H_∞ filtering problem of the coupled cantilevers for time-invariant system with random noise effects.

Keywords: Cantilever arrays, Two-scale modeling, Homogenization, Model verification, Optimization design, Interferometry measurements, Semi-decentralized control, Functional calculus, Cauchy integral formula

Résumé

Dans cette thèse, nous établissons un modèle à deux échelles à la fois pour des matrices de cantilevers unidimensionnels et bidimensionnels en régime de fonctionnement élastodynamique avec des applications possibles aux réseaux de microscopes à force atomique (AFM). Son élaboration est basée sur une analyse asymptotique pour les structures minces élastiques, une approximation à deux échelles et une mise à l'échelle utilisée pour l'homogénéisation des milieux fortement hétérogènes. Nous complétons la théorie de l'approximation à deux échelles pour les problèmes aux limites du quatrième ordre posés dans des domaines minces périodiques connexes seulement dans certaines directions. Notre modèle reproduit la dynamique globale du support ainsi que les mouvements locaux des cantilevers. Pour simplifier la suite du travail, nous concentrons nos travaux à l'étude de matrices de leviers constituées de lignes découplées en régime dynamique. Comme le support des leviers est élastique, l'effet du couplage entre levier est pris en compte. La vérification du modèle est soigneusement réalisée. Nous montrons que chaque mode propre peut être décomposé en produits d'un mode de base avec un mode de levier. Nous présentons une méthode de discrétisation du modèle et effectuons sa vérification numérique en la comparant avec des résultats de simulation par éléments finis du problème d'élasticité tridimensionnel. Par ailleurs, nous avons élaboré de nouveaux outils d'aide à la conception de réseaux d'AFM. Une boîte à outils d'optimisation robuste est interfacée avec le modèle permettant d'optimiser un design avant micro-fabrication. Un algorithme d'estimation de l'état statique combinant la mesure de déplacements mécaniques par interférométrie et le modèle a été introduit. Nous avons également synthétisé un régulateur quadratique linéaire (LQR) pour un réseau de cantilevers en mode dynamique comprenant actionneurs et capteurs régulièrement espacées. Dans le but de mettre en œuvre le contrôle en temps réel, nous proposons une approximation semi-décentralisée qui peut être réalisé par un circuit électronique distribué analogique. Plus précisément, notre processeur analogique peut être réalisé par un réseau périodique de résistances (PNR). La méthode d'approximation de commande est basée sur deux concepts généraux, à savoir sur un calcul fonctionnel (c'est-à-dire des fonctions d'opérateurs) et sur la formule de représentation d'une fonction d'opérateur de Dunford-Schwartz. Cette méthode d'approximation est étendue pour la résolution d'un problème de filtrage optimal robuste de type H_∞ de la dynamique d'un réseau de leviers couplés avec sources aléatoires de bruit.

Mots-clés: Matrice de levier, modélisation à deux échelles, homogénéisation, vérification de modèle, conception par optimisation robuste, mesures d'interférométrie, contrôle semi-décentralisé, calcul fonctionnel, formule intégrale de Cauchy.

Acknowledgment

I would like to express the deepest appreciation to my advisor, Professor Michel LENCZNER, for his support, guidance, and supervision. His knowledge, dedication, enthusiasm, patience, encouragement, and personality have made my graduate experience at University of Franche-Comté rewarding and indeed unforgettable. As a Chinese saying goes: *"Even if someone is your teacher for only a day, you should regard him like your father for the rest of your life."* I would like to sincerely thank the reviewers of my dissertation: Professor Murti V. SALAPAKA, Professor Dapeng CHEN and Dr. Eric COLINET, for their invaluable comments, suggestions of my work. I would like to thank my committee chairman: Professor Manuel COLLET, for his kind service and comments in my dissertation defense committee. I am also grateful to my committee members: Dr. Scott COGAN, Dr. André MEISTER and Dr. Abu SEBASTIAN, for their questions and discussions about my research work.

Special thanks to Dr. Scott COGAN, it was an excellent experience to work with him. I would like to thank Mr. Nicolas RATIER, for his contribution to my dissertation. I am also grateful to Dr. Mélanie FAVRE, Dr. Thomas OVERSTOLZ for their cooperation in aspects of design optimization and interferometric measurements. I want to express my appreciation to Raphaël COUTURIER and Stéphane DOMAS for their help with algorithm of interferometric measurements. I would like to extend my special thanks to my colleagues: Dr. Youssef YAKOUBI, PhD. Bin YANG, PhD. Raj Narayan DHARA and PhD. Thi Trang NGUYEN, for their helpful discussions with mathematical problems, simulation and control issues that I encountered in my research work.

I would like to thank my colleagues for providing me a lot of helps in my years at Institute of FEMTO-ST, Time frequency department. Special thanks to the secretaries Mrs. Fabienne CORNU from Time frequency department, Ms. Isabelle GABET and Ms. Sandrine FRANCHI of our Lab., for helping me in work contract issues. I am also thankful to the secretaries of doctoral school of University of Franche-Comté for providing me help with registration and preparation of my defense. Thanks to my friends at University of Franche-Comté and Institute of FEMTO-ST have made my study and life enjoyable and memorable.

I would like to acknowledge the financial support by China Scholarship Council, and European Territorial Cooperation Programme INTERREG IV A France-Switzerland 2007-2013. Thanks to Northwestern Polytechnical University in China, and Institute of FEMTO-ST and University of Franche-Comté in France for giving me opportunity to work on my dissertation. I am also grateful to Centre Suisse d'Electronique et de Microtechnique (CSEM), and Mésocentre de calcul de Franche-Comté, and DigitalSurf for contributing to my dissertation. I am extremely grateful to Professor Yikai SHI for his help. Special thanks to Professor

Qingchuan ZHANG, for his comments and suggestions of my dissertation.

Last but the least, I want to give my deepest grateful to my parents for supporting and encouraging me to get through all these years, and for their endless love. Thanks to my brother for supporting and being proud of me. I would also like to thank my wife Dr. Fangfang BU, and her family for their supporting me to finish my dissertation over last two years. I am grateful to my wife for sharing her time with me in preparing and writing this dissertation. Again, I am thankful to everyone who have contributed to this dissertation.

To my parents
and my wife

TABLE OF CONTENTS

List of Figures

List of Tables

Main Notations and Abbreviations

ℓ_C^0	The cantilever width in the reference cell, page 10
ϵ	The inverse of dilatation of any cell, page 8
$\gamma_{R,O}$	The tip-object interface, page 13
λ^A	The eigenvalue of system, page 16
λ^B	The macroscopic eigenvalue of base, page 17
λ^C	The microscopic eigenvalue of cantilever, page 17
$\mathcal{L}^B$	The linear operator, page 12
μ	The array size, page 8
ν	Poisson coefficient, page 88
ω	The filled rectangle covering the full array, page 8
$\overline{\widehat{u}}$	The inverse two-scale transform applied to two-scale transform of u, page 9
$\overline{u}^A$	The approximation of u in the physical system, page 9
$\overline{v}$	The approximated inverse for the two-scale transform of v , page 8
ψ^A	The eigenvector of system, page 16
ρ^B	The effective surface mass of base, page 10
$\sigma_{\alpha\beta}$	The plane stresses, page 88
ε	The cell size, page 8
ε^*	The ratio of the cell size ε, page 8
φ^B	The macroscopic eigenvector of base, page 17

φ^C The microscopic eigenvector of cantilever, page 17

$\widehat{\overline{v}}$ The two-scale transform applied to inverse two-scale transform of v, page 9

$\widehat{u}^\epsilon$ The two-scale transform of $u(x)$, defined for any $\widetilde{x}$ and for any y, page 8

$\widetilde{x}$ The two first components of moments (x_1, x_2) of x, page 9

$\widetilde{y}$ The two first components of moments (y_1, y_2) of y, page 9

ζ The tip-object friction coefficient, page 13

E Young modulus, page 88

E^C The cantilever elastic modulus, page 12

f^B The base effective load per unit area, page 13

F^{C0} The load per unit length of cantilevers, page 10

F^C The cantilever two-scale load per unit area times area in $\omega \times \widetilde{Y}_C$, page 13

F^D The two-scale load corresponding to a periodic distribution of concentrated load applied at points $z^c = x^c + \epsilon y^0$, page 13

F^O The object two-scale load per unit area times volume, page 13

F^{R0} The vector comprised of effective forces and moments of rigid part, page 11

F^R The tip two-scale load per unit area times area in $\omega \times \widetilde{Y}_C$, page 13

G^C The cantilever two-scale moment per unit area times area in $\omega \times \widetilde{Y}_C$, page 13

G^D The two-scale moment corresponding to a periodic distribution of concentrated load applied at points $z^c = x^c + \epsilon y^0$, page 13

G^R The tip two-scale moment per unit area times volume in $\omega \times \widetilde{Y}_C$, page 13

g^B_α The the base effective moments about the plate section per unit area, page 13

h The thickness of plate, page 12

h_B The thickness of base, page 10

h_C The thickness of cantilever, page 10

I^C The second moment of cantilever section, page 12

J^R The matrix of moments of rigid part, page 11

M^B The shear force matrix in base, page 14

m^{C0} The linear mass density of cantilevers, page 10

M^C The shear force matrix in cantilevers, page 14

m^C The two-scale mass density in cantilever per unit area times area , page 13

n^B The number of base modes, page 23

n^C The number of cantilever modes, page 23

R^B The homogenized stiffness tensor of base, page 10

r^B The two-scale stiffness tensors per unit area in ω and per unit area in base $\widetilde{Y}_B$, page 12

r^{C0} The linear stiffness coefficient of cantilevers, page 10

r^C The two-scale stiffness tensors per unit area in ω and per unit area in cantilever $\widetilde{Y}_C$, page 12

R^P The thin plate stiffness per unit area, page 12

$s_{\alpha\beta}$ The strains, page 87

t The time variable, page 10

u^A The *two-scale approximation* of u, page 8

u^P The elastic displacements in the model of a Kirchhoff-Love thin plate interacting with objects, page 87

u_3^0 Initial transverse displacement, page 14

u_3^1 Initial velocity, page 14

u_3^A The third component of the vector of mechanical displacement, page 10

u_α^0 Initial lateral displacements in objects, page 14

u_α^1 Initial velocity in objects, page 14

x^c The center of the cell, page 8

y The coordinates vary in the unique reference cell, page 8

Y The filled reference cell, page 9

Y_B The base in a reference cell, page 9

Y_C The cantilever flexible part in a reference cell, page 9

Y_O The object in a reference cell, page 9

Y_R The cantilever rigid part in a reference cell, page 9

Y_S The mechanical device in a reference cell, page 9

z^{Fr} The two-scale friction coefficient at the two-scale tip-object interface $\omega \times \gamma_{R,O}$, page 13

AFM Atomic Force Microscope, page xii

FEM Finite Element Method, page xii

KCL Kirchhoff Current Law, page xii

LQG Linear Quadratic Gaussian, page xii

LQR Linear Quadratic Regulator, page xii

MAC Modal Assurance Criterion, page xii

PCA Principal Component Analysis, page xii

PDE Partial Differential Equation, page xii

PDF Probability Density Function, page xii

PNR Periodic Network of Resistances, page xii

VCCS Voltage Controlled Current Source, page xii

INTRODUCTION

Since its invention by [1], the Atomic Force Microscope (AFM) has opened new directions for a number of operations at the nanoscale with an impact in various sciences and technologies. A number of research laboratories are now developing large Arrays of AFM [2], [3] that can achieve imaging resolution similar to a single standalone AFM in parallel, (see Figure 1).

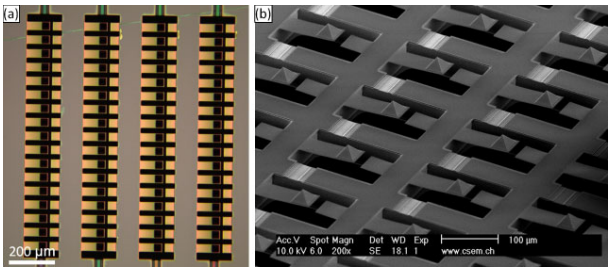

Figure 1: (a) optical image of a 4 $\times$17 probe array with SiN cantilevers anchored on parallel-beam base. The dark square at the end of each cantilever corresponds to the pyramidal shaped tip. (b) SEM images of a probe arrays with SiN cantilevers anchored on a gridlike base. Courtesy of Centre Suisse d'Electronique et de Microtechnique (CSEM), Neuchâtel Switzerland.

The state-of-the art system that employs an array of cantilever probes is the Millipede device from IBM [4],[5],[6] designed for data-storage, but again, a number of new architectures are emerging, see [7], [8], [9], [10], [11], [12], [13], [14], [15]. For nanolithography applications, a two-dimensional probe array is utilized for dip pen nanolithography [16] and nanoprobe maskless lithography is reported in [17].

The main limitation of AFM devices is their low speed of operation and their low reliability. Thus, modeling and model based control of AFM employing a single cantilever probe has found extensive attention, (see M. Napoli [18], S.M. Salapaka et al. [19], M. Sitti [20] for instance). To improve the performance of AFM, an H_∞ controller was employed in [21] and for AFM scanner in [22]. G. Schitter et al. [23] present a control strategy employing a model-based two-degrees-of freedom controller for high-speed topographical imaging. Regarding arrays, the group of

B. Bamieh, see [24] and the reference therein, has published a model of coupled cantilever arrays. It takes into account electrostatic coupling of cantilevers, and its derivation is phenomenological. In [25], both mechanical and electrostatic coupling neighboring cantilevers are modeled for an array of electrostatically actuated microcantilevers. In an array of cantilever probes, it is important to address the issue of cross-talk between cantilevers. Such cross-talk may have mechanical, thermal or electromagnetic origins and is an important effect to be considered while designing the array.

We propose a simplified model for the elastic behavior of large cantilever two-dimensional arrays. It extends results in [26] by taking into account the dynamical regime instead of the static regime, and is applicable to two-dimensional arrays instead of to one-dimensional arrays. Moreover, it takes into account the possible interaction between AFM tips and sample being interrogated. A similar analysis for one dimensional array ignoring the interaction between the tip and the sample is reported in [27]. The detailed derivation of the results in [28], not yet reported, follows from the results in this thesis.

Our method is mainly based on a homogenization technique applicable to strongly heterogeneous materials or systems expressed in the framework of two-scale convergence (or approximation) as introduced in works of M. Lenczner [29], [30] or in D. Cioranesco, A. Damlamian and G. Griso [31]. In a preliminary step, its derivation also uses the asymptotic method for thin structures developed by P.G. Ciarlet [32] and of P. Destuynder [33]. We remark that the choice of a method for the modeling of the periodic array is not straightforward. Here, a standard homogenization method is not applicable, where the local mechanical displacements of the moving parts may be of the same order as the displacements of the common support. Another aspect is that the lowest local eigenfrequencies of the moving parts are also in the same range of magnitude as those of the common supporting base. These features are usual in many microsystems arrays. However, the homogenization method was developed for typical continuum mechanics applications where the usual methods even with introduction of additional techniques has proven inadequate for modeling an array of micro-cantilever.

We review the main features of our simplified model. The array is comprised of cantilevers clamped in a common base, each possibly interacting with an object through its tip. We assume that the base is much stiffer than the cantilevers. This is expressed by saying that their stiffness have different asymptotic behaviors. The resulting model is composed of two evolution equations, one for the macroscopic behavior, related to the supporting base, and the other, at the microscopic level, which takes into account the cantilever dynamics. As required, their time scales are in the same range of magnitude and so are their mechanical displacements. We further assume that the tip is perfectly rigid, which is a commonly accepted

assumption. Then, we consider that the rigid objects interacting with tips have their own dynamics where the interaction is modeled via a friction law. All these assumptions yield the general model. As an introduction, we also present a slightly simpler model, referred to as the Simple Model, for which we have carried numerical simulations and validations. It does not include possible interaction with objects and it neglects the width effect in cantilevers.

For real-time control for arrays of microsystems like arrays of atomic force microscopes, micro-mirrors, or micro-membranes, we present a new approximation method based on the Simple Model. The microsystems are comprised of a very large number of units subjected to wanted or unwanted interactions (cross-talk effect). Achieving global control of such a system remains a challenging task. Here, we propose a computational strategy with very fine-grained computing processors allowing semi-decentralized exchanges, i.e. between neighbors only. We refer to this concept by using the term semi-decentralized architecture or computing.

In the past decade, a number of articles have focused on semi-decentralized distributed optimal control for systems with distributed actuators and sensors. Most of them deal with infinite length systems, see [34] and [35] for systems governed by partial differential equations, and [36] for discrete systems. In articles [37] and [38] authors have introduced an approximation, for optimal control design purposes, optimal control to a finite length beam endowed with a periodic distribution of piezoelectric sensors and actuators. Even-though here satisfactory results are obtained, it suffers from limitations of applying simple optimal control strategy, namely LQR, with simple control objective.

In [39] and [40], a comprehensive framework is introduced applicable to cover a large range of systems, with increased precision and robustness. The method is based on a general theory of optimal control for linear infinite dimensional systems. It does not require that all operators involved are functions of a same operator in the system. They only need to be functions of this operator up to some change of variables. Regarding precision of our method, the Taylor series approximating a function of an operator has been replaced using the integral Cauchy formula from functional calculus followed by a quadrature rule for the contour integral.

A first investigation for real-time vibration control of a one-dimensional cantilever array has been carried out in the LQR framework. In view of real-time control applications, we have derived a Semi-Decentralized Approximation of the controller based on the two mathematical concepts of functional calculus and Dunford-Schwartz representation formula, and formulated its realization through PNR, see [41]. This Semi-Decentralized approximation method can be extended to other linear control theories, such as Linear Quadratic Gaussian (LQG) and H_∞ control.

For real-time control of the cantilever arrays, one of the most important part

is the sensing system. Regarding sensing, in some cantilever arrays, the deflection of cantilever is measured by piezoresistive sensor integrated in the cantilever. In [42], a cantilever arrays equipped with piezoresistive sensors was employed in liquid environment. However, this approach suffers from the complexity of the microfabrication process of implementing the sensor in the cantilever. Additionally, the signal to noise ratio of piezoresistive arrays is limited due to the sensor noise. An interferometric readout method with imaging optics is provided in [43]. This approach does not suffer from optical cross-talk since the laser light reflected from one point on the cantilever is collected by only one pixel of the detector, and is independent of the direction the reflected laser beam. However, interferometric data processing requires heavy computation due to the large number of cantilevers, which represents a barrier to rapid operation. Thanks to a new approach for deflection estimation of cantilever arrays through interferometry measurement in quasi-static regime, it is turning into reality for real-time estimation and control of cantilever arrays in the dynamic regime.

This dissertation is organized as follows. In chapter 1, we start by shortly introducing the *Simple Model*. We then formulate the general model precisely. The model implementation is detailed both for two-dimensional and one-dimensional cantilever arrays. The Base/Cantilever displacement decomposition of the *Simple Model* is also discussed. Chapter 2 addresses the verification of the simple model. The eigenvalues and eigenmodes of the simple model are compared to those obtained by a direct three-dimensional Finite Element Method (FEM) both for one-dimensional and two-dimensional cantilever arrays. The verification of the model in static and dynamic regime is also presented. To meet the design requirements of AFM arrays, an optimization tool is introduced with an illustrative example. The interferometry measurement for AFM arrays is presented in chapter 3. The least square algorithm for phase computation is provided. In chapter 4, we present the semi-decentralized approximation method which is used LQR control and H_∞ filtering problem.

We draw our conclusion in chapter 5 with some remarks on future research work. A new software, AFMALab, for performing simulations for an array of cantilevers is presented in appendix B.

Chapter 1

TWO-SCALE MODEL FOR ARRAY OF CANTILEVERS

Contents

This chapter is devoted to the derivation of simple two-scale model in section 1.1.1, and general two-scale model in section 1.1.2 for a two-dimensional array of cantilevers. Each cantilever may be equipped with a rigid tip which can interact with the sample. For the simple model, we assume that there is no tip-sample interaction and the variation of the displacement in the width direction of cantilevers is negligible. All these assumptions are not present in the general model. Here, cantilevers can be modeled by a classical Euler-Bernoulli beam equation and the motion of the base is governed by a Kirchhoff-Love plate equation. The mathematical proofs of the two-scale approximation technique are detailed in a submitted paper [28].

In section 1.2, we show the model implementation both for two-dimensional and one-dimensional array of cantilevers. At the end of this chapter, we propose a Base/Cantilever displacement decomposition of the simple model.

1.1 Model Description

We consider a two-dimensional array of cantilevers, (see Figure 1.1). It is com-

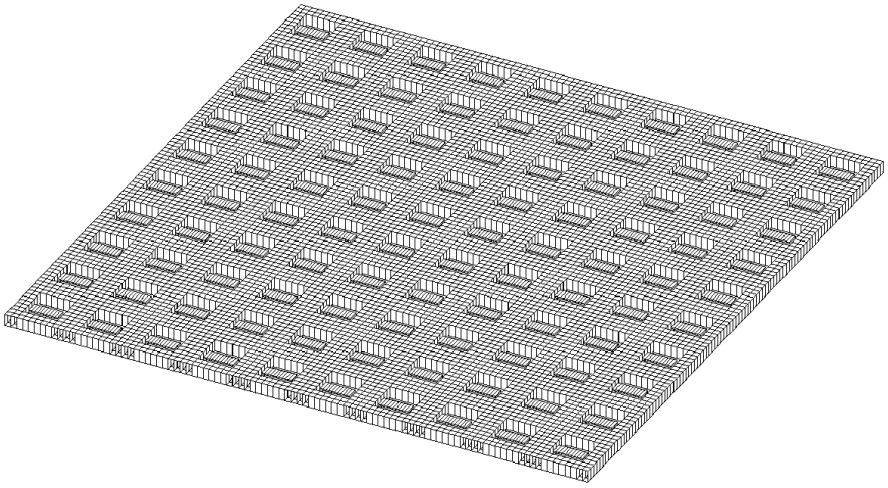

Figure 1.1: Array of Atomic Force Microscopes

prised of bases crossing the array in which cantilever are clamped. The bases are connected both in the x_1-direction and in the x_2-direction (see Figure 1.3 (a)), so they constitute a single common support clamped on its external boundary. Cantilevers may be equipped with a rigid tip, as in Atomic Force Microscopes.

The two-scale model derivation steps are illustrated in Figure 1.2. First, (a) the two-scale transform (also called the unfolding operator) and the two-scale approximation are successively applied to map a thin plate model in bending from the physical domain to a two-scale domain comprised of a reference cell and the macroscopic domains. Then, (b) the displacement variation in the width direction of cantilevers is neglected. In (c), base displacements in the reference cell are explicitly calculated and eliminated to yield the model in the so-called *two-scale domain* where the optimal control is implemented. Finally, (d) an inverse two-scale transform technique is applied to map the solutions in the two-scale domain back to the physical domain.

The whole array can be viewed as a periodic repetition of a same cell, in the two directions x_1 and x_2, (see Figure 1.3 (a)).

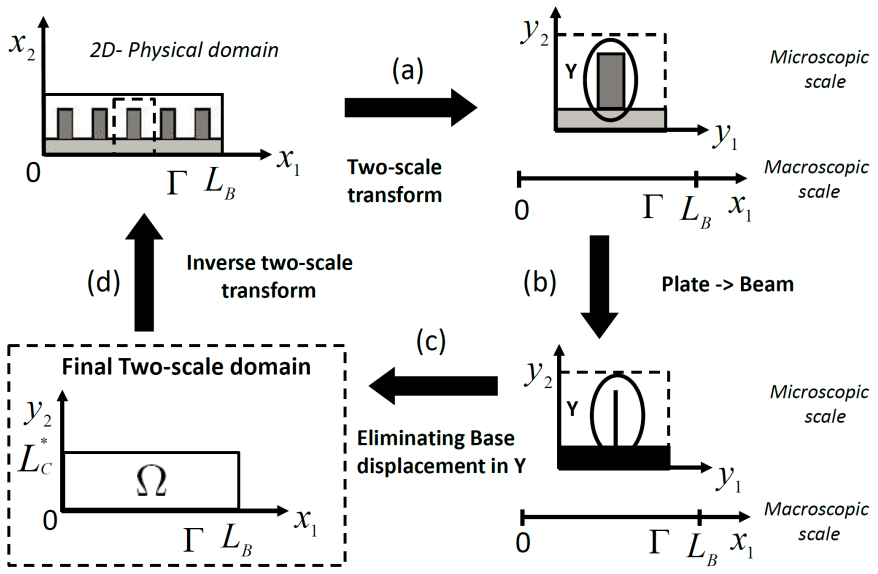

Figure 1.2: Two-scale transform and inverse two-scale transform in two-scale domain

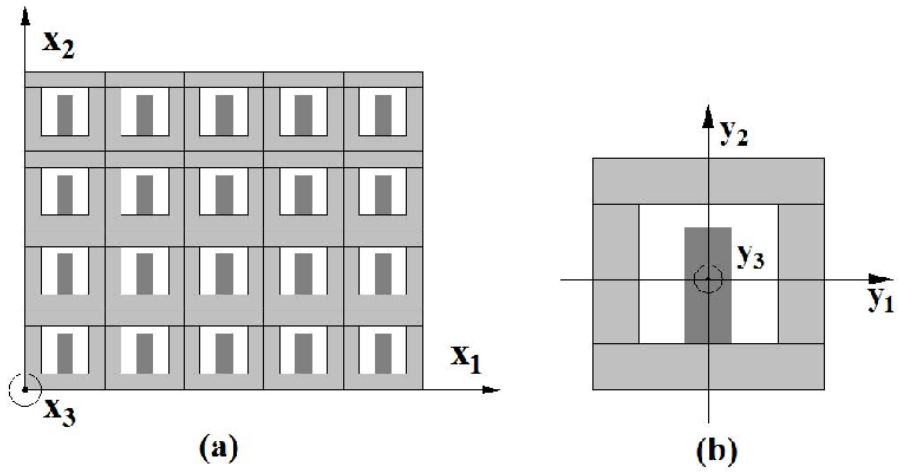

Figure 1.3: A two-dimensional view of (a) an array and (b) a cell

We suppose that the numbers of rows and columns of the array are sufficiently large, namely larger or equal to 10. The simplified model will be an approximation of the full model in the sense of small values of ε^*, the ratio of the cell size ε, to

array size μ, i.e.

$$\varepsilon^* = \varepsilon/\mu. \tag{1.1}$$

To build it, we shall make use of the two-scale approximation that we briefly introduce. Consider any point $x = (x_1, x_2, x_3)$ of the three-dimensional space is decomposed as

$$x = x^c + \epsilon y,$$

where x^c represents the coordinates of the center of the cell of x, $\epsilon = \begin{pmatrix} \varepsilon^* & 0 & 0 \\ 0 & \varepsilon^* & 0 \\ 0 & 0 & 1 \end{pmatrix}$, and $y = \epsilon^{-1}(x - x^c)$ is the dilated relative location of x with respect to x^c. In current cell, the points are identified by determining the cell in which the points (x_1, x_2) lie (see Figure 1.3 (a)). Then, points with coordinates y vary in the unique so-called *reference cell*, that is obtained through a translation and the dilatation ϵ^{-1} of any current cell, (see Figure 1.3 (b)) for a two-dimensional view of the reference cell.

Now, considering a distributed field $u(x)$, we introduce its *two-scale transform*

$$\widehat{u}^\epsilon(\widetilde{x}, y) = u(x^c + \epsilon y),$$

defined for any $\widetilde{x} = (x_1, x_2)$ belonging to the two-dimensional filled section of the cell, centered at $x^c = (x_1^c, x_2^c, x_3^c)$, and for any $y = (y_1, y_2, y_3)$ varying over the reference cell. We emphasize that through this construction $\widetilde{x}$ varies in a filled rectangle covering the full array, which we refer to as ω. By construction, the two-scale transform is constant, with respect to its first variable $\widetilde{x}$, over each cell. Since it depends on the ratio ε^*, it may be approximated by the asymptotic field, denoted by u^A, obtained when ε^* approaches (mathematically) 0:

$$\widehat{u}^\epsilon = u^A + O(\varepsilon^*).$$

The approximation u^A is called the *two-scale approximation* of u. We mention that as a consequence of the asymptotic process, the partial function $\widetilde{x} \mapsto u^A(\widetilde{x}, .)$ is continuous unlike the map $\widetilde{x} \mapsto \widehat{u}^\epsilon(\widetilde{x}, .)$.

Now, we observe that $u^A(\widetilde{x}, y)$ is a two-scale field, and therefore cannot be directly used as an approximation of the field $u(x)$ in the real array of cantilevers. So, an inverse two-scale transform must be applied to u^A. However, since $\widetilde{x} \mapsto u^A(\widetilde{x}, y)$ is continuous, u^A does not belong to the range of the two-scale transform. Hence we introduce an approximated inverse for the two-scale transform,

$$v(\widetilde{x}, y) \mapsto \overline{v}(x),$$

in the sense

$$\overline{\widehat{u}} = u + O(\varepsilon^*) \text{ and } \widehat{\overline{v}} = v + O(\varepsilon^*),$$

for sufficiently regular functions $u(x)$ and $v(\widetilde{x}, y)$. We are led to make two different choices for $x \mapsto \overline{v}(x)$, when x belongs to a cell centered at x^c. The first one applies to x belonging to a cantilever,

$$\overline{v}(x) = \left\langle v(., \epsilon^{-1}(x - x^c)) \right\rangle_{\widetilde{x}},$$

it is a mean in $\widetilde{x}$ over the cell. The other is for x in the base,

$$\overline{v}(x) = v(., \epsilon^{-1}(x - x^c)).$$

Once an approximate inverse two-scale transform is defined, we retain $\overline{u}^A$ as our approximation of u in the physical system. In the dissertation, we apply this technique to the mechanical displacements in the array, and we derive the equations governing the resulting two-scale field u^A.

Notations The reference cell is divided into the mechanical device Y_S and the object Y_O. Furthermore, the device Y_S is divided into the base Y_B, the cantilever flexible part Y_C, and the cantilever rigid part Y_R, (see Figure 1.4). The filled reference cell Y is a rectangle parallelepiped in $\mathbb{R}^3$.

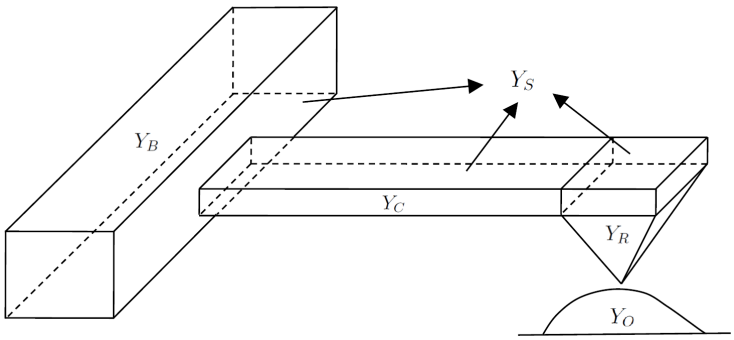

Figure 1.4: Reference cell of AFM array

We will use the *tilde* notation on variables x or y to refer to their two first components, $\widetilde{x} = (x_1, x_2)$ and $\widetilde{y} = (y_1, y_2)$ where $x = (x_1, x_2, x_3)$ and $y = (y_1, y_2, y_3)$. Accordingly, we will use the in-plane gradient $\nabla_{\widetilde{y}} = (\partial_{y_1}, \partial_{y_2})$, the in-plane Laplace operator $\Delta_{\widetilde{y}} = \partial^2_{y_1 y_1} + \partial^2_{y_2 y_2}$, the in-plane unit outward external normal components $n_{\widetilde{x}} = (n_{x_1}, n_{x_2})$ and $n_{\widetilde{y}} = (n_{y_1}, n_{y_2})$ to the boundary of ω and of the reference cell. The in-plane section of the reference cell Y is refereed as $\widetilde{Y}$ when the sections of its subdomains are denoted by $\widetilde{Y}_S$, $\widetilde{Y}_B$ and $\widetilde{Y}_C$ for instance. Similar notations are

used for their interfaces and for boundaries. The inverse of the cell section surface is constantly used, so it is referred to as

$$\widetilde{\kappa} = \frac{1}{|\widetilde{Y}|}. \tag{1.2}$$

The jump of a field v at an interface γ is written as $[\![v]\!]_\gamma$. Finally, we use the operation " : " for the inner product between two matrices A and B of same dimensions, $A : B = \sum_{i,j} A_{ij} B_{ij}$.

1.1.1 The Simple Two-Scale Model

Our models are formulated from the Kirchhoff-Love thin plate model of the whole structure, and we will always assume that the ratio of cantilever thickness h_C to base thickness h_B is small, namely

$$\frac{h_C}{h_B} \approx \varepsilon^{*4/3}. \tag{1.3}$$

Applying the two-scale approximation technique to the third component of the vector of mechanical displacement fields yields $u_3^A(t, \widetilde{x}, y)$ where t represents the time variable and is treated as a parameter. In the following, we detail the equations governing u_3^A, all parameters of its model being stated in section 1.1.2.

From the analysis, it appears that u_3^A is independent of y_3 everywhere. In the *Simple Model*, we consider cantilevers made of an isotropic material and there variations of $y_1 \mapsto u_3^A(t, \widetilde{x}, y)$ are neglected. So their motions are governed by a classical Euler-Bernoulli beam equation in the microscopic space variable y_2,

$$m^{C0} \partial_{tt}^2 u_3^A + r^{C0} \partial_{y_2 \dots y_2}^4 u_3^A = F^{C0}, \tag{1.4}$$

with m^{C0} their linear mass density, r^{C0} their linear stiffness coefficient, and F^{C0} their load per unit length, see (1.17), (1.13), (1.21).] This model holds for all $\widetilde{x} = (x_1, x_2)$, and therefore represents motions of an infinite number of cantilevers parameterized by $\widetilde{x}$ and y capture the relative motion with respect to this.

For y varying along the base, $y \mapsto u_3^A(t, \widetilde{x}, y)$ is constant and there the displacement $u_3^A(t, \widetilde{x})$ is governed by a Kirchhoff-Love plate equation

$$\rho^B \partial_{tt}^2 u_3^A + div_{\widetilde{x}}(div_{\widetilde{x}}(R^B : \nabla_{\widetilde{x}} \nabla_{\widetilde{x}}^T u_3^A)) + \ell_C^0 r^C (\partial_{y_2 y_2 y_2}^3 u_3^A)_{|junction} = f^B, \tag{1.5}$$

where ρ^B, R^B, R^B and ℓ_C^0 are respectively its effective surface mass, its homogenized stiffness tensor, its effective load per unit surface, and the cantilever width in the reference cell, see (1.15), (1.14), (1.18). The term $r^C (\partial_{y_2 y_2 y_2}^3 u_3^A)_{|junction}$ is a distributed load originating from shear forces exerted by cantilevers on the base at base-cantilever junctions.

At base-cantilever junctions, a cantilever is clamped in the base, so

$$u^A_{3|cantilever} = u^A_{3|base} \text{ and } ((\partial_{y_1}, \partial_{y_2})u^A_3.(n_1, n_2)^T)_{|cantilever} = 0, \tag{1.6}$$

because $\nabla_y u^A_3 = 0$ in the base. Other cantilever ends may be free with equations,

$$\partial^2_{y_2y_2} u^A_3 = 0 \text{ and } \partial^3_{y_2y_2y_2} u^A_3 = 0, \tag{1.7}$$

or may be equipped with a rigid part (usually a tip in Atomic Force Microscopes), then

$$J^R \partial_{tt} \begin{pmatrix} u^A_3 \\ \partial_{y_2} u^A_3 \end{pmatrix} + r^{C0} \begin{pmatrix} -\partial^3_{y_2y_2y_2} u^A_3 \\ \partial^2_{y_2y_2} u^A_3 \end{pmatrix} = F^{R0} \tag{1.8}$$

at a junction between an elastic part and a rigid part. Here, J^R is a matrix of moments and F^{R0} is comprised of effective forces and moments stated in (1.32). Last, the external base boundary being clamped in a fixed support

$$u^A_3 = 0 \text{ and } \nabla_{\widetilde{x}} u^A_3 . n_{\widetilde{x}} = 0 \tag{1.9}$$

on its boundary.

1.1.2 The General Two-Scale Model

In section 1.1.1, the model was introduced assuming that the base and cantilevers are rectangle parallelepiped, and that their deformations in the y_1 direction are negligible. Now, we relax these assumptions, and we present in detail a more general two-scale model that may also take into account possible interactions between tips and rigid objects. We restrict the presentation to the situation where the bodies are in contact with friction. This is applicable to contact mode microscopy with atomic force microscopes. In addition to approximation of displacements, we provide approximations of elastic strains and stresses. The approximations are still posed in the Kirchhoff-Love thin plate model where we still neglect mean (in the thickness direction) in-plane displacements.

Model Parameters The model parameters result from two-scale approximations of the physical data, namely coefficients, loads and initial conditions.

Remark 1 *It is natural to consider that the problem geometry and equation coefficients are parameterized by ε^*, but it is artificial to say the same thing regarding other data as loads or initial conditions. However, to follow the common use we proceed as if they were also known sequences of ε^*, with a known two-scale approximation. For some of them, we do not require their direct two-scale approximation but this of their product by a power of ε^*. This provide a measure of the asymptotic behavior required so that the model be well justified. Remark that for actual model computations, we do not use the two-scale approximation of parameters but only their two-scale transform.*

Let R^P be the thin plate stiffness per unit area, for instance for a plate with thickness h made of an isotropic material

$$R^P_{\alpha\beta\gamma\rho} = \frac{Eh^3}{12(1+\nu)}\left(\frac{\nu}{1-\nu}\delta_{\alpha\beta}\delta_{\gamma\rho} + \delta_{\alpha\gamma}\delta_{\beta\rho}\right), \tag{1.10}$$

the assumption (1.3) on ratio thicknesses may be restated with respect to stiffness as

$$\frac{R^P_{|\Omega_C}}{R^P_{|\Omega_B}} \sim \varepsilon^{*4}. \tag{1.11}$$

Posing the order of magnitude of base stiffness in the range of 1 with respect to ε^*, the two-scale stiffness tensors r^B (respectively r^C) per unit area in ω and per unit area in the base $\widetilde{Y}_B$ (respect. in cantilever $\widetilde{Y}_C$) is defined as the two-scale approximation of $\widetilde{\kappa}R^P$ (respect. of $\varepsilon^{*-4}\widetilde{\kappa}R^P$), that we write simply as,

$$r^B \approx \widetilde{\kappa}\widehat{R}^P \text{ in } \omega \times \widetilde{Y}_B \text{ (respect. } r^C \approx \varepsilon^{*-4}\widetilde{\kappa}\widehat{R}^P). \tag{1.12}$$

The stiffness per unit area in ω and per unit length in cantilever of the *Simple Model* is therefore $r^{C0} = \ell^0_C(1-\nu^2)r^C$, where we recall that ℓ^0_C is the scaled cantilever width ℓ_C/ε^* in the reference cell. In case of an isotropic material,

$$r^{C0} \approx \varepsilon^{*-4}\widetilde{\kappa}\ell^0_C E^C I^C = \varepsilon^{*-4}\widetilde{\kappa}\frac{E_C h_C^3 \ell^0_C}{12}, \tag{1.13}$$

E^C being the cantilever elastic modulus and $I^C = h_C^3/12$ the second moment of cantilever section. We introduce the effective stiffness tensor R^B per unit area in the base,

$$R^B_{\alpha\beta\gamma\rho} = \int_{\widetilde{Y}_B} r^B_{\alpha\beta\gamma\rho} + r^B_{\alpha\beta\xi\zeta}\mathcal{L}^B_{\xi\zeta\gamma\rho}\, d\widetilde{y}, \tag{1.14}$$

where the tensor $\mathcal{L}^B$ is defined in (A.6) below. Then, ρ representing the volume mass density, the effective mass density ρ^B per unit area in the base is

$$\rho^B \approx \widetilde{\kappa}\int_{Y_B} \widehat{\rho}\, dy \text{ in } \omega. \tag{1.15}$$

The other mass densities appearing in the model are two-scale densities: in cantilever m^C is per unit area times area when in the rigid tips and in objects ρ^R and ρ^O are per unit area times volume. Indeed,

$$m^C \approx \widetilde{\kappa}\int_{-h_C/2}^{h_C/2} \widehat{\rho}\, dy_3 \text{ in } \omega\times\widetilde{Y}_C,\ \rho^R \approx \widetilde{\kappa}\widehat{\rho} \text{ in } \omega\times Y_R \text{ and } \rho^O \approx \widetilde{\kappa}\widehat{\rho} \text{ in } \omega\times Y_O. \tag{1.16}$$

The two-scale mass density m^{C0} per unit area in ω and per unit length in cantilevers follows,

$$m^{C0} = \ell_C^0 m^C. \tag{1.17}$$

The base effective load f^B per unit area, the base effective moments g_α^B about the plate section per unit area are derived from the two-scale approximations of the vector of loads $f = (f_1, f_2, f_3)$ per unit volume,

$$f^B \approx \widetilde{\kappa} \int_{Y_B} \widehat{f}_3 \, dy, \text{ and } g_\alpha^B \approx \widetilde{\kappa} \int_{Y_B} y_3 \widehat{f}_\alpha \, dy \text{ in } \omega. \tag{1.18}$$

The cantilever two-scale load F^C and the moment G^C per unit area times area in $\omega \times \widetilde{Y}_C$, the tip two-scale load F^R and the moment G^R per unit area times volume, and the object two-scale load F^O per unit area times volume are defined similarly from f

$$F^C \approx \widetilde{\kappa} \int_{-h_C/2}^{h_C/2} \widehat{f}_3 \, dy_3 \text{ and } G_\alpha^C \approx \frac{\widetilde{\kappa}}{\varepsilon^*} \int_{-h_C/2}^{h_C/2} y_3 \widehat{f}_\alpha \, dy_3 \text{ in } \omega \times \widetilde{Y}_C, \tag{1.19}$$

$$F^R \approx \widetilde{\kappa} \widehat{f}_3, \; G_\alpha^R \approx \frac{\widetilde{\kappa}}{\varepsilon^*} y_3 \widehat{f}_\alpha \text{ in } \omega \times Y_R \text{ and } F^O \approx \varepsilon^* \widetilde{\kappa} \widehat{f} \text{ in } \omega \times Y_O. \tag{1.20}$$

The cantilever two-scale load of the *Simple Model* follows

$$F^{C0} = \ell_C^0 F^C. \tag{1.21}$$

The two-scale load and moment corresponding to a periodic distribution of concentrated load $(\sum_c f_{ci} \delta_{z^c}(x))_{i=1..3}$ applied at points $z^c = x^c + \epsilon y^0$ is

$$\begin{aligned} F^D &= \frac{1}{(\varepsilon^*)^d} \sum_c \chi_{\widetilde{Y}^\varepsilon(x^c)}(z) f_c \delta_{y^0}(y) \approx |\widetilde{Y}| \sum_c \delta_{\widetilde{x}^c}(z) f_c \delta_{y^0}(y) \qquad (1.22) \\ \text{and } G^D &= \frac{1}{(\varepsilon^*)^{d+1}} \sum_c \chi_{\widetilde{Y}^\varepsilon(x^c)}(z) f_c y_3^0 \delta_{y^0}(y) \approx \frac{|\widetilde{Y}|}{\varepsilon^*} \sum_c \delta_{\widetilde{x}^c}(z) f_c y_3^0 \delta_{y^0}(y). \end{aligned}$$

The two-scale friction coefficient at the two-scale tip-object interface $\omega \times \gamma_{R,O}$ is an approximation built from the tip-object friction coefficient ζ,

$$z^{Fr} \approx \widetilde{\kappa} \frac{\widehat{\zeta}}{\varepsilon^{*2}}. \tag{1.23}$$

For given initial transverse displacement u_3^0 and velocity u_3^1 in the whole system together with lateral displacements u_α^0 and velocity u_α^1 in objects, the two-scale initial displacements and velocities are defined by the approximations

$$\begin{gathered} u_3^{A0} \approx \widehat{u}_3^0, \; u_3^{A1} \approx \widehat{u}_3^1 \text{ in } \omega \times (Y_S \cup Y_O), \\ \text{and } u_\alpha^{A0} \approx \varepsilon^* \widehat{u}_\alpha^0, \; u_\alpha^{A1} \approx \varepsilon^* \widehat{u}_\alpha^1 \text{ in } \omega \times Y_O. \end{gathered}$$

Moreover, u^{A0} and u^{A1} are assumed to fulfil the forthcoming kinematics (1.24-1.28).

Admissible kinematics The two-scale fields u^A satisfies a kinematics inherited from the Kirchhoff-Love kinematics and from the two-scale approximation of derivatives. In the whole mechanical structure comprised of a base and of cantilevers,

$$u_3^A \text{ and } u^B \text{ are independent of } y_3. \tag{1.24}$$

We neglect mean in-plane displacements, and we assume that the surface $y_3 = 0$ corresponds to the mean section of the cantilevers and of the base. So,

$$u_\alpha^A = -y_3 \partial_{x_\alpha} u_3^A \text{ in } \omega \times Y_B \text{ and } u_\alpha^A = -y_3 \partial_{y_\alpha} u_3^A \text{ in } \omega \times (Y_C \cup Y_R). \tag{1.25}$$

In the base, u_3^A is independent of (y_1, y_2), that is

$$\nabla_{\widetilde{y}} u_3^A = 0. \tag{1.26}$$

The conditions of rigidity for tips and for objects are formulated as

$$\nabla_{\widetilde{y}} \nabla_{\widetilde{y}}^T u_3^A = 0 \text{ in tips and } s_y(u^A) = 0 \text{ in objects}, \tag{1.27}$$

where $s_y(u) = \frac{1}{2}(\nabla_y u + (\nabla_y u)^T)$ is the usual strain tensor in the y variables. The contact condition between tips and rigid objects results in normal displacement continuity through their interface $\gamma_{R,O}$,

$$[\![u^A]\!]_{\gamma_{R,O}}.n_y = 0, \tag{1.28}$$

where n_y denotes the unit outward normal vector to boundaries in the reference cell.

Equations of motion In cantilevers, the transverse displacement u_3^A is governed by a Love-Kirchhoff thin plate equation in the y variables,

$$m^C \partial_{tt}^2 u_3^A + div_{\widetilde{y}}(div_{\widetilde{y}}(M^C(u_3^A))) = F^C \text{ in } \omega \times \widetilde{Y}_C, \tag{1.29}$$

and the shear force matrix in cantilevers is $M^C(u_3^A) = r^C : \nabla_{\widetilde{y}} \nabla_{\widetilde{y}}^T u_3^A$. In the base, the transverse displacement u_3^A is also governed by a thin plate Love-Kirchhoff model in the macroscopic variables, with a contribution of the bending moment exerted by the cantilever distribution. This coupling with cantilevers appears under the form of an integral along the interface line $\widetilde{\gamma}_{B,C}$ between $\widetilde{Y}_B$ and $\widetilde{Y}_C$,

$$\rho^B \partial_{tt}^2 u_3^A + \partial_{x_\alpha x_\beta}^2 M_{\alpha\beta}^B(u_3^A) - \int_{\widetilde{\gamma}_{B,C}} div_{\widetilde{y}}(M^C(u_3^A)).n_{\widetilde{y}} \, d\widetilde{s} = f^B \text{ in } \omega \times \widetilde{Y}_B, \tag{1.30}$$

where the shear forces in the base are given by

$$M^B_{\alpha\beta}(u^A_3) = R^B_{\alpha\beta\gamma\delta}\partial^2_{x_\gamma x_\delta} u^A_3.$$

For the sake of shortness, we write the motion equations in tips and in objects under their variational formulation. This avoids formulating in detail their dynamics together with the interface condition. The admissible displacement set is built from the above admissible conditions,

$$W^A = \{u^A \text{ defined in } Y_R \cup Y_O \text{ satisfying (1.24, 1.25, 1.27, and 1.28)}\}.$$

For a given vector field $v \in W^A$, we introduce its tangent component v_T on the interface $\gamma_{R,O}$ defined as,

$$v_T = v - (v.n_y)n_y,$$

and $\widetilde{\gamma}_{C,R}$ the interface between $\widetilde{Y}_C$ and $\widetilde{Y}_R$. The linear form of the right hand side is

$$l^R(v) = \int_{Y_R} F^R_3 v_3 - G^R.\nabla_{\widetilde{y}} v_3 \; dy + \int_{Y_O} F^O.v \; dy - \int_{\widetilde{\gamma}_{C,R}} G^C.n_{\widetilde{y}} \; v_3 \; d\widetilde{s},$$

and the bilinear forms are

$$c^R(u^A, v) = \int_{Y_R} \rho^R u^A_3 v_3 \; dy + \int_{Y_O} \rho^O u^A.v \; dy,$$

$$b^R(u^A, v) = \int_{\gamma_{R,O}} z^{Fr} [\![u^A_T]\!]_{\gamma_{R,O}}.[\![v_T]\!]_{\gamma_{R,O}} \; ds$$

$$a^R(u^A_3, v_3) = \int_{\widetilde{\gamma}_{C,R}} (M^C(u^A_3)n_{\widetilde{y}}).\nabla_{\widetilde{y}} v_3 - div_{\widetilde{y}}(M^C(u^A_3)).n_{\widetilde{y}} \; v_3 \; d\widetilde{s}.$$

The variational formulation states as $u^A(t, x, .) \in W^A$ and

$$\partial^2_{tt} c^R(u^A, v) + \partial_t b^R(u^A, v) + a^R(u^A_3, v_3) = l^R(v) \text{ for all } v \in W^A. \tag{1.31}$$

For the *Simple Model*, this equation was restated as a boundary condition (1.8) at $\widetilde{\gamma}_{C,R}$ where

$$J^R = \begin{pmatrix} J_0 & J_1 \\ J_1 & J_2 \end{pmatrix} \text{ and } F^{R0} = \begin{pmatrix} \int_{Y_R} F^R_3 \; dy - \ell^0_C G^C_{|\widetilde{\gamma}_{C,R}} \\ \int_{Y_R} F^R_3 (y_2 - y_{2|\widetilde{\gamma}_{C,R}}) \; dy - G^R_2 \end{pmatrix}, \tag{1.32}$$

with $J_k = \int_{Y_R} (y_2 - y_{2|\widetilde{\gamma}_{C,R}})^k \; dy_2$ being a k^{th} moment of the rigid part Y_R about the junction $\widetilde{\gamma}_{C,R}$ in the direction y_2.

Interface and boundary conditions Cantilevers being clamped in a base, the deflection u^A_3 and its derivatives are continuous through the base-cantilever interface $\widetilde{\gamma}_{B,C}$,

$$u^A_{3|\omega\times\widetilde{Y}_C} = u^A_{3|\omega\times\widetilde{Y}_B} \text{ and } (\nabla_{\widetilde{y}} u^A_3)_{|\omega\times\widetilde{Y}_C} = 0 \text{ at } \widetilde{\gamma}_{B,C}. \tag{1.33}$$

At free cantilever boundaries,

$$n_{\widetilde{y}}^T M^C(u_3^A) n_{\widetilde{y}} = 0,\ \nabla_{\widetilde{y}}(n_{\widetilde{y}}^T M^C(u_3^A)\tau_{\widetilde{y}}).\tau_{\widetilde{y}} + div_{\widetilde{y}}(M^C(u_3^A)).n_{\widetilde{y}} = 0 \tag{1.34}$$

where $\tau_{\widetilde{y}}$ is the tangent vector to the reference cell's boundary. Along the complete boundaries of ω where base is clamped, the two-scale transverse displacement fulfils clamping like conditions,

$$u_3^A = \nabla_{\widetilde{x}} u_3^A . n_{\widetilde{x}} = 0 \text{ at } \partial\omega \times \widetilde{Y}_B. \tag{1.35}$$

Initial conditions The two-scale transverse displacement and its velocity are initialized in the whole system $\omega \times (Y_S \cup Y_O)$ by

$$u_3^A = u_3^{A0},\ \partial_t u_3^A = u_3^{A1}.$$

In-plane displacements and their time derivatives are initialized, in objects $\omega \times Y_O$ only, by

$$u_\alpha^A = u_\alpha^{A0} \text{ and } \partial_t u_\alpha^A = u_\alpha^{A1}. \tag{1.36}$$

Eigenvalue Problem We consider the model without object, and we state the associated eigenvalue problem as well as a property of factorization of eigenvectors. An eigenvalue λ^A and an eigenvector $\psi^A(\widetilde{x}, \widetilde{y})$ satisfy the constraints

$$\nabla_{\widetilde{y}} \psi^A = 0 \text{ in } \widetilde{Y}_B,\ \nabla_{\widetilde{y}} \nabla_{\widetilde{y}}^T \psi^A = 0 \text{ in } Y_R, \tag{1.37}$$

an equation in the base

$$div_{\widetilde{x}}(div_{\widetilde{x}}(M^B(\psi^A))) - \int_{\widetilde{\gamma}_{B,C}} div_{\widetilde{y}}(M^C(\psi^A))_{|\widetilde{Y}_C} . n_{\widetilde{y}}\ ds = \rho^B \lambda^A \psi^A \text{ in } \omega \times \widetilde{Y}_B, \tag{1.38}$$

an equation in cantilevers

$$div_{\widetilde{y}}(div_{\widetilde{y}}(M^C(\psi^A))) = \lambda^A m^C \psi^A \text{ in } \widetilde{Y}_C, \tag{1.39}$$

and a variational formulation in the rigid part,

$$\psi^A_{|Y_R} \in W^A,\ a^R(\psi^A, v) = \lambda^A c^R(\psi^A, v) \text{ for all } v \in W^A, \tag{1.40}$$

endowed with the reduced definition

$$W^A = \{v \text{ defined in } Y_R \mid \partial_{y_3} v = 0 \text{ and } \nabla_{\widetilde{y}} \nabla_{\widetilde{y}}^T v = 0\}.$$

The boundary and interface conditions for ψ^A are not detailed since they are the same as for u_3^A in (1.33-1.35).

Factorization of the Eigenvectors Now, we state that each eigenvector ψ^A can be written as the product of a *macroscopic eigenvector* defined in ω only by a *microscopic (or local) eigenvector* defined in $\widetilde{Y}_C \cup Y_R$ only. We first introduce the *macroscopic eigenvalue problem* where λ^B and $\varphi^B(\widetilde{x})$ denote respectively an eigenvalue and an eigenvector,

$$\begin{gathered} div_{\widetilde{x}}(div_{\widetilde{x}}(M^B(\varphi^B))) = \lambda^B \rho^B \varphi^B \text{ in } \omega, \\ \varphi^B = \nabla_{\widetilde{x}} \varphi^B . n_{\widetilde{x}} = 0 \text{ on } \partial\omega. \end{gathered}$$

Then, for each λ^B we define the *microscopic eigenvalue problem* in cantilevers where λ^C and φ^C represent an eigenvalue and an eigenvector,

$$\begin{gathered} div_{\widetilde{y}}(div_{\widetilde{y}}(M^C(\varphi^C))) = \lambda^C m^C \varphi^C \text{ in } \widetilde{Y}_C, \\ \lambda^B \rho^B \varphi^C - div_{\widetilde{y}} M^C(\varphi^C) n_{\widetilde{y}} = \lambda^C \rho^B \varphi^C \text{ and } \nabla_{\widetilde{y}} \varphi^C = 0 \text{ at } \widetilde{\gamma}_{B,C}, \\ \text{and } n_{\widetilde{y}}^T M^C(\varphi^C) n_{\widetilde{y}} = 0, \\ \nabla_{\widetilde{y}}(n_{\widetilde{y}}^T M^C(\varphi^C) \tau_{\widetilde{y}}) . \tau_{\widetilde{y}} + div_{\widetilde{y}}(M^C(\varphi^C)) . n_{\widetilde{y}} = 0 \text{ at free boundaries}, \end{gathered}$$

together with the variational formulation in rigid parts,

$$\varphi^C_{|Y_R} \in W^A, \ a^R(\varphi^C, v) = \lambda^C c^R(\varphi^C, v) \text{ for all } v \in W^A.$$

Finally, we state the decomposition property. For the sake of brevity its proof is omitted.

Proposition 2 *For each pair (λ^A, ψ^A) solution to (1.37-1.40), there exists a unique pair (λ^B, φ^B) and a unique pair (λ^C, φ^C) such that $\psi^A(\widetilde{x}, \widetilde{y}) = \varphi^B(\widetilde{x})\varphi^C(\widetilde{y})$ and $\lambda^A = \lambda^C$. Reciprocally, for any pair (λ^B, φ^B) and any pair (λ^C, φ^C), its combination $(\varphi^B(\widetilde{x})\varphi^C(\widetilde{y}), \lambda^C)$ determines the pair $(\psi^A(\widetilde{x}, \widetilde{y}), \lambda^A)$ which is solution to (1.37-1.40).*

1.2 Model Implementation

In this section, we provide further details in view of the model implementation for a two-dimensional array and then for a one-dimensional array without object.

First, we summarize the coefficient expressions in case of constant coefficients

$$\ell_C^0 = \frac{\ell_C}{\varepsilon^*},\ L_C^0 = \frac{L_C}{\varepsilon^*},\ \widetilde{\kappa} = \frac{1}{|\widetilde{Y}|},\ R^P_{\alpha\beta\gamma\rho} = \frac{Eh^3}{12(1+\nu)}(\frac{\nu}{1-\nu}\delta_{\alpha\beta}\delta_{\gamma\delta} + \delta_{\alpha\gamma}\delta_{\beta\rho}),$$

$$r^B \approx \widetilde{\kappa} R^P \text{ in } \omega \times \widetilde{Y}_B,\ \overline{r^C} = (1-\nu^2) r^C_{1111} = \varepsilon^{*-4}\frac{\widetilde{\kappa} E h^3}{12},$$

$$R^B_{\alpha\beta\gamma\rho} = \int_{\widetilde{Y}_B} r^B_{\alpha\beta\gamma\rho} + r^B_{\alpha\beta\xi\zeta}\mathcal{L}^B_{\xi\zeta\gamma\rho}\ d\widetilde{y},$$

$$\rho^B \approx \widetilde{\kappa}|Y_B|\rho_{|Y_B},\ m^C \approx \widetilde{\kappa} h_C \rho_{|Y_C},\ \rho^R \approx \widetilde{\kappa}\rho_{|Y_R},$$

$$Q = N \begin{pmatrix} J_0 & J_1 \\ J_1 & J_2 \end{pmatrix} N, \text{ with } N = \begin{pmatrix} 1 & 0 \\ 0 & 1/L_C^0 \end{pmatrix} \text{ and } J_k = \int_{Y_R} (y_2 - L_C^0)^k\ dy,$$

$$f^B \approx \widetilde{\kappa}\int_{Y_B} \widehat{f}_3\ dy, \text{ and } g^B_\alpha \approx \widetilde{\kappa}\int_{Y_B} y_3 \widehat{f}_\alpha\ dy \text{ in } \omega,\ F^C \approx \widetilde{\kappa}\int_{-h_C/2}^{h_C/2} \widehat{f}_3\ dy_3$$

$$\text{and } G^C_2 \approx \frac{\widetilde{\kappa}}{\varepsilon^*}\int_{-h_C/2}^{h_C/2} y_3 \widehat{f}_2\ dy_3 \text{ in } \omega \times \widetilde{Y}_C,\ F^R \approx \widetilde{\kappa}\widehat{f}_3,\ G^R_\alpha \approx \frac{\widetilde{\kappa}}{\varepsilon^*} y_3 \widehat{f}_\alpha \text{ in } \omega \times Y_R.$$

1.2.1 The Two-dimensional Case

We detail the formulation of the model when variations of displacements in cantilever width are ignored. We recall that u_3^A is solution of the problem: Find $u_3^A \in V_3^A$ such that

$$\partial^2_{tt} c^A(u_3^A, v_3^A) + \widetilde{a}^A(u_3^A, v_3^A) = l^A(v_3^A) \text{ for all } v_3^A \in V_3^A \tag{1.41}$$

accompanied with initial conditions

$$u_3^A = u_3^{A0} \text{ and } \partial_t u_3^A = u_3^{A1} \text{ at } t = 0,$$

where

$$\begin{array}{c} \widetilde{a}^A(u_3^A, v_3^A) = \int_\omega [\big(\big[R^B : \nabla_{\widetilde{x}}\nabla^T_{\widetilde{x}} u_3^A\big] : \nabla_{\widetilde{x}}\nabla^T_{\widetilde{x}} v_3^A\big)_{|\widetilde{Y}_B} \\ + \ell_C^0 \int_0^{L_C^0} \overline{r^C}\partial^2_{y_2y_2} u_3^A \partial^2_{y_2y_2} v_3^A\ dy_2^C] d\widetilde{x}, \end{array} \tag{1.42}$$

$$\begin{array}{c} c^A(u_3^A, v_3^A) = \int_\omega [(\rho^B u_3^A v_3^A)_{|\widetilde{Y}_B} + \ell_C^0 \int_0^{L_C^0} m^C u_3^A v_3^A\ dy_2^C \\ + \int_{Y_R} \rho^R u_3^A v_3^A\ dy] d\widetilde{x}, \end{array} \tag{1.43}$$

and

$$\begin{array}{c} l^A(v_3^A) = \int_\omega [(f^B v_3^A - g^B.\nabla_{\widetilde{x}} v_3^A)_{|\widetilde{Y}_B} + \int_{\widetilde{Y}_C} F^C\ v_3^A - G_2^C \partial_{y_2} v_3^A\ d\widetilde{y} \\ + \int_{Y_R} F^R v_3^A - G_2^R \partial_{y_2} v_3^A\ dy] d\widetilde{x} + (F^D - G^D) v_3^A. \end{array} \tag{1.44}$$

The eigenmodes $\psi^A \in V_3^A$ are solution of

$$\widetilde{a}^A(\psi^A; v_3^A) = \lambda^A c^A(\psi^A, v_3^A) \text{ for all } v_3^A \in V_3^A \tag{1.45}$$

with the normalization condition $c^A(\psi^A, \psi^A) = 1$.

For a rectangle domain $\omega = (0, L_1) \times (0, L_2)$, we introduce the factorization of $\psi^A(\widetilde{x}, y_2) = \varphi^B(\frac{x_1}{L_1}, \frac{x_2}{L_2})\varphi^C(\frac{y_2^C}{L_C^0})$ where φ^B and φ^C are solution to the two following eigenvalue problems where y_2^C is the translation of y_2 equal to zero at the clamping point of the cantilever to the base. First, $\varphi^B \in H_0^2((0,1)^2)$ with λ^B are solution to the weak formulation

$$\begin{array}{c} a^B(\varphi^B, v^B) = \lambda^B c^B(\varphi^B, v^B) \text{ for all } v^B \in H_0^2((0,1)^2) \\ \text{normalized by the condition } c^B(\varphi^B, \varphi^B) = 1, \end{array} \tag{1.46}$$

where the bilinear forms are defined on the scaled domain $(0,1)^2$ by

$$\begin{array}{c} a^B(\varphi^B, v^B) = \int_{(0,1)^2} \left[R^{B0} : \nabla_\xi \nabla_\xi^T \varphi^B\right] : \nabla_\xi \nabla_\xi^T v^B \; d\xi \\ \text{and } c^B(\varphi^B, v^B) = \int_{(0,1)^2} \varphi^B \; v^B \; d\xi, \end{array} \tag{1.47}$$

and R^{B0} is the scaled homogenized stiffness tensor

$$\begin{array}{c} R^{B0}_{\alpha\beta\gamma\delta} = \frac{R^B_{\alpha\beta\gamma\delta}}{R^B_{\max} L^0_\alpha L^0_\beta L^0_\gamma L^0_\delta} \text{ with } L^0_\alpha = \frac{L_\alpha}{\mu}, \\ \mu = \frac{L_1 + L_2}{2} \text{ and } R^B_{\max} = \max_{\alpha,\beta,\gamma,\delta}(R^B_{\alpha\beta\gamma\delta}). \end{array} \tag{1.48}$$

Next, $\varphi^C \in V^C = \{v \in H^4(0,1) \mid \partial_\xi v(0) = 0\}$ with λ^C are solution to the weak formulation

$$\begin{array}{c} a^C(\varphi^C, v^C) = \lambda^C c^C(\varphi^C, v^C) \text{ for all } v^C \in V^C \\ \text{normalized by } c^C(\varphi^C, \varphi^C) = \frac{\overline{r^C}}{(L_C^0)^4 m^C}, \end{array} \tag{1.49}$$

where

$$a^C(\varphi^C, v^C) = \frac{|\omega| R^B_{\max}}{\mu^4} \lambda^B \left(\varphi^C \; v^C\right)_{|\xi=0} + \frac{|\omega| \ell_C^0}{(L_C^0)^3} \int_0^1 \overline{r^C} \partial^2_{\xi\xi} \varphi^C \partial^2_{\xi\xi} v^C \; d\xi, \tag{1.50}$$

and

$$\begin{array}{c} c^C(\varphi^C, v^C) = \frac{|\omega| \overline{r^C}}{(L_C^0)^4 m^C} [(\rho^B \varphi^C v^C)_{|\xi=0} + \ell_C^0 L_C^0 \int_0^1 m^C \varphi^C v^C \; d\xi \\ + \rho^R \int_{Y_R} \varphi^C v^C \; dy]. \end{array} \tag{1.51}$$

So, the normalization condition reads as

$$|\omega|[\rho^B(\varphi^C_{|\xi=0})^2 + \ell_C^0 L_C^0 \int_0^1 m^C (\varphi^C)^2 \; d\xi + \rho^R (\varphi^C, \partial_\xi \varphi^C)_{|\xi=1} Q \begin{pmatrix} \varphi^C \\ \partial_\xi \varphi^C \end{pmatrix}_{|\xi=1}] = 1.$$

The boundary value problem satisfied by φ^C states therefore as

$$\partial^4_{\xi\xi\xi\xi} \varphi^C = \lambda^C \varphi^C \text{ in } (0,1) \tag{1.52}$$

with the boundary conditions

$$\partial_\xi \varphi^C = 0 \text{ and } \frac{R^B_{\max}(L^0_C)^4 m^C}{\overline{r^C}\mu^4\rho^B}\lambda^B\varphi^C + \frac{m^C\ell^0_C L^0_C}{\rho^B}\partial^3_{\xi\xi\xi}\varphi^C = \lambda^C\varphi^C \text{ at } \xi = 0, \quad (1.53)$$

and

$$\begin{pmatrix} -\partial^3_{\xi\xi\xi}\varphi^C \\ \partial^2_{\xi\xi}\varphi^C \end{pmatrix} = \frac{\lambda^C\rho^R}{\ell^0_C L^0_C m^C} Q \begin{pmatrix} \varphi^C \\ \partial_\xi\varphi^C \end{pmatrix} \text{ at } \xi = 1. \quad (1.54)$$

Then

$$\lambda^A = \lambda^C \frac{\overline{r^C}}{(L^0_C)^4 m^C}.$$

Finally, the weak formulation of the cell problem is: Find $w^B \in V^B$ such that,

$$\int_{\widetilde{Y}_B} M^{B0} : \nabla_{\widetilde{y}}\nabla^T_{\widetilde{y}} v^B \, d\widetilde{y} = -\int_{\widetilde{Y}_B} F^B : \nabla_{\widetilde{y}}\nabla^T_{\widetilde{y}} v^B \, d\widetilde{y} \text{ for all } v^B \in V^B, \quad (1.55)$$

where $M^{B0} = r^B : \nabla_{\widetilde{y}}\nabla^T_{\widetilde{y}} w^B$, $F^B = r^B : \zeta$, ζ being a symmetric 2×2 matrix.

The evolution problem (1.41) is solved using the modal decomposition

$$u^A_3(t, \widetilde{x}, y_2) = \sum_k U_k(t)\psi^A_k(\widetilde{x}, y_2),$$

where the modal coefficients U_k are solution to the ordinary differential equation

$$\partial^2_{tt} U_k + \lambda^A_k U_k = l^A(\psi^A_k). \quad (1.56)$$

In view of insuring fast computations, we further assume (it is a strong assumption that may be relaxed) that the loads are products of functions of microscale, macroscale or time variable. Precisely, we consider loads f_i as

$$\begin{aligned}
\widehat{f_3}(t, \widetilde{x}, y) &= f^0_3(\widetilde{x}, y) f^{B2}(t), \\
\widehat{f_\alpha}(t, \widetilde{x}, y) &= f^0_\alpha(\widetilde{x}, y) g^{B2}_\alpha(t) \text{ in } Y_B, \\
\widehat{f_3}(t, \widetilde{x}, y_2, y_3) &= F^{C0}(\widetilde{x}) f^{C1}_3(y_2, y_3) F^{C2}(t), \\
\widehat{f_2}(t, \widetilde{x}, y_2, y_3) &= G^{C0}(\widetilde{x}) f^{C1}_2(y_2, y_3) G^{C2}(t) \text{ in } Y_C, \\
\widehat{f_3}(t, \widetilde{x}, y) &= F^{R0}(\widetilde{x}) f^{R1}_3(y) F^{R2}(t), \\
\widehat{f_2}(t, \widetilde{x}, y) &= G^{R0}(\widetilde{x}) f^{R1}_2(y) G^{R2}(t) \text{ in } Y_R,
\end{aligned} \quad (1.57)$$

plus a concentrated load at the tips with microscale coordinate y^{tip},

$$\widehat{f^{tip}_i}(t, \widetilde{x}, y) = \sum_c f^{tip}_{i,c}(t)\delta_{\widetilde{x}^c}(\widetilde{x})\delta_{y^{tip}}(y). \quad (1.58)$$

Posing

$$f^{B0}(\widetilde{x}) \approx \frac{1}{|Y_B|}\int_{Y_B} \widehat{f_3}\ dy,\ f^{B1} = \widetilde{\kappa}|Y_B|,\ g_\alpha^{B0}(\widetilde{x}) \approx \frac{1}{|Y_B|}\int_{Y_B} y_3\widehat{f_\alpha}\ dy,\ g_\alpha^{B1} = \widetilde{\kappa}|Y_B|,$$
$$F^{C1}(y_2) = \widetilde{\kappa}\int_{-h_C/2}^{h_C/2} f_3^{C1}\ dy_3,\ G^{C1}(y_2) = \frac{\widetilde{\kappa}}{\varepsilon^*}\int_{-h_C/2}^{h_C/2} y_3 f_2^{C1}\ dy_3,$$
$$F^{R1} = \widetilde{\kappa} f_3^{R1},\ G^{R1} = \frac{\widetilde{\kappa}}{\varepsilon^*} y_3 f_2^{R1},\ F_c^D = |\widetilde{Y}| f_{3c}^{tip},\ G_c^D = \frac{|\widetilde{Y}|}{\varepsilon^*} y_3 f_{2c}^{tip},$$

we derive the two-scale loads,

$$f^B(t,\widetilde{x}) = f^{B0}(\widetilde{x})f^{B1}f^{B2}(t),\ g_\alpha^B(t,\widetilde{x}) = g_\alpha^{B0}(\widetilde{x})g_\alpha^{B1}g_\alpha^{B2}(t) \text{ in } Y_B,$$
$$F^C(t,\widetilde{x},y_2) = F^{C0}(\widetilde{x})F^{C1}(y_2)F^{C2}(t),\ G_2^C(t,\widetilde{x},y_2) = G^{C0}(\widetilde{x})G^{C1}(y_2)G^{C2}(t) \text{ in } Y_C,$$
$$F^R(t,\widetilde{x},y) = F^{R0}(\widetilde{x})F^{R1}(y)F^{R2}(t),\ G_2^R(t,\widetilde{x},y) = G^{R0}(\widetilde{x})G^{R1}(y)G^{R2}(t) \text{ in } Y_R,$$
$$F^D(t,\widetilde{x},y) = \sum_c F_c^D(t)\delta_{\widetilde{x}^c}(\widetilde{x})\delta_{y^{tip}}(y),\ G^D(t,\widetilde{x},y) = \sum_c G_c^D(t)\delta_{\widetilde{x}^c}(\widetilde{x})\delta_{y^{tip}}(y).$$

Inserting these expression in the right hand side of the modal equation (1.56), we can rewrite it as

$$\begin{array}{c} l^A(\psi^A) = \int_\omega f^{B0}\varphi^B\ d\widetilde{x}\ \varphi^C(0)f^{B1}f^{B2}(t) \\ -\sum_\alpha \int_\omega g_\alpha^{B0}\frac{\partial_{\xi_\alpha}\varphi^B}{L_\alpha}\ d\widetilde{x}\ \varphi^C(0)g_\alpha^{B1}g_\alpha^{B2}(t) \\ +\int_\omega F^{C0}\varphi^B\ d\widetilde{x}\int_0^{L_C^0} F^{C1}\varphi^C\ dy_2^C F^{C2} \\ -\int_\omega G^{C0}\varphi^B\ d\widetilde{x}\int_0^{L_C^0} G^{C1}\frac{\partial_\xi\varphi^C}{L_C^0}\ dy_2^C G^{C2} \\ +\int_\omega F^{R0}\varphi^B\ d\widetilde{x}\int_{Y_R} F^{R1}\varphi^C\ dyF^{R2} \\ -\int_\omega G^{R0}\varphi^B\ d\widetilde{x}\int_{Y_R} G^{R1}\frac{\partial_\xi\varphi^C}{L_C^0}\ dy_2^C G^{R2} \\ +\sum_c F_c^D\psi^A(x^c,y^{tip}) - G_c^D\partial_{y_2}\psi^A(x^c,y^{tip}). \end{array} \tag{1.59}$$

1.2.2 The One-dimensional Case

The one-dimensional model can be formulated in a manner which is very close to the two-dimensional model. Here, we present its formulation and we mainly quote the differences with the two-dimensional one. The rectangle ω is replaced by a single row $\omega = (0,L_1)\times(0,\varepsilon^*\ell_2)$, so $|\omega| = \varepsilon^*\ell_2 L_1$. The weak formulation (1.41) remains the same but with other bilinear forms,

$$\begin{array}{c} \widetilde{a}^A(u_3^A,v_3^A) = \varepsilon^*\ell_2\int_0^{L_1}[\left(R^B\partial^2_{x_1x_1}u_3^A\partial^2_{x_1x_1}v_3^A\right)_{|\widetilde{Y}_B} \\ +\ell_C^0\int_0^{L_C^0}\overline{r^C}\partial^2_{y_2y_2}u_3^A\partial^2_{y_2y_2}v_3^A\ dy_2^C]dx_1. \end{array} \tag{1.60}$$

$$\begin{array}{c} c^A(u_3^A,v_3^A) = \varepsilon^*\ell_2\int_0^{L_1}[(\rho^B u_3^A v_3^A)_{|\widetilde{Y}_B} + \ell_C^0\int_0^{L_C^0} m^C u_3^A v_3^A\ dy_2^C \\ +\int_{Y_R}\rho^R u_3^A v_3^A\ dy]dx_1, \end{array} \tag{1.61}$$

and

$$l^A(v_3^A) = \varepsilon^* \ell_2 \int_0^{L_1} [(f^B v_3^A - g^B \nabla_{\widetilde{x}} v_3^A)_{|\widetilde{Y}_B} + \int_{\widetilde{Y}_C} F^C \; v_3^A - G_2^C \partial_{y_2} v_3^A \; d\widetilde{y} + \int_{Y_R} F^R v_3^A - G_2^R \partial_{y_2} v_3^A \; dy] dx_1 + (F^D - G^D) v_3^A. \tag{1.62}$$

The eigenvalue problem in ψ^A and λ^A keeps the same expression, and the resulting decomposition of the solution, which is a function of (t, x_1, y_2) only, states as

$$u_3^A(t, x_1, y_2) = \sum_k u_{3k}^A(t) \psi^A(x_1, y_2).$$

Here, $\psi^A(\widetilde{x}, \widetilde{y}) = \varphi^B(\frac{x_1}{L_1}) \varphi^C(\frac{y_2^C}{L_C^0})$ where φ^B and λ^B are solution to the macroscopic eigenvalue problem (1.46) in $H_0^2(0,1)$ with the bilinear forms

$$a^B(\varphi^B, v^B) = \int_0^1 \partial_{\xi\xi}^2 \varphi^B \partial_{\xi\xi}^2 v^B \; d\xi \text{ and } c^B(\varphi^B, v^B) = \int_0^1 \varphi^B \; v^B \; d\xi. \tag{1.63}$$

Next, $\varphi^C \in V^C$ with λ^C are solution to the eigenvalue problem (1.49) with $R^B_{\max}$ replaced by R^B in the expression of $a^C(.,.)$. The associated normalization condition and the boundary value problem are formally unchanged, excepted that $R^B_{\max}$ and μ are replaced by R^B_{1111} and L_1 respectively in the second boundary conditions at $\xi = 0$:

$$\frac{R^B_{1111} (L_C^0)^4 m^C}{\overline{r^C} L_1^4 \rho^B} \lambda^B \varphi^C + \frac{m^C \ell_C^0 L_C^0}{\rho^B} \partial_{\xi\xi\xi}^3 \varphi^C = \lambda^C \varphi^C \text{ at } \xi = 0. \tag{1.64}$$

The cell problem is kept the same excepted that the matrix ζ in the right hand side has a vanishing ζ_{22} component. When $\widetilde{Y}_B$ is a rectangle, the exact expression of w^B, $\mathcal{L}^B$ and of R^B_{1111} can be derived. Precisely, the solution to the cell problem is

$$w^B(y_1, y_2) = -\frac{\nu \zeta_{11}}{2} y_2^2 \text{ and } M^B = -\frac{\widetilde{\kappa} E_B h_B^3 \nu \zeta_{11}}{12(1-\nu^2)} \begin{pmatrix} \nu & 0 \\ 0 & 1 \end{pmatrix}.$$

The linear operator $\mathcal{L}^B_{\alpha\beta\gamma\rho} = -\nu \delta_{\alpha 2} \delta_{\beta 2} \delta_{\gamma 1} \delta_{\rho 1}$, which implies the expression of $R^B = \int_{\widetilde{Y}_B} r^B + r^B \mathcal{L}^B \; d\widetilde{y}$,

$$R^B_{\alpha\beta\gamma\rho} = \frac{\widetilde{\kappa} |\widetilde{Y}_B| E_B h_B^3}{12(1+\nu)} \left(\frac{\nu}{1-\nu} \delta_{\alpha\beta} \delta_{\gamma\rho} + \delta_{\alpha\gamma} \delta_{\beta\rho} - \frac{\nu^2}{1-\nu} \delta_{\alpha\beta} \delta_{\gamma 1} \delta_{1\rho} + \nu \delta_{\alpha 2} \delta_{2\beta} \delta_{\gamma 1} \delta_{1\rho} \right),$$

then

$$R^B_{1111} = \frac{\ell_B^0 E_B h_B^3}{12 \ell_2}$$

where ℓ_B^0 is the width of $\widetilde{Y}_B$.

In the load expressions (1.57) $\widetilde{x}$ is replaced by x_1, so

$$\begin{aligned}
\widehat{f}_3(t,x_1,y) &= f_3^0(x_1,y)f^{B2}(t),\\
\widehat{f}_\alpha(t,x_1,y) &= f_\alpha^0(x_1,y)g_\alpha^{B2}(t) \text{ in } Y_B,\\
\widehat{f}_3(t,x_1,y_2,y_3) &= F^{C0}(x_1)f_3^{C1}(y_2,y_3)F^{C2}(t),\\
\widehat{f}_2(t,x_1,y_2,y_3) &= G^{C0}(x_1)f_2^{C1}(y_2,y_3)G^{C2}(t) \text{ in } Y_C,\\
\widehat{f}_3(t,x_1,y) &= F^{R0}(x_1)f_3^{R1}(y)F^{R2}(t),\\
\widehat{f}_2(t,x_1,y) &= G^{R0}(x_1)f_2^{R1}(y)G^{R2}(t) \text{ in } Y_R,\\
\widehat{f}_i^{tip}(t,x_1,y) &= \sum_c f_{ic}^{tip}(t)\delta_{x_1^c}(x_1)\delta_{y^{tip}}(y).
\end{aligned}$$

Thus, the right hand side of the modal equation (1.56) is

$$\begin{aligned}
l^A(\psi^A) = {}& \varepsilon^*\ell_2 \textstyle\int_0^{L_1} f^{B0}\varphi^B\, dx_1\ \varphi^C(0)f^{B1}f^{B2}(t)\\
&-\textstyle\sum_\alpha \varepsilon^*\ell_2 \int_0^{L_1} g_\alpha^{B0}\frac{\partial_{\xi_\alpha}\varphi^B}{L_\alpha}\, dx_1\ \varphi^C(0)g_\alpha^{B1}g_\alpha^{B2}(t)\\
&+\varepsilon^*\ell_2 \textstyle\int_0^{L_1} F^{C0}\varphi^B\, dx_1 \int_0^{L_C^0} F^{C1}\varphi^C\, dy_2^C F^{C2}\\
&-\varepsilon^*\ell_2 \textstyle\int_0^{L_1} G^{C0}\varphi^B\, dx_1 \int_0^{L_C^0} G^{C1}\frac{\partial_\xi\varphi^C}{L_C^0}\, dy_2^C G^{C2}\\
&+\varepsilon^*\ell_2 \textstyle\int_0^{L_1} F^{R0}\varphi^B\, dx_1 \int_{Y_R} F^{R1}\varphi^C\, dy F^{R2}\\
&-\varepsilon^*\ell_2 \textstyle\int_0^{L_1} G^{R0}\varphi^B\, dx_1 \int_{Y_R} G^{R1}\frac{\partial_\xi\varphi^C}{L_C^0}\, dy_2^C G^{R2}\\
&+\textstyle\sum_c F_c^D\psi^A(x^c,y^{tip}) - G_c^D\partial_{y_2}\psi^A(x^c,y^{tip}).
\end{aligned} \tag{1.65}$$

1.3 Base/Cantilever Displacement Decomposition of the *Simple Model*

In this section, we propose a new approach based on base and cantilever displacement decomposition instead of global modal decomposition for the *Simple Model* of one-dimensional cantilever array. We recall that the global modal decomposition

$$u_3^A(t,x_1,y_2) = \sum_k U_k(t)\psi_k^A(x_1,y_2),$$

where the global eigenvector

$$\psi^A(\widetilde{x},\widetilde{y}) = \varphi^B(\frac{x_1}{L_1})\varphi^C(\frac{y_2^C}{L_C^0}),$$

as introduced in section 1.2.2. We have observed that the global approximation with ψ^A for the number of base modes $n^B = 10$ and the number of cantilever modes $n^C = 3$ is not very good, as shown in Figure 1.5.

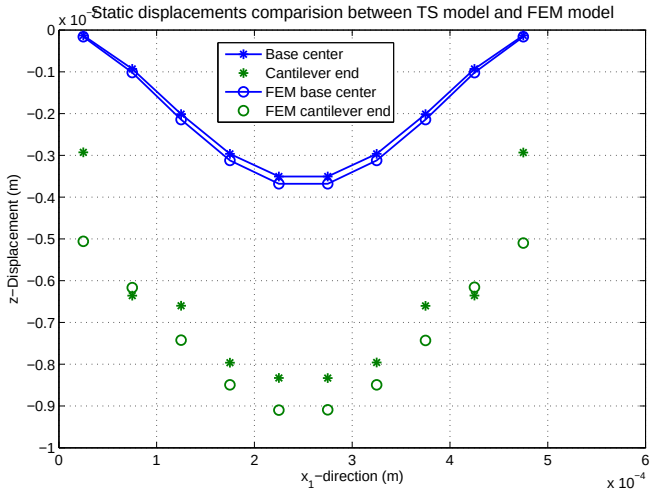

Figure 1.5: Static displacements comparison between FEM model and two-scale model with global modal decomposition.

We remark that the approximation based on global modal decomposition gets worse with increasing n^B and n^C. This is due to the coupling in ψ^A of the micro and macro modes. We note that the eigenvector of cantilever φ^C depends on the eigenvalue of base λ^B, see the boundary condition (1.64). Thus, φ^C is not a pure cantilever mode. It seems that a solution with discoupled modes works better.

We introduce the extension $y_2 \mapsto \overline{u}(.,y_2)$ of the restriction $y_2 \mapsto u^A_{3|base}(.,y_2)$ the displacement in base (which is in fact independent of y_2) to the values taken by y_2 in cantilevers. So, $\overline{u}$ is defined in the whole two-scale domain and we can define its difference with u^A_3, $\widetilde{u} = u^A_3 - \overline{u}$, also defined in the whole domain. In the base, it is obvious that $\widetilde{u} = 0$ and $\nabla_y \overline{u} = 0$ since u^A_3 is independent of y_2. We reformulate the equations (1.5) and (1.4) for one-dimensional cantilever arrays, satisfied by the couple $(\overline{u}, \widetilde{u})$,

$$\left\{ \begin{array}{l} \rho^B \partial^2_{tt} \bar{u} + R^B \partial^4_{x_1 \cdots x_1} \bar{u} + \ell^0_C r^C (\partial^3_{y_2 y_2 y_2} \widetilde{u})_{|junction} = f^B, \text{ in base} \\ m^{C0} \partial^2_{tt} \widetilde{u} + m^{C0} \partial^2_{tt} \bar{u} + r^{C0} \partial^4_{y_2 \ldots y_2} \widetilde{u} = F^C, \text{ in cantilever} \end{array} \right. \tag{1.66}$$

In practice, we will work on a model reduced at the microscopic scale through modal decompositions on cantilever modes $\{\phi_k(y_2)\}_{k=1..n^C}$ in $L^2(0, L^0_C)$, where n^C is the number of cantilever modes and the parameter L^0_C represent the cantilever length in the microscale domain. We have

$$\widetilde{u}(t,x_1,y_2) \approx \sum_{k=1}^{n^C} \widetilde{u}_k(t,x_1)\phi_k(y_2) \text{ and } F^C(t,x_1,y_2) \approx \sum_{k=1}^{n^C} f^C_k(t,x_1)\phi_k(y_2). \tag{1.67}$$

In this approximation, equations (1.66) yields,

$$\left\{\begin{array}{l} \rho^B\partial^2_{tt}\overline{u} + R^B\partial^4_{x_1\cdots x_1}\overline{u} + \ell^0_C r^C(\partial^3_{y_2y_2y_2}\widetilde{u})_{|junction} = f^B \text{ in base,} \\ m^{C0}\partial^2_{tt}\widetilde{u}_k + m^{C0}\partial^2_{tt}\bar{u}\bar{\phi}_k + r^{C0}\frac{\lambda^C_k}{(L^0_C)^4}\widetilde{u}_k = f^C_k \text{ for each } k, \end{array}\right. \tag{1.68}$$

where $\bar{\phi}_k = \int_0^{L^0_C}\phi_k\ dy_2$ and $\phi_k(y_2) = \varphi_k(\frac{y_2}{L^0_C})$. The eigenelements $(\lambda_k,\varphi_k)_{k\in\mathbb{N}}$ are solutions to the eigenvalue problem, posed in $(0,1)$,

$$\left\{\begin{array}{l} \varphi_k'''' = \lambda^C_k\varphi_k \quad \text{in } (0,1) \\ \varphi_k(0) = \varphi_k'(0) = 0, \quad \text{at } 0 \\ \begin{pmatrix} -\varphi_k''' \\ \varphi_k'' \end{pmatrix} = \lambda_k Q \begin{pmatrix} \varphi_k \\ \varphi_k' \end{pmatrix} \quad \text{at } 1. \end{array}\right. \tag{1.69}$$

where $Q = N\begin{pmatrix} J_0 & J_1 \\ J_1 & J_2 \end{pmatrix}N$ with $N = \begin{pmatrix} 1 & 0 \\ 0 & 1/L^0_C \end{pmatrix}$ and $J_i = \int_{Y_R}(y_2 - L^0_C)^i\ dy$, $i = \{0,1,2\}$.

The weak formulation associated to (1.68) states as,

$$\begin{array}{l} \varepsilon^*\ell_2\int_0^{L_1}[\left(\left(\rho^B + \ell^0_C L^0_C m^{C0}\right)\partial^2_{tt}\bar{u}\bar{v} + R^B\partial^2_{x_1x_1}\bar{u}\partial^2_{x_1x_1}\bar{v}\right)|_\Gamma + \ell^0_C\int_0^{L^0_C} m^{C0}\partial^2_{tt}(\tilde{u}\bar{v} + \bar{u}\tilde{v} + \tilde{u}\tilde{v}) \\ +r^{C0}\partial^2_{y_2y_2}\tilde{u}\partial^2_{y_2y_2}\tilde{v}\ dy_2]dx_1 = \varepsilon^*\ell_2\int_0^{L_1}[(f^B\bar{v})|_\Gamma + \ell^0_C\int_0^{L^0_C} f^C(\bar{v}+\tilde{v})\ dy_2]dx_1 + F^D(\bar{v}+\tilde{v}), \end{array} \tag{1.70}$$

which is satisfied by the couple $(\bar{u},\tilde{u})$. In the following, we show that the displacements in base $\bar{u}$ are solved by a classical FEM, and the displacements in cantilevers $\tilde{u}$ are solved by using the modal decomposition introduced in (1.67).

1.3.1 FEM discretization in Base

We use a FEM to approximate, $\bar{u}$, the solutions in base. The normalized interval $[0,1]$ is discretized by elements $e_i = [\zeta^i_1, \zeta^{i+1}_1]$ with $i \in \{1,\cdots N^e\}$, and the ends of the nodes are $0 < \zeta^1_1 < \zeta^2_1 < \cdots < \zeta^{N+1}_1 = 1$. We approximate the solution by a function of the class $\mathcal{C}^1(0,1)$ and third order polynomials on each elements, $\bar{u}_h \in \mathcal{P}^3(0,1)$. The global degree of freedoms are the displacements and the derivatives at each nodes, $\bar{u}_{2n-1} = u_h(\eta_n)$ and $\bar{u}_{2n} = u_h'(\eta_n)$ for $n = 1,\cdots,N^e+1$, and in total there are $2(N^e+1)$ degree of freedoms.

The local degrees of freedom are the displacements and derivatives at nodes

$$\bar{u}^{e_i}_1 = \bar{u}_h(\xi^{e_i}_1),\ \bar{u}^{e_i}_2 = \bar{u}_h'(\xi^{e_i}_1),\ \bar{u}^{e_i}_3 = \bar{u}_h(\xi^{e_i}_2),\ \bar{u}^{e_i}_4 = \bar{u}_h'(\xi^{e_i}_2),$$

where $\xi^{e_i}_1 = \zeta^i_1$, $\xi^{e_i}_2 = \zeta^{i+1}_1$. The shape functions are $N_k(\xi)$:

$$\begin{aligned} N_1(\xi) &= \frac{-(\xi-\xi_2)^2(-h+2(\xi_1-\xi))}{h^3},\ N_2(\xi) = \frac{(\xi-\xi_1)(\xi-\xi_2)^2}{h^2}, \\ N_3(\xi) &= \frac{(\xi-\xi_1)^2(h+2(\xi_2-\xi))}{h^3},\ N_4(\xi) = \frac{(\xi-\xi_1)^2(\xi-\xi_2)}{h^2} \end{aligned}$$

The local and global approximations are represented,

$$\bar{u}_{e_i}(t,\zeta_1) = N^T(\zeta_1)U^{e_i}(t) \text{ in } e_i \text{ where } U^{e_i} = (\bar{u}_1^{e_i}, \bar{u}_2^{e_i}, \bar{u}_3^{e_i}, \bar{u}_4^{e_i})^T \tag{1.71}$$

and

$$\bar{u}_h(t,\zeta_1) = \sum_{n=1}^{2(N^e+1)} \bar{u}_n(t)\phi_n(\zeta_1).$$

1.3.2 Modal decomposition in Cantilevers

As indicated at the beginning of section 1.3, the solutions in the cantilevers are decomposed $\tilde{u}$ by

$$\widetilde{u}(t,x_1,y_2) \approx \sum_{k=1}^{n^C} \widetilde{u}_k(t,x_1)\phi_k(y_2) \tag{1.72}$$

with $\phi_k(y_2) = \varphi_k(\frac{y_2}{L_C^0})$. Here, the basis φ_k is the solution of eigenvalue problem with fixed-free boundary condition (1.69) instead of the boundary condition (1.53) for φ^C based on global modal decomposition.

The approximation of the integrals by Galerkin method for (1.70):

$$\left[M_{sys}\partial_{tt}^2 \begin{pmatrix} \overline{U} \\ \widetilde{U}_1 \\ \vdots \\ \widetilde{U}_{n^C} \end{pmatrix} + K_{sys} \begin{pmatrix} \overline{U} \\ \widetilde{U}_1 \\ \vdots \\ \widetilde{U}_{n^C} \end{pmatrix} \right] = F_{sys}, \tag{1.73}$$

where the vectors of the coefficients $\overline{U} = \begin{pmatrix} 0 & 0 & \bar{u}_3 & \bar{u}_4 & \cdots & \bar{u}_{2N^e-1} & \bar{u}_{2N^e} & 0 & 0 \end{pmatrix}^T$ and $\widetilde{U}_k = \begin{pmatrix} 0 & 0 & \tilde{u}_{k,2} & \tilde{u}_{k,2} & \cdots & \tilde{u}_{k,2N^e-1} & \tilde{u}_{k,2N^e} & 0 & 0 \end{pmatrix}^T$ for k varying from 1 to n^C. The matrices

$$\begin{aligned} M_{sys} &= |\omega| \begin{pmatrix} \left(\rho^B + \ell_C^0 L_C^0 m^{C0}\right) M_B & (\bar{\varphi}_k)_{k=1,\ldots,n^C} \ell_C^0 L_C^0 m^C M_B \\ (\bar{\varphi}_k)^T_{k=1,\ldots,n^C} \ell_C^0 L_C^0 m^{C0} M_B & \ell_C^0 L_C^0 m^{C0} Id \end{pmatrix}, \text{ and} \\ K_{sys} &= |\omega| \begin{pmatrix} \frac{K_B}{L_1^4} & 0 \\ 0 & \frac{\ell_C^0 r^{C0}}{(L_C^0)^3}(\lambda_k^C)_{k=1,\cdots,n^C} \end{pmatrix}. \end{aligned}$$

where the rectangle domain $\omega = (0, L_1)\times(0, \varepsilon^*\ell_2)$, the matrices $M_B = \sum_{i=1}^{N^e} \int_{e_i} N(\xi)N^T(\xi)$ $d\xi$, $K_B = \sum_{i=1}^{N^e} \int_{e_i} N''(\xi)N''^T(\xi)\, d\xi$, and Id is identity matrix with size of $n^C \times 2(N^e + 1)$.

1.4 Conclusion

In this chapter, we have presented a two-scale model for two-dimensional arrays of cantilevers in dynamic regime based on a theory of strongly heterogeneous homogenization. We have also considered the dynamics of the possible interaction between the rigid tips and the objects in the *General Model*. The model implementation has been reported both for one-dimensional and two-dimensional arrays of cantilevers. We have proposed a new approach of base/cantilever displacement decomposition which is different from the approach based on the decomposition on the global modes ψ^A.

In the next chapter, we shall focus on the model verification and it will be followed by a presentation of design optimization for arrays of AFMs.

Chapter 2

MODEL VERIFICATION AND DESIGN OPTIMIZATION FOR AFM ARRAYS

Contents

In chapter 1, we presented the *Simple Model* and the *General Model* for two-dimensional cantilever arrays. We also detailed the model implementation and the model decomposition of the *Simple Model*. In this chapter, we conduct the verification of the two-scale model. It includes the following contents.

1. Eigenvalue and eigenmode shape comparison between the two-scale model and a direct Finite Element Model both for one-dimensional and two-dimensional cantilever arrays.

2. Verifications in static and dynamic regime for one-dimensional array of cantilevers.

Additionally, an optimization tool is presented. It has been used for designing arrays of cantilevers satisfying all the design requirements.

2.1 Simple Model Verification

2.1.1 Qualitative Properties of the Modal Structure of Cantilever Arrays

An infinite number of eigenvalues λ^A and eigenvectors $\varphi^A(\widetilde{x}, y_2)$ are solutions to the eigenvalue problem (1.45), which are associated to the model of two-dimensional array of cantilevers. For convenience, we parameterize them by two independent indices, $i \in \mathbb{N}$ and $j \in \mathbb{N}$, both varying in an infinite countable set. The first index i refers to an infinite set of eigenvalues λ_i^B and eigenvectors $\varphi_i^B(\widetilde{x})$ of a problem posed in the base. The eigenvalues $(\lambda_i^B)_{i\in\mathbb{N}}$ constitutes a sequence of positive number increasing towards infinity. At each such eigenvalue, another eigenvalue problem is posed for a cantilever, which also has a countable infinity of solutions denoted by λ_{ij}^C and $\varphi_{ij}^C(y_2)$. The index i of λ_i^B being fixed, the sequence $(\lambda_{ij}^C)_{j\in\mathbb{N}}$ is a positive sequence increasing towards infinity. On the other hand, when the index j is fixed, the sequence $(\lambda_{ij}^C, \varphi_{ij}^C)_{i\in\mathbb{N}}$ is an infinite sequence converging to an eigenelement associated to a clamped-free cantilever. We can show that the eigenvectors $\varphi_{ij}^A(\widetilde{x}, y_2)$ are the product of a mode in the base by a mode in a cantilever $\varphi_i^B(\widetilde{x})\varphi_{ij}^C(y_2)$. Note that $\widetilde{x}$ is replaced by x_1 for the model of one-dimensional array of cantilevers. Now we report observations made on eigenmode computations.

Verification for Eigenvalues of One-dimensional Array of Cantilevers

We consider an array of $N = 10$ cantilevers, with base dimensions $500\mu m \times 16.7\mu m \times 10\mu m$, and cantilever dimensions $41.7\mu m \times 12.5\mu m \times 1.25\mu m$, (see Figure 2.1) for the two possible geometries, with or without tips. We have carried out our numerical study on both cases, with or without tips. But we limit the following comparisons to cantilevers without tips, because configuration including tips yields similar results.

We restrict our attention to a finite number of eigenvalues λ_i^B with i varying from 1 to n^B. Computing the eigenvalues λ^A, we observe that they are grouped in bunches of size n^B accumulated around a clamped-free cantilever eigenvalues. A number of eigenvalues are isolated far from the bunch. It is remarkable that

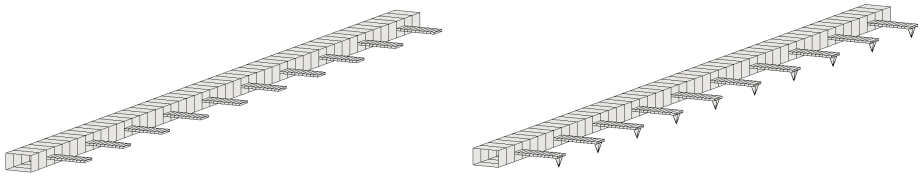

(a) (b)

Figure 2.1: Cantilever array without tips (a) and with tips (b)

the eigenelements in a same bunch share a same cantilever mode shape, (close to a clamped-free cantilever mode) even if they correspond to different indices j. That is why, these modes will be called *"cantilever modes"*, (see Figure 2.2 (a)). Isolated eigenelements share also a common cantilever shape, which looks like a first clamped-free cantilever mode shape except that the clamped side is shifted far from zero. The induced global mode φ^A is then dominated by base deformations and therefore will be called *"base modes"*, see Figure 2.2 (b).

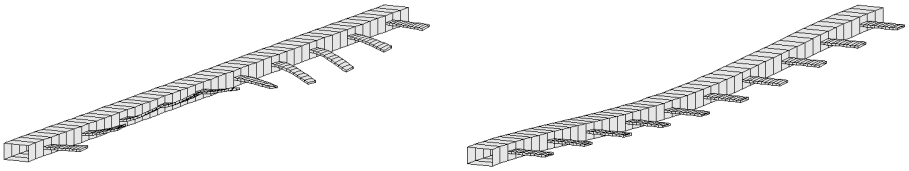

(a) (b)

Figure 2.2: Cantilever mode (a) and Base mode (b)

Then, for arrays of 15 and 20 cantilevers, only the cantilever width is changed so that to keep the same characteristic values of λ^A_{ij}. The densities of square roots of eigenvalues in logarithm scale are presented in the sub-figures $2, 4$ and 6[1] of Figure 2.3 for the number of base modes $n^B = 10, 15$ and 20 respectively. These figures show three bunches with size n^B and isolated modes that remain unchanged.

[1]Sub-figures are counted from top to bottom.

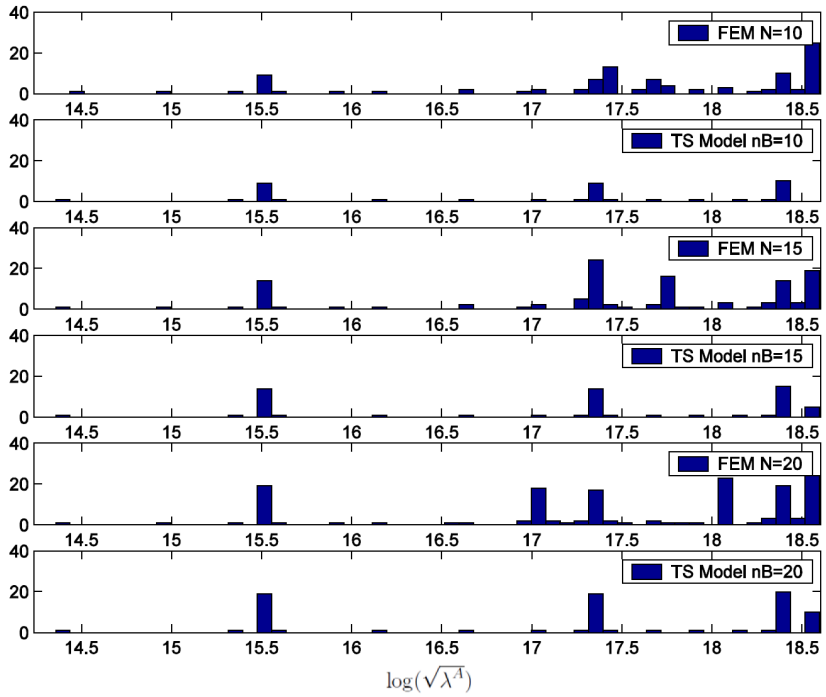

Figure 2.3: Distributions of $\log(\sqrt{\lambda^A})$ of the FEM model and of the two-scale model

Verification for Eigenvalues of a Two-dimensional Array of Cantilevers

In this section, we show our preliminary work on the eigenmode and eigenvalue verifications for a two-dimensional array of $N \times N$ cantilevers without tips, (see Figure 1.1). We have carried our computation with small number $N = 3, 4$ and 5 due to long computing time of FEM simulations on a personal computer. Thanks to super computer facilities of the *Mésocentre de calcul de Franche-Comté*, we have performed a simulation for $N = 10$. We consider an array of cantilever with base dimensions of left base $30\mu m \times 10\mu m \times 10\mu m$, right base $30\mu m \times 10\mu m \times 10\mu m$, top base $50\mu m \times 10\mu m \times 10\mu m$, bottom base $50\mu m \times 10\mu m \times 10\mu m$ and of cantilever dimensions $25\mu m \times 10\mu m \times 1.25\mu m$ for one cell. Here, we still focus on the comparisons where cantilevers are without tips as for one-dimensional arrays of cantilevers.

Densities of square roots of eigenvalues in logarithm are reported in sub-figures 2, 4 and 6 of Figure 2.4 for $N = 3, 4$ and 5 respectively. These figures show two bunches with size of the number of base mode n^B and the isolated modes that remains unchanged.

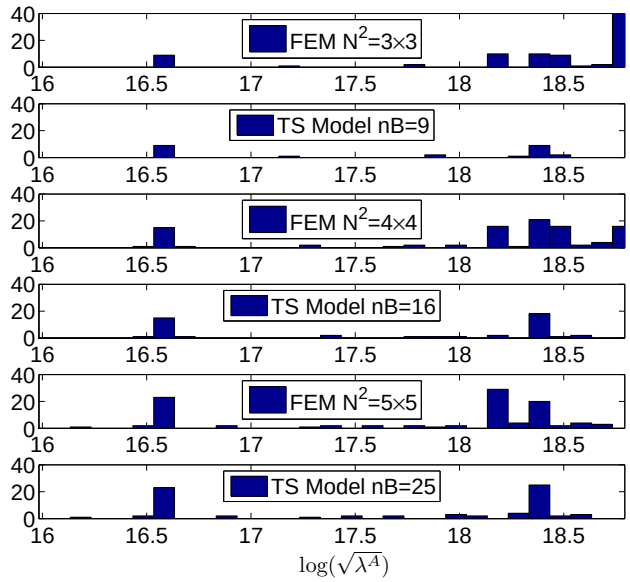

Figure 2.4: Eigenvalue density comparison for $N = 3, 4$ and 5

We report the eigenmode density comparison for $N = 10$ in Figure 2.5.

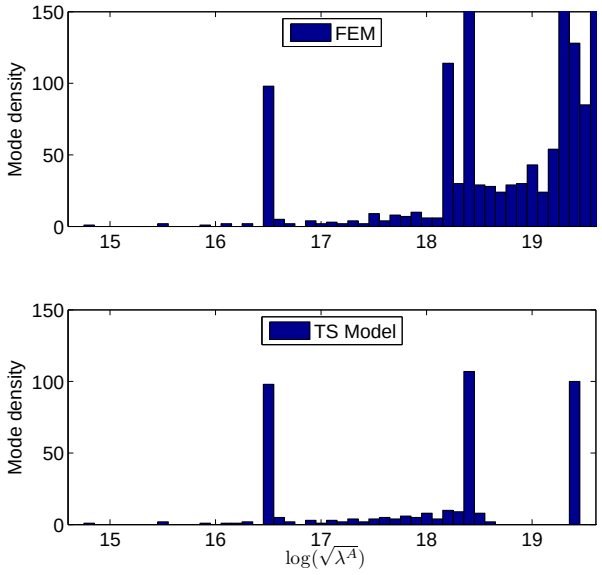

Figure 2.5: Eigenvalue density comparison for $N = 10$

The first bunch with size $N \times N$ and the isolated modes that remains un-

changed. We remark that a number of eigenvalues in the FEM spectrum do not have their counterparts in the two-scale model spectrum for $\log(\sqrt{\lambda^A}) > 18$. We have checked that these missing elements correspond to modes which have membrane displacement in some local cells and torsion in the cantilevers. These cases are not modeled in the current simple two-scale model.

We also compare the eigenmodes and especially those belonging to bunches of eigenvalues, (see Figure 2.6 for $N = 10$). We have found that the mode shapes of the FEM model and of our model are similar for identical eigenvalues.

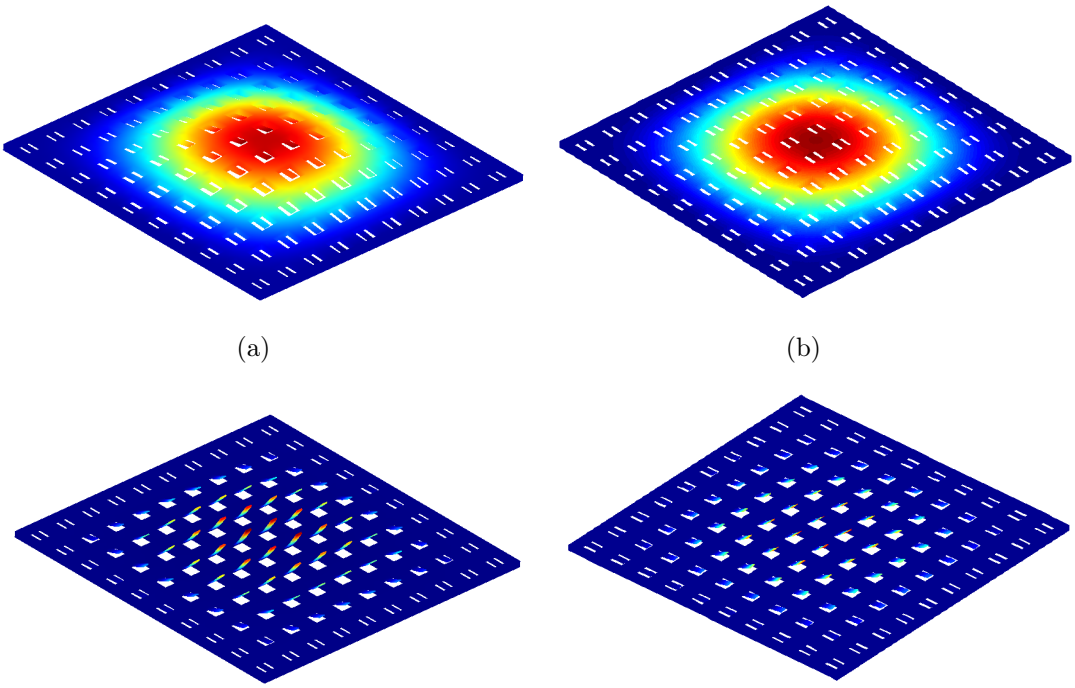

(a) (b)

(c) (d)

Figure 2.6: The first *base* mode of (a) FEM model and (b) Two-scale model. The first *cantilever* mode of (c) FEM model (d) Two-scale model

In order to compare the distribution of the spectrum for a 100-cantilever array, we operate a truncation of mode list. It corresponds to the range [0 17.46] of $\log(\sqrt{\lambda^A})$ in Figure 2.5. We have reported the eigenvalue distribution both in our model and in the FEM model, see Figure 2.7 (a). The relative errors between both eigenvalues sequences are represented in Figure 2.7 (b). Note that errors are far from being uniform among eigenvalues. In fact, the main error source resides in a poor precision of the beam model for representing base deformations in some particular deformation modes.

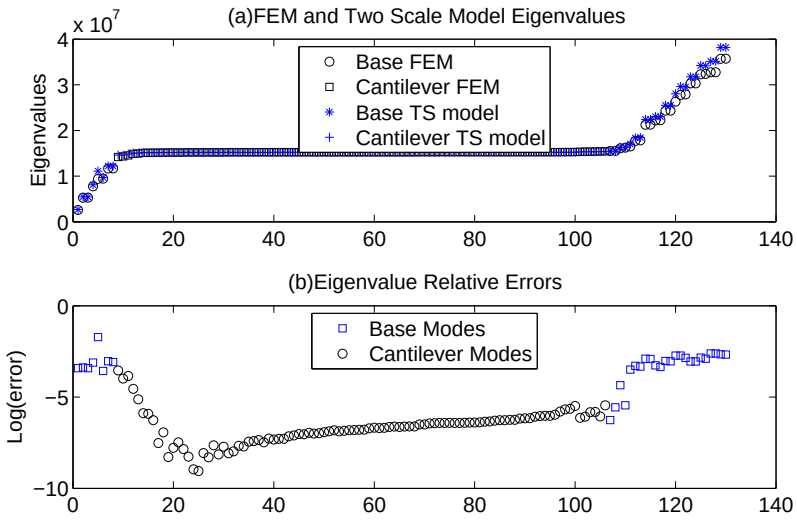

Figure 2.7: (a) Eigenvalue density distributions and (b) its relative errors for the FEM model and for the two-scale model

Verification for eigenmodes

We discuss the comparison with the modal structure of the three-dimensional linear elasticity system for the cantilever array discretized by a standard FEM analysis both for two-dimensional and one-dimensional arrays of cantilevers. The eigenvalues of the three-dimensional elasticity equations constitute also an increasing positive sequence that accumulates at infinity. As for the two-scale model, its density distribution exhibits a number of concentration points and also some isolated values. Here bunch sizes equal the number of cantilevers, see sub-figures 1, 3 and 5 in Figure 2.3, Figure 2.4 (a) and sub-figure 1 in Figure 2.4 (b) representing eigenmode distributions. Extrapolating this observation shows that when the number of cantilevers increases to infinity bunch size increases proportionally. Since the two-scale model is an approximation in the sense of an infinitely large number of cantilevers, this explains why the two-scale model spectrum exhibit mode concentration with infinite number of elements. This remark provides guidelines for operating mode selection in the two-scale model. In order to determine an approximation of the spectrum for an array of cantilevers, we suggest to operate a truncation in the mode list so that to retain a simple infinity of eigenvalues $(\lambda^A_{ij})_{i=1,..,N \text{ and } j\in\mathbb{N}}$. It is remarked that a number of eigenvalues in the FEM spectrum have not their counterparts in the two-scale model spectrum. We found that the missing eigenmodes in the two-scale model correspond to physical effects not taken into account in the two Euler-Bernoulli models for the base and the

cantilevers.

2.1.2 Quantitative Verification

The quantitative verification is focused on the case of a one-dimensional array with 10-cantilevers, i.e. for $N = 10$. The results relate to the first 40 modes in the FEM model and to the eigenelements $(\lambda_{ij}^A, \varphi_{ij}^A)$ for $i \in \{1, ..., 10\}$ and $j \in \{1, 2, 3\}$, the latter being listed in Table 2.1. Note that the computation time is $0.76s$ for the

Table 2.1: List of $\log(\sqrt{\lambda_{ij}^A})$ of the two-scale model

j\i	1	2	3	4	5	6	7	8	9	10
1	14.44	15.38	15.51	15.51	15.51	15.51	15.51	15.51	15.51	15.51
2	15.54	15.61	16.16	16.65	17.05	17.31	17.34	17.35	17.35	17.35
3	17.36	17.36	17.36	17.36	17.37	17.43	17.69	17.93	18.15	18.33

modes of the two-scale model implemented in a non optimized MATLAB® code versus $88.14s$ for the finite element modes using COMSOL® with $20,859$ quadratic elements with a regular laptop. We stress the fact that the $N-$eigenvalue bunches are not corresponding to a single row in Table 2.1 i.e. not corresponding to a single j. This is because the modes dominated by the deformation of base are interposed between the clusters of modes dominated by the deformations of cantilevers. The counterpart in terms of base modes is that they follow each other on consecutive columns but with possible line breaks.

To conduct a quantitative comparison of eigenvalues, it is required to match the modes of the two-scale model with those of the FEM model. Because of the proximity of many eigenvalues, a tool like the conventional Modal Assurance Criterion (MAC) is necessary to discriminate them, see [44]. For any couple of an eigenvector φ^A from the two-scale model and the transverse displacement component φ^{ref} of an eigenvector from the FEM model,

$$MAC_\varphi = \frac{|\left\langle \varphi^{ref^T}, \varphi^A \right\rangle)|^2}{|\left\langle \varphi^{ref^T}, \varphi^{ref} \right\rangle| \ \ |\left\langle \varphi^{A^T}, \varphi^A \right\rangle|},$$

it is equal to one if the shapes are identical and to zero when they are orthogonal in the sense of the inner product $\langle ., . \rangle$. Each subspace of eigenvectors φ^{ref} corresponding to a quasi-multiple eigenvalue is rotated so as to optimize the MAC matrix. The results are shown in Figure 2.8 where the modes φ^A are arranged in the order such that the index i varies faster than the index j. The inner product is based on a sum over 300 points distributed along six parallel lines in the base

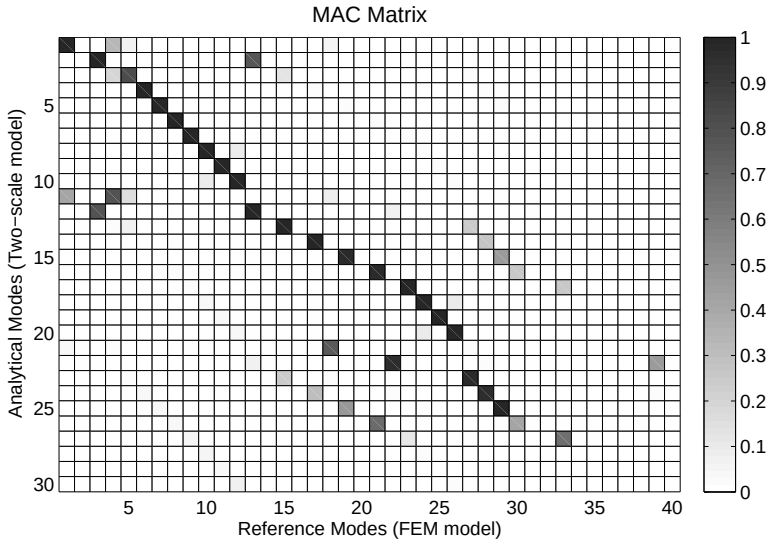

Figure 2.8: MAC matrix between the two-scale model modes and the FEM modes

and over $6 \times 10 \times N$ points along six lines in each cantilever. In both cases the six lines are along the four edges and along the central axes of the upper and lower faces and the points are regularly spaced. The FEM computation has been carried out with $20,859$ elements. All modes φ^{ref} from the FEM model which are not sufficiently correlated with a mode φ^{A} i.e. with a MAC lower than 0.5 are not considered for comparison because they correspond to physical effects not modeled by the Euler-Bernoulli models. Some modes φ^{A} seem to correlate well with several modes φ^{ref}, like the eigenmodes 2, 11 and 12 so an additional criterion for selection should be applied. The most general method would be to add more points in the inner product, but here it was enough to eliminate the unwanted modes by comparing the magnitudes of eigenvalues. Figures 2.9 (a) and (b) and 2.9 (c) and (d) are two examples of paired modes using this strategy. In Figure 2.10 (a) paired eigenvalues are represented and relative errors are plotted on Figure 2.10 (b). Note that errors are far from being uniform among eigenvalues. In fact, the main error source resides in a poor precision of the Euler-Bernoulli model for representing base deformations in few particular cases. A careful observation of Finite Element modes shows that base torsion can be predominant for some modes, such as in the first mode of the first cantilever mode bunch.

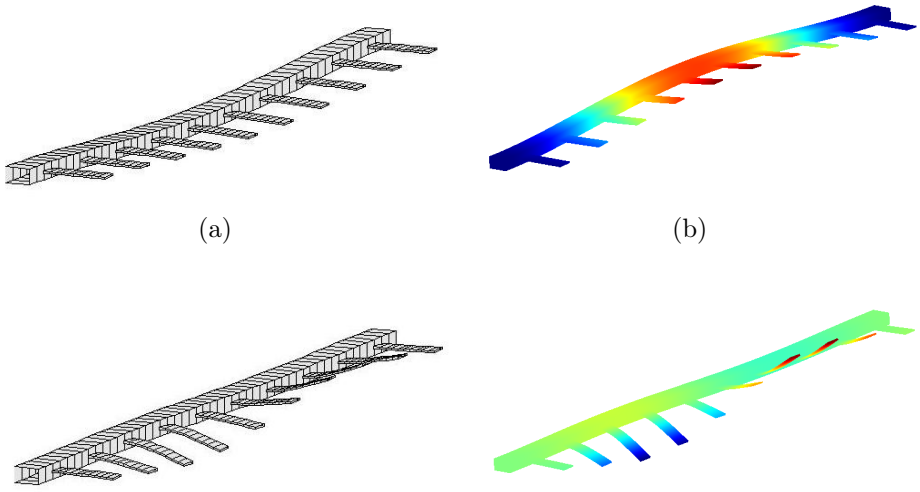

(a) (b)

(c) (d)

Figure 2.9: Eigenmode shapes of (a) $\varphi^A_{1,1}$, (b) φ^{ref}_1, (c) $\varphi^A_{2,2}$, (d) φ^{ref}_{13}

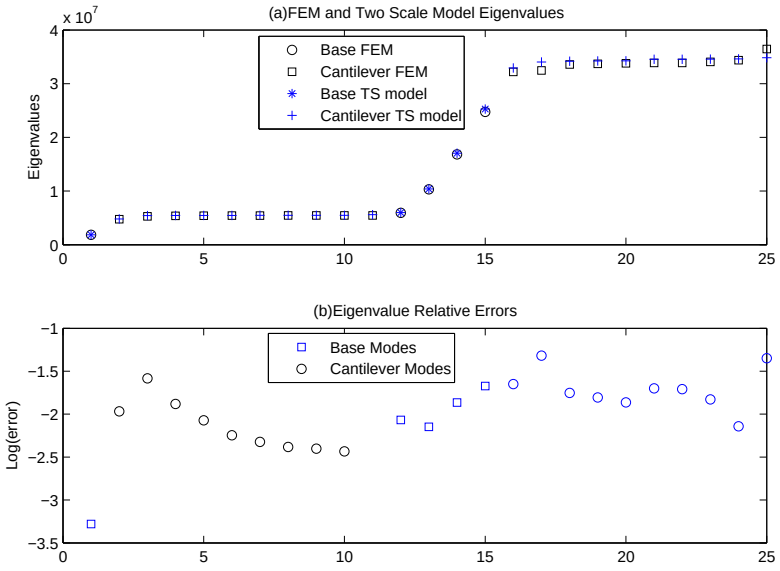

Figure 2.10: (a) Superimposed $\sqrt{\lambda^A}$ of the two-scale model with a selection of those of the finite element model, (b) Errors in logarithmic scale

In Figure 2.10(a), the distinction between the base modes and the cantilever

modes is also marked. Their distinction could be done from the ratio of the amplitudes of deformation in the base and in the cantilevers. An equivalent way is to use the sensitivities with respect to characteristic parameters of the two modes of deformations. To find the influential parameters, the sensitivities of the model through parameter variations is established using a first-order finite difference method applied to the eigenvalues. The results are presented in Figure 2.11 where all parameters have been tested, i.e. the Young's modulus, the volume mass, the thicknesses, the lengths and the widths.

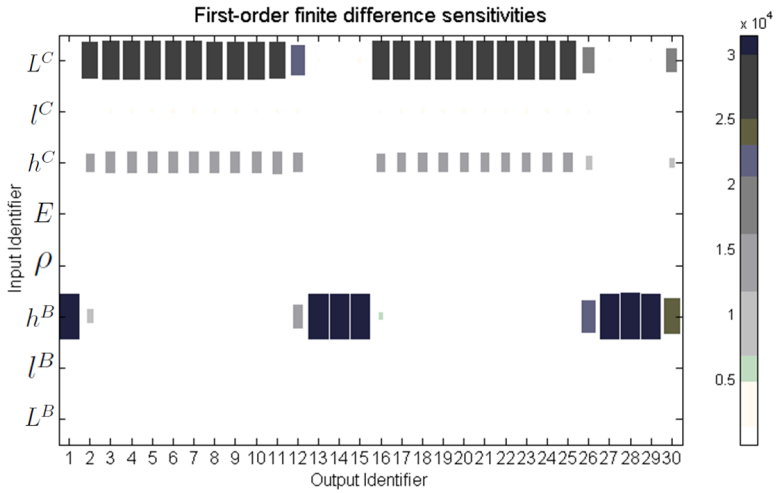

Figure 2.11: First-order finite difference sensitivity analysis

Their values are denoted by E, ρ, h^B, L^B, l^B, h^C, L^C, and l^C where the superscripts B and C stand for base and cantilevers. The eigenvalues are mainly sensitive to the thickness h^B of the base, to the length L^C of the cantilevers, and for a lesser extent to the thickness h^C of the cantilevers. Most of the eigenvalues are sensitive to only one of the two parameters h^B or L^C then they can be identified as a base mode or as a cantilever mode. The cantilever modes are clearly organized in clusters of $N = 10$ modes separated by base modes. At their interfaces some modes are almost equally sensitive to base and to cantilever parameters, they are referred as mixed mode in Figure 2.12. However, for simplicity they are considered as base modes in Figure 2.10.

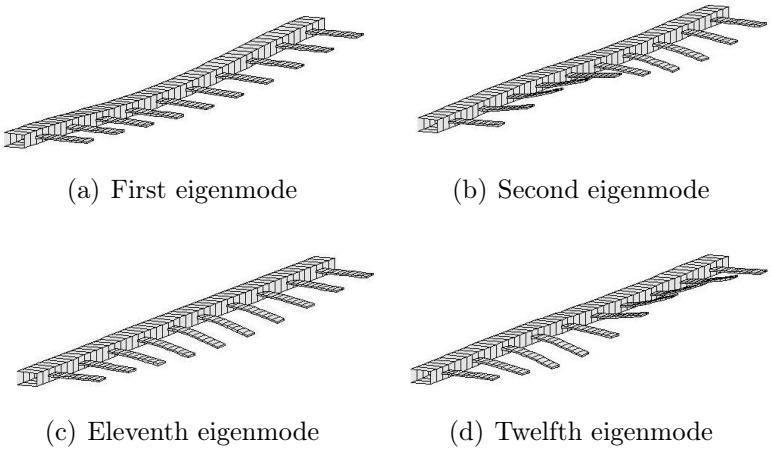

(a) First eigenmode (b) Second eigenmode

(c) Eleventh eigenmode (d) Twelfth eigenmode

Figure 2.12: Eigenmodes of the two-scale model

To illustrate the distinction between the three kind of modes, the sub-figures 2.12 (a) and (c) present a base mode and a cantilever mode when the sub-figures 2.12 (b) and (d) show two mixed modes.

2.2 Model Verification in Static and Dynamic Regime

We recall that we have introduced the base/cantilever displacement decomposition in section 1.3. In this section, we compare the reformulated two-scale model (a simplified model) to a FEM build from the system of elasticity equations in the three-dimensional domain. Here, we refine sufficiently the discretization of both models so that to evaluate the two-scale model itself but not its discretization. The solution of the FEM model is denoted by $u^{FEM.}$. Excepted when it is explicitly said, all computations are carried out for a 10-cantilever array.

2.2.1 Verification in Static Regime

The vertical displacement shown on Figure 2.13 are obtained after applying a $10\mu N$ concentrated force at the middle point of the free end of the fifth and sixth cantilevers. To better estimate the model quality, four loading conditions have been tested: A- Same load on all cantilevers, B- Only the fifth cantilever is loaded, C- The fifth and the sixth cantilevers are equally loaded, and D- Opposite loads on even and odd cantilevers. In table 2.2, the relative L^2-norm errors,

$$E = \left(\frac{\int_\omega |u - u^{FEM}|^2 \, dx}{\int_\omega |u^{FEM}|^2 \, dx} \right)^{1/2},$$

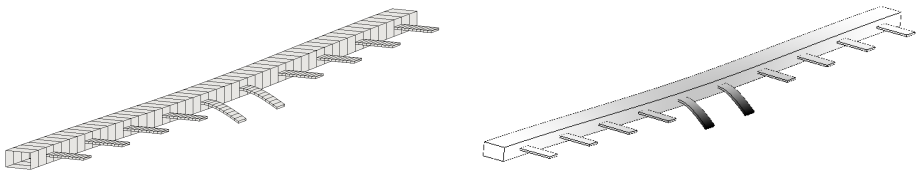

(a) (b)

Figure 2.13: Displacement of a 10-cantilever array under a static load of (a) Two-scale Model (b) FEM model

are reported. The errors of the model are small enough to use it in a model based

Table 2.2: L^2-norm error for different loads

Loads	A	B	C	D
Errors (%)	5.12	4.49	2.42	1.36

control loop. Deeper investigations show that the largest errors come when all loads are operating in the same direction and therefore when the base is subjected to a large deformation. Then, Figure 2.14 represents displacements in a single cantilever, namely the fifth cantilever, in the loading case A. We noticed that the

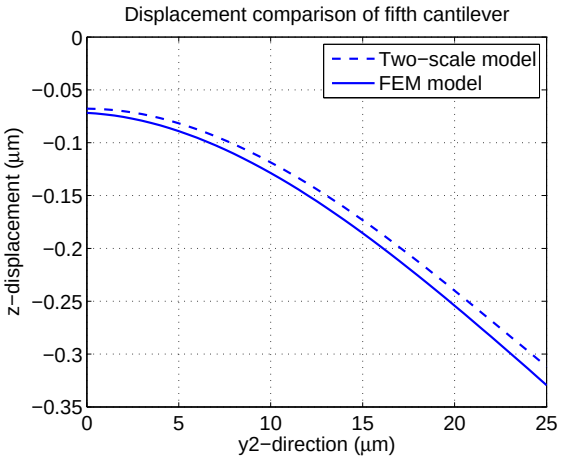

Figure 2.14: Displacement comparison of static analysis of 10-cantilever array at fifth cantilever

error originate from the clamping zone, and after a careful inspection we have concluded that it could have been corrected if torsion effects have been taken into account in the base.

Next, we report results of a study on static cross-talk effect. The load is this of case C. The ten ratios of the displacements at the free end of cantilevers to this of loaded cantilevers are reported in Table 2.3, they show a good agreement between the two models in terms of static cross-talk.

Table 2.3: Ratios of the displacements at the free end of cantilevers to this of a loaded one in static regime

Free ends	Two-scale model (%)	FEM model (%)	Absolute errors
1	0.6	0.9	0.3
2	4.9	5.9	1
3	11.3	13	1.7
4	17.7	20	2.3
5	100	100	0
6	100	100	0
7	17.7	20.1	2.4
8	11.3	13	1.7
9	4.9	5.9	1
10	0.6	0.9	0.3

2.2.2 Verification in Dynamic Regime

To study the dynamic regime, the fifth cantilever free end is excited with a load oscillating to the first base eigenfrequency ($303kHz$). Figure 2.15 shows the sixth and ninth cantilever end motion for both models.

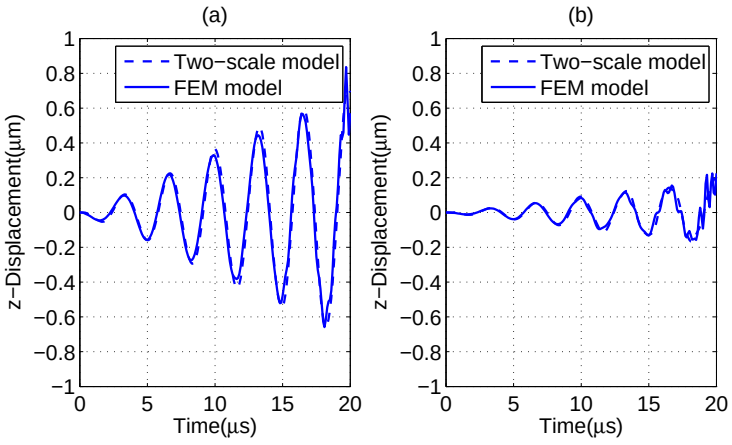

Figure 2.15: Displacement at (a) sixth cantilever end, and (b) ninth cantilever end in dynamic regime

We conclude to a good fit between the models in terms of phase shift but a noticeable difference regarding amplitudes. In the same experiment, dynamic cross-talk is characterized through the ratios of maximum displacements at the cantilever free ends to this of a loaded one. They are reported in Table 2.4 where the maximum displacements are taken over the time interval $[0, 15\mu s]$. In that

Table 2.4: Ratios of maximum displacements at the free end of cantilevers to this of a loaded one under first base eigenfrequency excitation

Free ends	Two-scale model (%)	FEM model (%)	Absolute errors
1	3.1	2.4	0.7
2	23.2	21.5	1.7
3	51.6	47.9	3.7
4	77.2	71.5	5.7
5	100	100	0
6	92.5	86.8	5.7
7	77.5	73.7	3.8
8	51.6	49.9	1.7
9	23.3	22.5	0.8
10	3.1	2.5	0.6

case, the observations show that the energy originating from an excited cantilever propagates more than in the static operating regime. Finally, Table 2.5 reports results of dynamic cross-talk effect when the fifth cantilever is excited at the first cantilever frequency $(2.34MHz)$. In this case, the simulation have been carried out in the time interval $[0, 2\mu s]$. As expected, the dynamic cross-talk effect, at this frequency, is smaller than this at the first base frequency. However, the absolute errors is increasing due to the poor precision of the beam model when exciting the cantilever at high frequency.

Table 2.5: Ratios of maximum displacements at the free end of cantilevers to this of a loaded one under first cantilever eigenfrequency excitation

Free ends	Two-scale model (%)	FEM model (%)	Absolute errors
1	1.2	3.6	2.4
2	4.9	9.3	4.4
3	2.6	18.3	15.7
4	5.4	31.2	25.8
5	100	100	0
6	12.6	24.5	11.9
7	6.2	18.3	12.1
8	6.0	22.8	16.8
9	10.4	21.1	10.7
10	2.5	5.7	3.2

2.3 Robust Design Optimization

Parameters of an array, such as the cantilever length, width and thickness, spring constant and deflection angle of the cantilevers for a given force, footprint of the array and lateral pitch between two adjacent cantilever, must satisfy initial requirements for good operation. Thanks to SIMBAD a decision making tool for development design, which we introduced in [45], we perform various optimization analyzes for the design of AFM probe arrays:

1. Sensitivity analysis: selection of the subset of model design variables with the greatest impact on system performance

2. Deterministic design optimization: searching the design space for solutions which optimize system behavior while satisfying design constraints

3. Uncertainty quantification: quantifying the impact of manufacturing uncertainties on the optimized system performance.

In this section, we introduce these tools through a static design optimization application for a one-dimensional array of cantilevers which is a collaboration with CSEM. Two dimensional arrays with unconnected rows are made by aligning several one-dimensional arrays. A parameter can be used to define the geometry of the array of levers and it may be a:

- fixed variable: a variable that its value is fixed (assessed value)

- free variable: a variable that can be freely chosen between two limits, or from a known list of values
- dependent variable: a variable that is depended to another free variable
- variable to be optimized: a variable that we seek to define the nearest possible to a target value which is included into two limitations
- variable to be minimized: a variable has to be minimized, which has a maximum threshold
- variable to be maximized: a variable has to be maximized, which has a minimum threshold

A constraint limits the choice of parameter values. It can be a:

- variable to be optimized: a variable that we seek to define the nearest possible to a target value which is included into two limitations
- variable to be minimized: a variable has to be minimized, which has a maximum threshold
- variable to be maximized: a variable has to be maximized, which has a minimum threshold
- threshold: a variable depends on other values or variables, which should not exceed a critical threshold, but what we seek is neither to be optimized nor to be minimized and nor to be maximized.

After definition of the boundary conditions, such as minimal and maximal values of the parameters to be optimized and material properties, SIMBAD computes the optimal design of the probe arrays.

2.3.1 Design Problem

We consider an one-dimensional array of cantilevers, (see Figure 2.16). It is comprised of bases crossing the array in which cantilever are clamped. The support is clamped on its external boundary. Cantilevers may be equipped with a rigid tip, as in AFMs, (see Figure 2.17). The whole array can be viewed as a periodic repetition of a same cell, referred as reference cell shown in Figure 2.18, in the two directions or in one direction. We suppose that the number of cells in each direction is sufficiently large, namely larger or equal to 10.

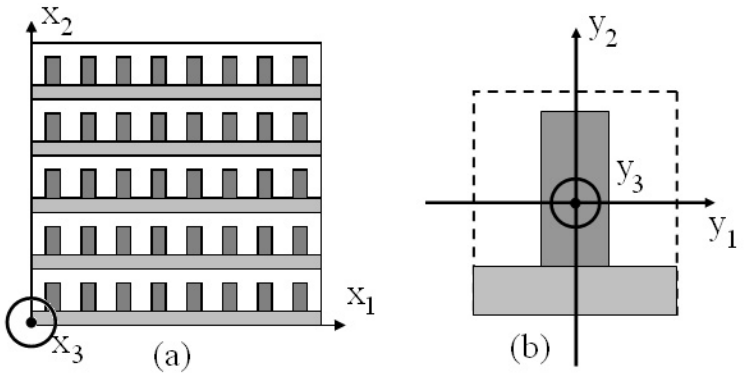

Figure 2.16: A one-dimensional view of (a) an Array and (b) a Cell

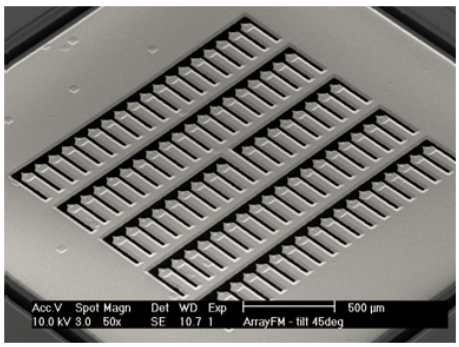

Figure 2.17: One-dimensional arrays of AFM. Courtesy of André Meister and of Thomas Overstolz, CSEM Neuchâtel Switzerland.

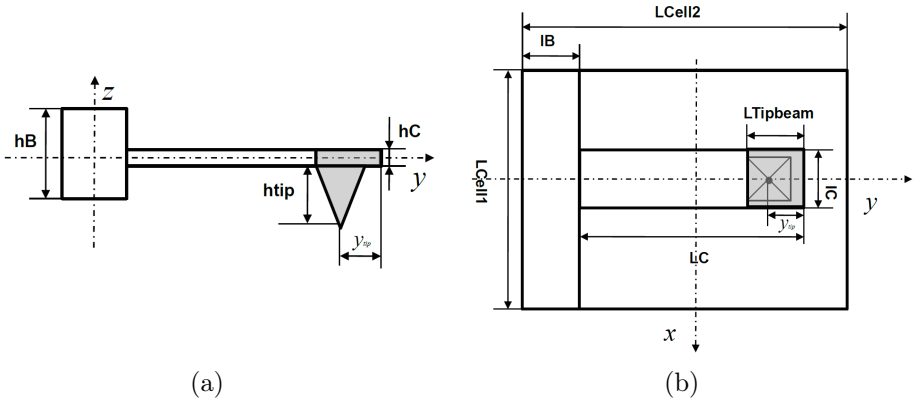

Figure 2.18: (a) Side view and (b) Top view of a reference cell

Design Variables

The design variable space is, $X = [x_1, x_2, \cdots, x_d] \in \mathbb{R}$. We list the design variables for this application in Table 2.6.

Table 2.6: List of design parameters

Label	X	Description	Initial value	Bound	Uncertainty
LC	x_1	Lever length	200 μm	[60 400] μm	$\pm$4 μm
lC	x_2	Lever width	40 μm	[40 80] μm	$\pm$1 μm
hC	x_3	Lever thickness	0.5 μm	[0.25 0.70] μm	$\pm$2%
EC	x_4	Young modulus of lever	335 Gpa	fixed	$\pm$10%
rhoC	x_5	Mass density of lever	3100 kg/m^3	fixed	$\pm$3%
activtip	x_6	Tip presence	1 (or 0)	fixed	
hB	x_7	Base thickness	30 μm	[30 60] μm	$\pm$10 μm
lB	x_8	Base width	40 μm	[10 200] μm	$\pm$1 μm
EB	x_9	Young modulus of Base	169 Gpa	fixed	$\pm$10%
rhoB	x_{10}	Mass density of Base	2330 kg/m^3	fixed	$\pm$3%
L1	x_{11}	Array size in x-direction	1000 μm	fixed	
nx	x_{12}	No. levers in x-direction	10	[2 20]	
ny	x_{13}	No. levers in y-direction	1	fixed	
ltip	x_{14}	Tip beam width	$x_2 - 10$ μm	dependent	$\pm$1 μm
ytip	x_{15}	position of tip apex	$x_2/2$	dependent	$\pm$4 μm
S_{array}	x_{16}	Array size	1×1 mm^2	fixed	
Dim	x_{17}	Array dimension	1 (or 2)	fixed	
LB	x_{18}	x-direction pitch	$floor(\frac{x_{11}}{x12 \times 50}) \times 50$ μm	proportional to 50 μm	
Lcell2	x_{19}	y-direction pitch	$(floor(\frac{x_1+x_8}{5 \times 10^{-5}}) + 1) \times 50$ μm	proportional to 50 μm	

Design Features

The design feature space is,

$$S = [s_1, s_2, \cdots, s_{n_s}] \in \mathbb{R}.$$

For a static design problem of AFM arrays, we list the design response features in Table 2.7.

Table 2.7: Design features

Label	S	**Description**	**Equation**
S_Spring	s_1	Spring constant of lever	$\frac{x_4 x_2 x_3^3}{4x_1^3}$
S_Tapex[1]	s_2	Static displacement at the tip apex	solved by AFMALab
S_Base	s_3	Static displacement at the base	solved by AFMALab
Gap	s_4	Gap between two levers	$x_{18} - x_2$
Gapcell	s_5	Gap percentage of each cell	$1 - \frac{x_1 x_2 + x_{18} x_8}{x_{18} x_{19}}$
S_MTn	s_6	Mechanical–thermal noise	not used
S_FP	s_7	Footprint size	$x_{11}(x_1 + x_8)$
S_hB	s_8	Base thickness	x_7

[1] maximum deflection at tip when the lever is bent by a known static point force in the x_3-direction $F_{\max}$.

Design Objectives

The design objective functions are defined as

$$F_i(x), \text{ with } i = 1, \cdots, n_F$$

which depend on the design variables. An aggregated mono-objective minimization with nonlinear constraints standard form is considered to solve the optimization problem,

$$\min_x (\sum_{i=1}^{n_F} \omega_i F_i(x))$$

where ω_i is the weight for ith design objective. The standard form of design objectives are presented in Table 2.8.

Table 2.8: Design objectives

Label	$F(x)$	**Description**	Equation
F_Gap	$F_1(x)$	Gap between two levers	s_4
F_Gapcell	$F_2(x)$	Gap percentage of each cell	s_5
F_hB	$F_3(x)$	Base thickness	s_8

Nonlinear Design Constraints

We have certain number of nonlinear constraints, transformed into standard form, presented in Table 2.9.

Table 2.9: Nonlinear design constraints

Label	Description	Equation	Tolerance
C_Base	Maximum displacement at base must smaller than 50 nm for small array and 80 nm for large array	$s_3 - 50$ nm≤ 0 or $s_3 - 80$ nm≤ 0	
C_Gap	Minimum gap between two levers larger than $lC/2$	$\frac{x_2}{2} - s_4 \leq 0$	± 1 μm
C_Gapcell	Minimum gap percentage of each cell greater than 40%	$0.4 - s_5 \leq 0$	
C_Angle	Maximum deflection angle at tip end less than $\frac{3\pi}{180}$	$\arctan(\frac{3S_2}{2(x_1-x_2/2)}) - \frac{3\pi}{180} \leq 0$	
C_Spring	Spring constant equals to 0.03 with $F_{max} = 2$ nN	$s_1 - 0.03 = 0$	$\pm 50\%$
C_FP	Maximum footprint size of	$s_7 - 1 \times 1$ mm$^2 \leq 0$	
	small and large array	or $s_7 - 2 \times 2$ mm$^2 \leq 0$	

2.3.2 Phases of the Design Optimization Process

Design Sensitivity and Effects Analysis

- First-order sensitivity analysis

  We perform a first-order sensitivity analysis to select the most influential design variables by a steepest descent algorithm. The result of the first-order sensitivity analysis plot is shown in Figure 2.19.

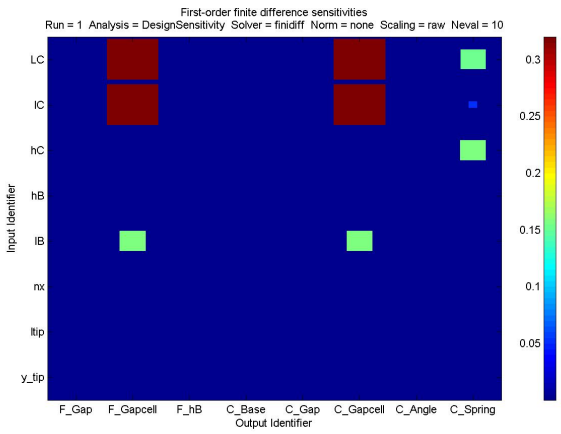

Figure 2.19: First-order finite difference sensitivities

The analysis result shows that the length and width of cantilever arrays are most critical parameters.

- Parametric analysis

We perform a parametric analysis to see the relationships between design variables. A parametric analysis of AFM array is represented in Figure 2.20.

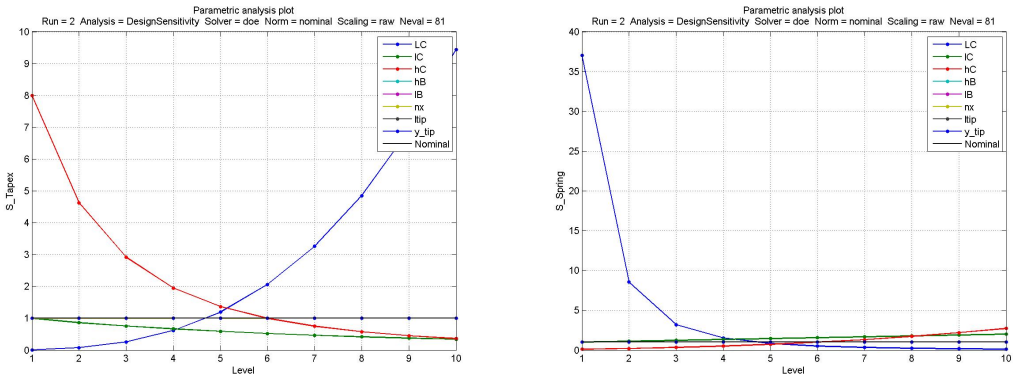

(a) (b)

Figure 2.20: Parametric analysis of active design parameters and features (a) S_Tapex (b) S_Spring

- Monte-Carlo analysis

Monte-Carlo analysis generates random points in the design space consistent with the uncertainty distributions for the different design parameters (eg. Gaussian, uniform, etc). Stratified random search algorithms such as Latin Hypercube Sampling can also be used to guarantee a better coverage of the design space of a given number of evaluations. These methods can be used in view of either a global sensitivity analysis or for the quantification of uncertainty. We perform a Monte-Carlo analysis to see the changes of design variables. Plot the results of the Monte-Carlo analysis. Scatter plots with Monte-Carlo sampling are shown in Figure 2.21.

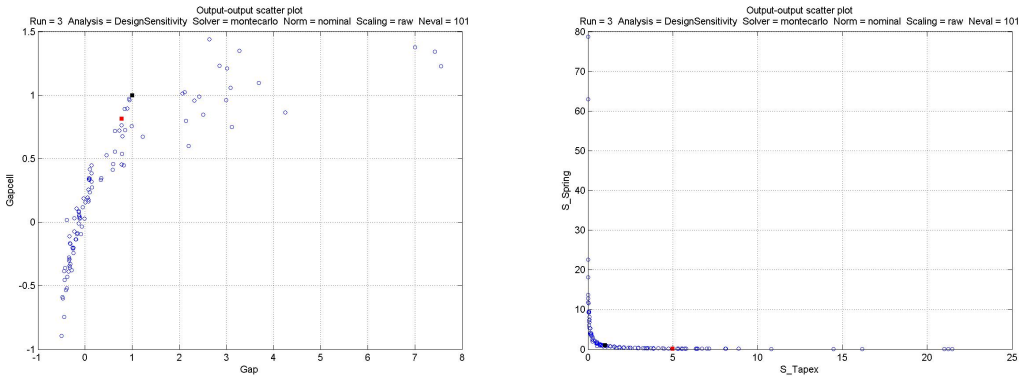

(a) (b)

Figure 2.21: Scatter plots of Monte Carlo sampling

- Principal component analysis

  Principal component analysis (PCA) is a way of identifying patterns in data, and expressing the data in such a way as to highlight their similarities and differences. Since patterns in data can be hard to find in data of high dimension, where the luxury of graphical representation is not available, PCA is a powerful tool for analyzing data. We perform a Principal component analysis to find the patterns of design variables. A principal component analysis based on Monte Carlo sampling is shown in Figure 2.22.

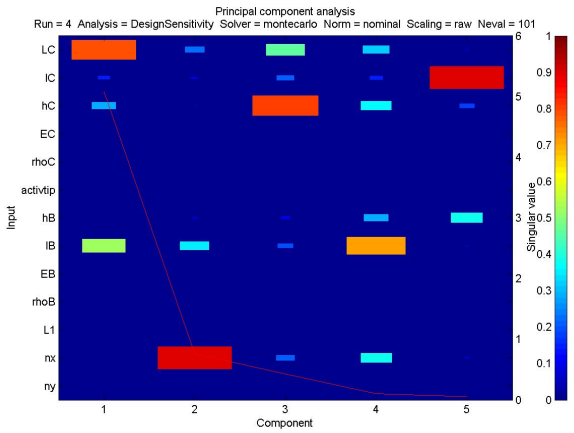

Figure 2.22: Principal component analysis

Design Optimization

An optimal design is the best feasible design according to a preselected quantitative measure of effectiveness. In current application, aggregated mono-objective optimization with design constraints and multi-objective optimization with design constraints problems are written in standard forms.

- Aggregated Mono-objective optimization with design constraints

  The mono-objective optimization is the standard optimization problem, see [46] for an introduction. Given the function F that depends on the design variables $x = [x_1, x_2, \cdots, x_d] \in \mathbb{R}$, the optimization problem is to find:

$$\min_{x \in X} \left(\sum_{i=1}^{n_F} \omega_i F_i(x) \right)$$

  subject to the constraints:

$$\begin{aligned} x &\in X \\ g_j(x) &\leq 0, \ j = 1, \cdots, n_g \\ h_k(x) &= 0, \ k = 1, \cdots, n_h \end{aligned}$$

  where ω_i are weighting coefficients taking into account the relative importance of each objective. We perform a mono-objective optimization analysis to find the best solution of the designs. The results of a mono-objective optimization with nonlinear constraints are shown in Figure 2.23. The results

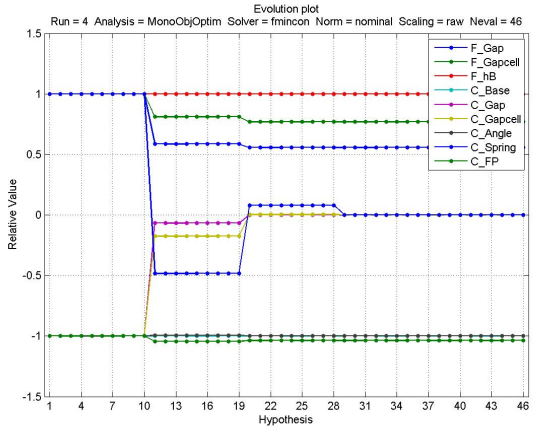

Figure 2.23: Evolution plot by solving mono-objective optimization problem

  indicate that some of the objectives, for instance F_Gap and $F\_Gapcell$, are decreased when all the nonlinear constrains are satisfied.

- Multi-objective optimization with design constraints

  Multi-objective optimization, also known as multi-criteria or multi-attribute optimization, is the process of simultaneously optimizing two or more conflicting objectives subject to certain constraints. Given the function $f_i(x)$ that depends on the design variables $x \in X = [x_1, x_2, \cdots, x_d] \in R^d$, the optimization problem is to find:

$$\min_x \{f_1(x), \cdots, f_{n_f}(x)\}$$

  subject to:

$$\begin{aligned} x_L &\leq x \leq x_U \\ g_j(x) &\leq 0,\ j = 1, \cdots, n_g \\ h_k(x) &= 0,\ k = 1, \cdots, n_h \end{aligned}$$

  The solution to the above problem is a set of Pareto points. We perform a multi-objective optimization analysis to find the best solution of the designs. The results of a multi-objective optimization with nonlinear constraints are shown in Figure 2.24.

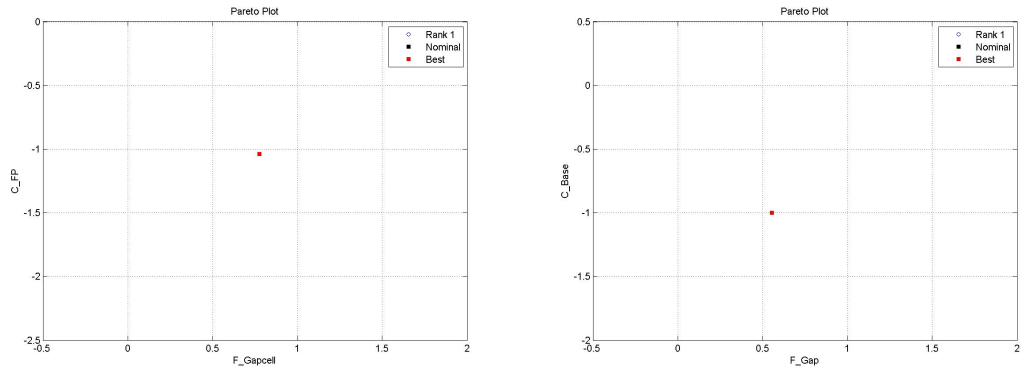

(a) (b)

Figure 2.24: Pareto plot of Monte Carlo sampling between (a) F_Gapcell and C_FP and (b) F_Gap and C_base

Uncertainty Quantification

Uncertainty quantification (UQ) is the science of quantitative characterization and reduction of uncertainties in applications. It tries to determine how likely certain

outcomes are if some aspects of the system are not exactly known. We perform an uncertainty quantification analysis with Monte-Carlo samples. The results of an uncertainty qualification analysis with uniform probability density function (PDF) are represented in Figure 2.25.

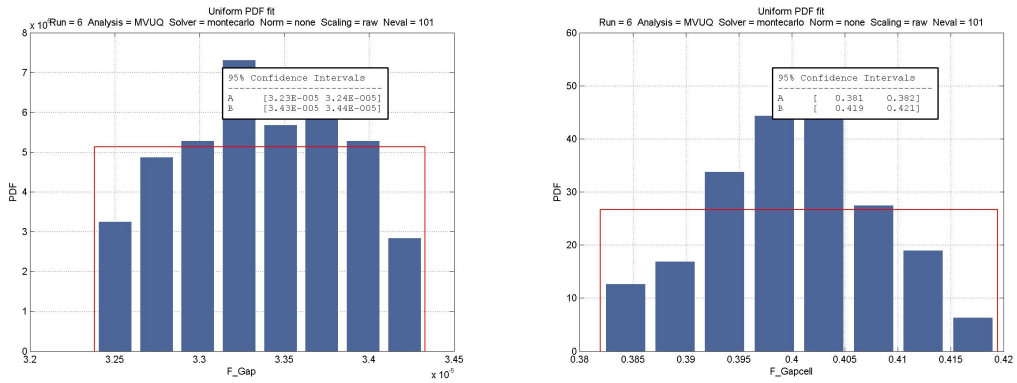

(a) (b)

Figure 2.25: Uncertainty qualification analysis

Application of Robust Design Optimization for Arrays of AFMs

In this application, we consider designing six types of array of AFMs on a single wafer. The six types of arrays correspond to three different cantilever spring constants, and to two different cantilever pitch conditions. For some applications, the pitch between cantilevers cannot be freely chosen. The three spring constants correspond to 0.03, 0.3 and 3 N/m, and the two pitch conditions define the lateral and longitudinal cantilever pitches as a multiple of $10\mu m$, respectively $100\mu m$. Table 2.10 summarizes the results of the optimization computation.

Table 2.10: Designs of probe arrays defined using the design decision making tool SIMBAD. The values in italic correspond to the initial conditions, and the values in bold to the optimized design parameters.

Array design	1	2	3	4	5	6
Pitch condition $[\mu m]$	*10*	*10*	*10*	*100*	*100*	*100*
Spring constant $[N/m]$	*0.03*	*0.3*	*3*	*0.03*	*0.3*	*3*
No. lever in x-direction	*16*	*16*	*11*	*10*	*10*	*10*
No. lever in y-direction	*2*	*4*	*5*	*2*	*3*	*5*
Pitch in x-direction $[\mu m]$	**60**	**60**	**90**	**100**	**100**	**100**
Pitch in y-direction $[\mu m]$	**500**	**250**	**200**	**500**	**300**	**200**
Length of cantilever $[\mu m]$	**300**	**150**	**100**	**300**	**150**	**100**
With of cantilever $[\mu m]$	**40**	**40**	**56**	**40**	**40**	**56**
Optimized spring constant	**0.033**	**0.33**	**2.7**	**0.033**	**0.33**	**2.7**

A microfabrication run to produce cantilever arrays with the optimized design was launched. An example of a computed optimized design and of a produced cantilever array are shown in Figure 2.26.

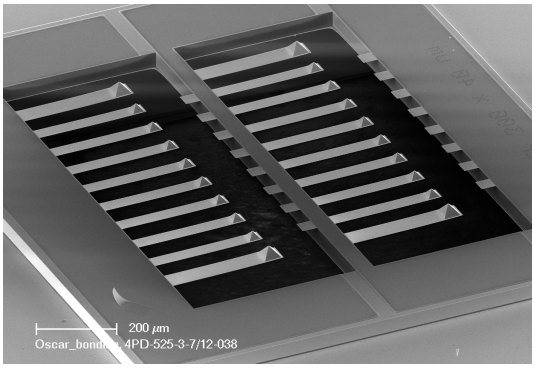

Figure 2.26: Example of an optimized design geometry. The larger cantilevers with larger and higher tip situated in the corner of the probe array are used to land and adjust the probe array onto the sample surface. Courtesy of André Meister and Thomas Overstolz, CSEM Neuchâtel Switzerland.

Normally, the optimal design is not unique. A compromise between the design objectives should be made with the consideration of meeting the requirements for microfabrication.

2.4 Conclusion

In this chapter, we have carried out the model verification by comparing the eigenvalue density distribution and eigenmodes to a direct FEM simulations. The verifi-

cations for an array of cantilevers, without tips both in static and dynamic regimes, have been reported. The results shown a globally good agreement with the three-dimensional elasticity model. We have also reported results of design optimization for an array of AFMs. It opens the way for future works on model calibration, other design problems, such as for dynamical problem, and for control synthesis.

In the next chapter, we shall present a global phase computation algorithm of interferometry measurement of cantilever displacements in quasi-static regime, which is an improvement to an algorithm introduced in [47].

Chapter 3

INTERFEROMETRY MEASUREMENT FOR AFM ARRAYS

Contents

In this chapter we focus on a method based on interferometry for cantilever displacement measurement in quasi-static regime. Cantilevers are illuminated by an optical source. Interferometry produces fringes enabling cantilever displacement measurement. A high speed camera is used to analyze the fringes. In view of real time applications, images need to be processed quickly and then a fast estimation method is required to determine the displacement of cantilevers. In [43], an algorithm based on splines has been introduced for cantilever position estimation. The overall process gives accurate results where computations are performed on a standard computer using LabView®. Consequently, the main drawback of this implementation is that bandwidth offered by the computer is a limitation. In paper [47], authors have proposed a new algorithm based on the least square method which achieves the better precision with less operations than the algorithm based on a spline method. However, this algorithm is limited since it assumes that the cantilevers are uncoupled. Here we relax this assumption in a global computation

of the phases based on our two-scale model presented in section 1.3. A topographic scan application for an array of AFMs in quasi-static regime is reported.

3.1 Measurement of Displacement in a Cantilever Array

In this section, we detail our global phase computation algorithm of interferometry measurement for array of AFMs in quasi-static regime. Section 3.1.1 describes the experimental set-up at CSEM, and Section 3.1.2 presents the global phase computation algorithm.

3.1.1 The Experimental Set-up

An illustrative picture of the experimental set-up [43], developed by CSEM, is shown in Figure 3.1.

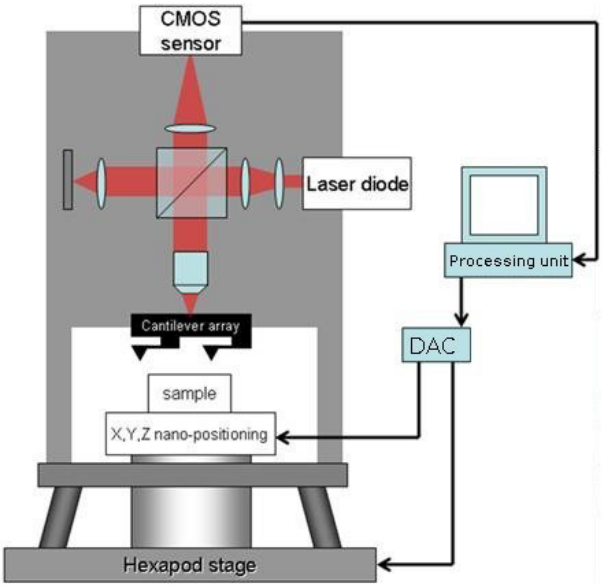

Figure 3.1: AFM experimental setup

In contrast to other optical based systems using a laser beam deflection scheme, which is sensitive to the angular displacement of the cantilever, interferometry is sensitive to the optical path difference induced by the vertical displacement of the cantilever. The interferometric system is based on a Linnik interferometer [48]. A laser diode is first split into a reference beam and a sample beam both reaching the

cantilever array. The complete system including a cantilever array and the optical system can be moved thanks to a translation and rotational hexapod stage with six degrees of freedom. Thus, the cantilever array is centered in the optical system which can be adjusted accurately. The beam illuminates the array by a microscope objective and the light reflects on the cantilevers. Likewise the reference beam reflects on a movable mirror. A CMOS camera chip records the reference and sample beams which are recombined in the beam splitter and the interferogram. Then, cantilever motion in the transverse direction produces movements in the fringes. They are detected with the CMOS camera where images are analyzed by a LabView® program to recover the cantilever deflections.

3.1.2 Cantilever Displacement Estimation

We consider an array made with uncoupled rows of AFM cantilevers, see Figure 3.2.

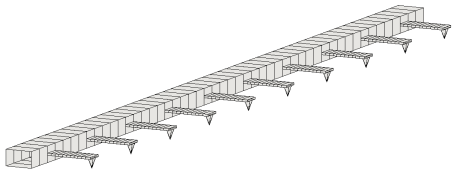

Figure 3.2: A one-dimensional view of array of AFMs.

In [43], as shown in Figure 3.3, the cantilever is covered by interferometric fringes. They distort when cantilevers deflect. For each cantilever, the displacement is derived from phase shift of the light intensity. A phase shift corresponds to the lateral shift of the intensity profile along a segment of pixels induced by the cantilever bending. Three segments of pixels, parallel to its width, are used. The first one is located just above the AFM tip (tip profile), it provides the phase shift modulo 2π. The second one is close to the base junction (base profile) and is used to determine the exact multiple of 2π through an operation called unwrapping where it is assumed that the displacements along the two measurement segments are linearly dependent. The third one is on the base (reference profile) and provides a reference for cancelling the effect of base motion.

Each profile is expressed in a normalized interval $(0, M-1)$ where M is the number of pixels of the profile. The gray-level light intensity is under the form

$$I(x_p) = ax_p + bA\cos(2\pi f x_p + \theta). \tag{3.1}$$

where $x_p \in (0, M-1)$, f and θ are the frequency and the phase of the interferometric signal, and the affine function $ax_p + b$ corresponds to cantilever surface

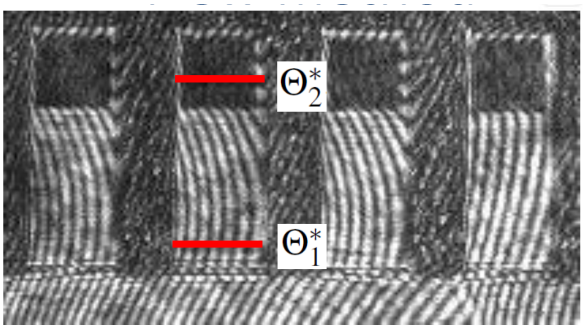

Figure 3.3: Intensity profiles: close to base-cantilever junction Θ_1^* and above the tip of cantilevers Θ_2^*.

tilt with respect to the light source. The phase computation is done either using a spline method or a least square method detailed in [47]. For a given phase θ, we denote by $\theta^* \in [0, 2\pi)$ its value modulo 2π i.e.

$$\theta = \theta^* + 2n\pi \text{ and } n = [\frac{\theta}{2\pi}], \tag{3.2}$$

where $[\alpha]$ represents the integer part of α. The relation between the phase and the displacement is

$$\theta = 2\pi f \overline{c}(\overline{b} - 2u) \tag{3.3}$$

where $\overline{b}$, $\overline{c}$ are constants related to the tilt of the beam splitter and are determined in a calibration phase. Moreover, the constant $\overline{b}$ corresponds to a constant phase shift that is ignored in the following, so we use only the proportionality relation

$$\theta = -mu. \tag{3.4}$$

As u is decomposed into $\overline{u} + \widetilde{u}$, the phase θ is also decomposed as $\theta = \overline{\theta} + \widetilde{\theta}$. The base and tip profiles are taken at positions $y_2 = y_{2,1}$ and $y_{2,2}$ and all corresponding notations are indexed by 1 and 2, as for instance θ_1 and θ_2. In the setup [43], the reference profile is used to determine $\overline{\theta}$. The displacements of the base are assumed to be sufficiently small so that $\overline{\theta}^* = \overline{\theta}$. The base profile is sufficiently close from the base so that $\theta_1 = \theta_1^*$ also. And, the linear relation between $\widetilde{u}_1$ and $\widetilde{u}_2$, or $\widetilde{\theta}_1$ and $\widetilde{\theta}_2$, is used to determine the integer n_2. In total, $\overline{u}$, $\widetilde{u}_1$ and $\widetilde{u}_2$ are determine from three measurements and the tip force can be deduced.

In the following, we introduce an alternate method to avoid the reference measurement, based on the two-scale model.

For an array of N cantilevers, we refer the i^{th} cantilever with the subscript $i \in \{1, ..., N\}$, and we use the relation (3.4) applied to each of them,

$$\begin{cases} \theta_{1,i} = \theta^*_{1,i} = -m(\bar{u}_i + \tilde{u}_{1,i}), \\ \theta_{2,i} = -m(\bar{u}_i + \tilde{u}_{2,i}). \end{cases}$$

The above equation written in vector form is

$$\begin{cases} \Theta_1 = \Theta^*_1 = -m(\bar{U} + \tilde{U}_1), \\ \Theta_2 = -m(\bar{U} + \tilde{U}_2). \end{cases} \tag{3.5}$$

The two-scale model is discretized, and the N-dimensional vectors $\bar{U}$, $\tilde{U}_1$ and $\tilde{U}_2$ represent the displacements in the base and in cantilevers at $y_2 = y_{2,1}$ and $y_{2,2}$ respectively at the coordinates x_1 of the cantilever centers. Neglecting all external forces excepted the tip forces $f^{tip} = (f^{tip}_i)_{i=1,..,N}$ and considering the system in the quasi-static regime, there exists three $N \times N$ stiffness matrices $\bar{K}$, $\tilde{K}_1$ and $\tilde{K}_2$ such that

$$\bar{U} = [\bar{K}]^{-1} f^{tip},\ \tilde{K}_1\tilde{U}_1 = f^{tip} \text{ and } \tilde{K}_2\tilde{U}_2 = f^{tip}. \tag{3.6}$$

Eliminating f^{tip} in the two last relations using the first one,

$$\begin{cases} \bar{U} = [\bar{K}]^{-1}\tilde{K}_1\tilde{U}_1, \\ \tilde{U}_2 = [\tilde{K}_2]^{-1}\tilde{K}_1\tilde{U}_1. \end{cases} \tag{3.7}$$

By (3.5) and (3.7), we derive the relation between the phases of two profile lines,

$$\Theta_2 = K\Theta_1 \tag{3.8}$$

where the matrix $K = ([\bar{K}]^{-1} + [\tilde{K}_2]^{-1})\tilde{K}_1([\bar{K}]^{-1}\tilde{K}_1 + Id)^{-1}$ and Id being the identity matrix. Using this relation and the fact that $\Theta_1 = \Theta^*_1$ we deduce n_2 in the phase decomposition (3.2) and Θ_2,

$$n_2 = [\frac{K\Theta^*_1}{2\pi}] \text{ and } \Theta_2 = \Theta^*_2 + 2n_2\pi. \tag{3.9}$$

Thus, combining the relations (3.5), (3.6) and (3.9) we can establish that

$$\Theta^*_1 = D_1 f^{tip} \text{ or } \Theta^*_2 + 2n_2\pi = D_2 f^{tip}$$

with $D_1 = -m([\bar{K}]^{-1} + [\tilde{K}_1]^{-1})$ and $D_2 = -m([\bar{K}]^{-1} + [\tilde{K}_2]^{-1})$. In conclusion, we estimate the tip forces from (3.6) and we deduce $\bar{U}$ the base displacement and U_2 the total tip displacement, all being expressed with the measurements Θ^*_1 and Θ^*_2,

$$f^{tip} = D_1^{-1}\Theta^*_1 \text{ or } f^{tip} = D_2^{-1}(\Theta^*_2 + 2n_2\pi), \tag{3.10}$$

$$\bar{U} = [\bar{K}]^{-1} f^{tip},\ U_2 = -\frac{1}{m}(\Theta^*_2 + 2n_2\pi) \text{ with (3.9)}. \tag{3.11}$$

Algorithm 1: Phase correction algorithm.

1 $\Theta_1 \leftarrow$ phase of the base profile
2 $\Theta_2 \leftarrow$ First tip-profile phase estimated by (3.9)
3 $\Theta_2' \leftarrow$ Second tip-profile phase estimated by (3.8)
4 $\delta\Theta_2 = \Theta_2' - \Theta_2$
5 $\Theta_2 = \Theta_2 + 2\pi * round(\frac{\Theta_2}{2\pi})$

In practice, the formula (3.9) may produce inaccurate phase of tip profile by a perturbation of 2π. The source of the error comes from the integer part calculation due to its discontinuity. We state Algorithm 1 that eliminates the error, where ε is in the range of the error.

Remark 3 *The scanner operates with a sufficient small step, so that we can locate the positions where the integer calculation generates inaccurate phases through algorithm (1). Then, these positions are saved in the memory for real-time control applications.*

3.2 Least Square Algorithm (LSQ) for Phase Computation

For the sake of simplicity of the notations, we consider the light intensity I a function on the interval $[0, M-1]$ which itself is the range of a one-to-one mapping defined on the physical segment. The pixels are assumed to be regularly spaced and centered at the positions $x_p \in \{0, 1, \ldots, M-1\}$. We use the simplest definition of a pixel, namely the value of I at its center. The pixel intensities are considered as pre-normalized so that their minimum and maximum have been resized to -1 and 1,.

We compute the phase during the acquisition loop, equation (3.1) has only 4 parameters: a, b, A, and θ, f and x_p being already known. A least square method based on a Gauss-Newton algorithm can be used to determine these four parameters. This kind of iterative process ends with a convergence criterion, so it is not suited to our design goals. Fortunately, it is quite simple to reduce the number of parameters to θ only. Firstly, the affine part $ax_p + b$ is estimated from the M values $I(x_p)$ to determine the rectified intensities,

$$I^{corr}(x_p) \approx I(x_p) - ax_p - b.$$

To find a and b we apply an ordinary least square method

$$a = \frac{\text{covar}(x_p, I(x_p))}{\text{var}(x_p)} \quad \text{and} \quad b = \overline{I(x_p)} - a.\overline{x_p}$$

where overline symbols represent average. Then the amplitude A is approximated by

$$A \approx \frac{\max(I^{corr}) - \min(I^{corr})}{2}.$$

Finally, the problem of approximating θ is reduced to minimizing

$$\min_{\theta \in [-\pi,\pi]} \sum_{i=0}^{M-1} \left[\cos(2\pi f.i + \theta) - \frac{I^{corr}(i)}{A} \right]^2,$$

which will allow to determine an angle $\theta^*(t, x_2^0) \in (-\pi, \pi)$. Note that the solution of minimizing this problem is not unique.

An optimal value θ^* of the minimization problem is a zero of the first derivative of the above argument,

$$\begin{aligned} 2 \left[\cos\theta^* \sum_{i=0}^{M-1} I^{corr}(i).\sin(2\pi f.i) + \sin\theta^* \sum_{i=0}^{M-1} I^{corr}(i).\cos(2\pi f.i) \right] \\ -A \left[\cos 2\theta^* \sum_{i=0}^{M-1} \sin(4\pi f.i) + \sin 2\theta^* \sum_{i=0}^{M-1} \cos(4\pi f.i) \right] = 0 \end{aligned}$$

Several points can be noticed:

- The terms $\sum_{i=0}^{M-1} \sin(4\pi f.i)$ and $\sum_{i=0}^{M-1} \cos(4\pi f.i)$ are independent of θ, they can be precomputed.
- Lookup tables (namely lut_{sfi} and lut_{cfi} in the following algorithms) can be set with the $2.M$ values $\sin(2\pi f.i)$ and $\cos(2\pi f.i)$.
- A simple method to find a zero θ^* of the optimality condition is to discretize the range $[-\pi, \pi]$ with a large number nb_s of nodes and to find which one is a minimizer in the absolute value sense. Hence, three other lookup tables (lut_s, lut_c and lut_A) can be set with the $3 \times nb_s$ values $\sin\theta$, $\cos\theta$, and

$$\left[cos2\theta \sum_{i=0}^{M-1} sin(4\pi f.i) + sin2\theta \sum_{i=0}^{M-1} cos(4\pi f.i) \right].$$

- The search algorithm can be very fast using a dichotomous process in $log_2(nb_s)$.

The overall method is synthesized in an algorithm (called LSQ in the following) divided into the precomputing part and the acquisition loop, see [47].

Algorithm 2: LSQ algorithm - before acquisition loop.

$M \leftarrow$ number of pixels of the profile
I[] $\leftarrow$ intensity of pixels
$f \leftarrow$ frequency of the profile
$s4i \leftarrow \sum_{i=0}^{M-1} sin(4\pi f.i)$
$c4i \leftarrow \sum_{i=0}^{M-1} cos(4\pi f.i)$
$nb_s \leftarrow$ number of discretization steps of $[-\pi, \pi]$
for $i = 0$ *to* nb_s **do**
    $\theta \leftarrow -\pi + 2\pi \times \frac{i}{nb_s}$
    $\text{lut}_s[i] \leftarrow sin\theta$
    $\text{lut}_c[i] \leftarrow cos\theta$
    $\text{lut}_A[i] \leftarrow cos2\theta \times s4i + sin2\theta \times c4i$
    $\text{lut}_{sfi}[i] \leftarrow sin(2\pi f.i)$
    $\text{lut}_{cfi}[i] \leftarrow cos(2\pi f.i)$
end

Algorithm 3: LSQ algorithm - during acquisition loop.

$\bar{x} \leftarrow \frac{M-1}{2}$
$\bar{y} \leftarrow 0$, $x_{var} \leftarrow 0$, $xy_{covar} \leftarrow 0$
for $i = 0$ *to* $M-1$ **do**
  $\bar{y} \leftarrow \bar{y}+ \mathrm{I}[i]$
  $x_{var} \leftarrow x_{var} + (i - \bar{x})^2$
end
$\bar{y} \leftarrow \frac{\bar{y}}{M}$
for $i = 0$ *to* $M-1$ **do**
  $xy_{covar} \leftarrow xy_{covar} + (i - \bar{x}) \times (I[i] - \bar{y})$
end
$slope \leftarrow \frac{xy_{covar}}{x_{var}}$
$start \leftarrow \bar{y} - slope \times \bar{x}$
for $i = 0$ *to* $M-1$ **do**
  $I[i] \leftarrow I[i] - start - slope \times i$
end
$I_{max} \leftarrow max_i(I[i])$, $I_{min} \leftarrow min_i(I[i])$
$amp \leftarrow \frac{I_{max}-I_{min}}{2}$
$Is \leftarrow 0$, $Ic \leftarrow 0$
for $i = 0$ *to* $M-1$ **do**
  $Is \leftarrow Is + I[i] \times \mathrm{lut}_{sfi}[i]$
  $Ic \leftarrow Ic + I[i] \times \mathrm{lut}_{cfi}[i]$
end
$\delta \leftarrow \frac{nb_s}{2}$, $b_l \leftarrow 0$, $b_r \leftarrow \delta$
$v_l \leftarrow -2.I_s - amp.\mathrm{lut}_A[b_l]$
while $\delta >= 1$ **do**
  $v_r \leftarrow 2.[Is.\mathrm{lut}_c[b_r] + Ic.\mathrm{lut}_s[b_r]] - amp.\mathrm{lut}_A[b_r]$
  if $!(v_l < 0 \ and \ v_r >= 0)$ **then**
    $v_l \leftarrow v_r$
    $b_l \leftarrow b_r$
  end
  $\delta \leftarrow \frac{\delta}{2}$
  $b_r \leftarrow b_l + \delta$
end
if $!(v_l < 0 \ and \ v_r >= 0)$ **then**
  $v_l \leftarrow v_r$
  $b_l \leftarrow b_r$
  $b_r \leftarrow b_l + 1$
  $v_r \leftarrow 2.[Is.\mathrm{lut}_c[b_r] + Ic.\mathrm{lut}_s[b_r]] - amp.\mathrm{lut}_A[b_r]$
else
  $b_r \leftarrow b_l + 1$
end
if $abs(v_l) < v_r$ **then**
  $b_\theta \leftarrow b_l$
else
  $b_\theta \leftarrow b_r$
end
$\theta \leftarrow \pi \times \left[\frac{2.b_{ref}}{nb_s} - 1\right]$

3.3 Application: Topographic Scan

We illustrate the algorithm by a sample surface topographic scan simulation for an array of AFMs in quasi-static regime. We consider an 10-cantilevers array with base dimensions $L_B \times \ell_B \times h_B = 500\mu m \times 16.7\mu m \times 10\mu m$, and those of cantilevers $L_C \times \ell_C \times h_C = 25\mu m \times 10\mu m \times 1.25\mu m$. The other model parameters are the bending coefficient $R^B = 1.09 \times 10^{-5} N/m$, $R^C = 2.13 \times 10^{-4} N/m$ and the masses per unit length $m^B = 0.0233 kg/m$, $m^C = 0.00291 kg/m$, and the light wavelength is $\lambda = 0.633\mu m$. The number of pixels in all measurement segments is taken as 20. The position of the base profile line is defined as $y_{2,1} = \frac{L_C^0}{10}$. The topography of the samples is defined with bumps that are regularly distributed both in x_1- and y_2-directions, see Figure 3.4.

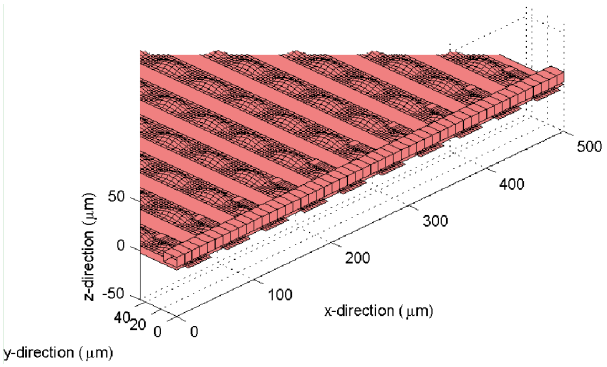

Figure 3.4: AFM arrays and samples.

The scan procedure is following:

1. The AFM arrays is a low position to put tips in contact with the sample surface.
2. The scanner moves in the negative y_2-direction and the deflection at tips are measured by interferometry in each scan step.
3. At the end of the line, the scanner moves back to the initial y_2-position, then increase the x_1-position to the next line.
4. Repeat step 2 and 3 until the required number of lines is obtained.
5. Save data.

All these steps together with the method for estimation of cantilever deflection have been implemented in a simulation. The sample is an array of 10×10 bumps.

Their dimensions are $L_S \times \ell_S \times h_S = 10\mu m \times 20\mu m \times 0.1\mu m$. Twenty scan lines distant from $2\mu m$ are recorded in the x_1-direction with 128 scan points each distant from $1\mu m$. The estimated three-dimensional topography with Formula (3.9) is presented in Figure 3.5.

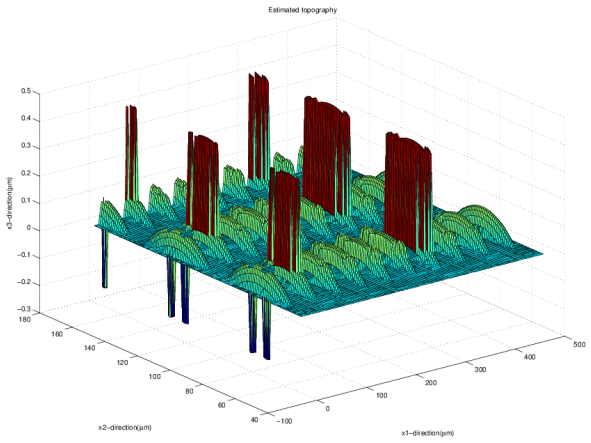

Figure 3.5: Estimated sample topography with Formula (3.9).

It shows peaks due to the integer part calculation in Formula (3.9). The use of Algorithm (1) eliminates them as seen in Figure 3.6.

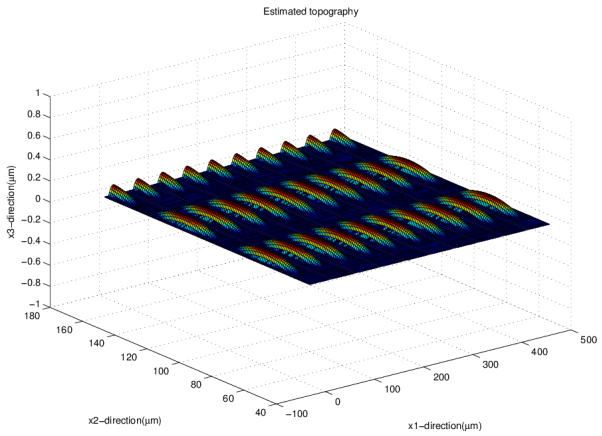

Figure 3.6: Estimated sample topography after phase correction.

Here, we also present the topographic scan results through the commercial software MountainsMap®. In this simulation, we use the same configuration of the AFM arrays and the topography of samples. One surface view in three-dimensional

is shown in Figure3.7 (a). A stitching technique is used to recover the topography of the sample, (see Figure 3.7 (b)).

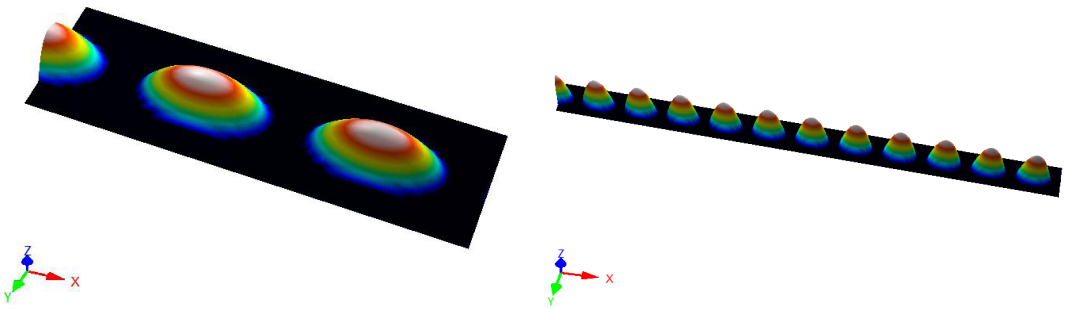

(a) (b)

Figure 3.7: (a) One surface viewed in three-dimensional (b) Stitched surface

3.4 Conclusion

In this paper, we have presented an effective global phase computation algorithm of interferometry for deflection measurement in an array of cantilevers in quasi-static regime. It improves a method using three measurements in each cantilever by avoiding one of them. It has been tested in a full simulation including a cantilever array, a scanner and an analyzed surface. Applications are also envisioned as for instance topographic scans for different samples and force spectroscopy.

In the next chapter, we shall present the semi-decentralized approximation method and its application to LQR control problem and H_∞ filtering problem for an array of cantilevers.

Chapter 4

SEMI-DECENTRALIZED APPROXIMATION METHOD AND ITS APPLICATIONS

Contents

In spite of significant development of large AFM arrays, the status of achieving their global distributed control is still at its preliminary stage. Due to the extremely huge data exchanges between distributed sensors and actuators, appropriate architectures of distributed processors allowing for highly parallel processing are wished. So, appropriate distributed control algorithms are required to operate on such architectures. Some groups have reported algorithms of semi-decentralized optimal control for systems with distributed actuators and sensors. In [34] and [35], the authors have considered the systems with infinite length, which are governed by partial differential equations. And the paper [36] has focused on discrete systems. A preliminary investigation of semi-decentralized control for partial differential equations in a bounded domain has been carried out for vibration control by M. Kader et al. and reported in [37] and [38]. It uses distributed piezoelectric

actuators and sensors, and implement a simple optimal control strategy, namely a Linear Quadratic Regulator (LQR), using a distributed analog electronic circuits. Other authors, [49], [50], [51], [52], have also worked on the same concept of distributed control realized by distributed circuits. The approach [37] has been significantly improved by [39], [40]. The polynomial approximation of a function of a self-adjoint operator was replaced by an approximation derived from the Cauchy integral formula. Here, we improve this method, apply it to control problems for cantilever arrays, and show how it can be implemented as Periodic Network of Resistors (PNR). The latter is a general method presented in [53], [54] for solving a large class of partial differential equations by analog computation. Two applications are studied, one to an LQR control problem published in [55], and one to an H_∞ filtering problem.

This chapter is organized as follows. In section 4.1, we focus on the derivation of the semi-decentralized approximation method and its applications to the LQR control problem for a one-dimensional AFM arrays. This is followed in section 4.2 by the application to an H_∞ filtering problem.

4.1 Semi-decentralized Approximation Method of an LQR Problem

We apply, with some improvements, the theory presented in [39], [40] on the reformulated two-scale model of one-dimensional micro-cantilever arrays introduced in section 1.3. The calculations are carried out using a simple Linear Quadratic Regulator (LQR) optimal control strategy, for the purpose of canceling vibrations. We study the quality of the approximation method, i.e. its precision and its cost. We also provide a realization of the semi-decentralized control scheme through PNR circuits.

4.1.1 Statement of the *LQR* Problem

By recalling the reformulated model in section 1.3,

$$\begin{cases} \rho^B \partial_{tt}^2 \overline{u} + R^B \partial_{x_1 \cdots x_1}^4 \overline{u} + \frac{\ell_C^0 r^C}{(L_C^0)^3} \sum\limits_k \widetilde{u}_k c_k = f^B \text{ in base,} \\ m^{C0} \partial_{tt}^2 \widetilde{u}_k + m^{C0} \partial_{tt}^2 \bar{u} \bar{\phi}_k + \frac{r^{C0} \lambda_k^C}{(L_C^0)^4} \widetilde{u}_k = f_k^C \text{ for each } k, \end{cases} \tag{4.1}$$

where $c_k = \partial^3_{\xi_2\xi_2\xi_2} \varphi_k(0)$ with $\xi_2 = \frac{y_2}{L_C^0}$. We can write the LQR problem in an abstract setting, see [56], even if we do not justify the functional framework. We set $z^T = \begin{pmatrix} \overline{u} & (\widetilde{u}_k)_{k=1,\cdots,n^C} & \partial_t \overline{u} & \partial_t (\widetilde{u}_k)_{k=1,\cdots,n^C} \end{pmatrix}$ the state variable, $u^T = \begin{pmatrix} f^B & (f_k^C)_{k=1,\cdots,n^C} \end{pmatrix}$ the control variable. The LQR problem, consisting

in minimizing the functional under the constraint, can be written under its usual form as

$$\begin{array}{l} \frac{dz}{dt} = Az(t) + Bu(t) \text{ for } t > 0 \text{ and } z(0) = z_0, \\ \min\limits_{u \in U} J(z_0, u) = \min\limits_{u \in U} \int_0^{+\infty} ||Cz||_Y^2 + (Su, u)_U dt. \end{array} \tag{4.2}$$

where $A = \begin{pmatrix} 0 & Id \\ -M_{array}^{-1} K_{array} & 0 \end{pmatrix}$ the state operator, with the matrices M_{array} and K_{array}

$$M_{array} = \begin{pmatrix} \rho^B & 0 \\ m^{C0} L_C^0 \bar{\varphi}_k & m^{C0} L_C^0 Id \end{pmatrix},$$

and

$$K_{array} = \begin{pmatrix} R^B \partial^4_{x_1 \cdots x_1} & 0 \\ 0 & \frac{R^C \lambda_k^C + L_C^0 \ell_C^0 r^{C0} c_k}{(L_C^0)^4} Id \end{pmatrix},$$

Id is the identity matrix with size $n^C + 1$ and $B = \begin{pmatrix} 0 \\ M_{array}^{-1} \end{pmatrix}$ the control operator,

$$C = \begin{pmatrix} \partial^2_{xx} & 0 & 0 & 0 \\ 0 & Id & 0 & 0 \\ 0 & 0 & 0 & 0 \\ 0 & 0 & 0 & 0 \end{pmatrix}$$

the observation operator, and $S = Id$ the weight operator. The choice for B and C is the simplest one so that it can guarantee the controllability and observability of the system. We denote by $\mathcal{X}$ the space $L^2(\Gamma)$. Here, A is the infinitesimal generator of a continuous semigroup on the separable Hilbert space $\mathcal{Z} = H_0^2(\Gamma) \times \mathcal{X}^{n^C} \times \mathcal{X} \times \mathcal{X}^{n^C}$ with dense domain $D(A) = H^4(\Gamma) \cap H_0^2(\Gamma) \times \mathcal{X}^{n^C} \times H_0^2(\Gamma) \times \mathcal{X}^{n^C}$. It is known that the control operator $B \in \mathcal{L}(\mathcal{U}, \mathcal{Z})$, the observation operator $C \in \mathcal{L}(\mathcal{Z}, \mathcal{Y})$, and $S \in \mathcal{L}(\mathcal{U}, \mathcal{U})$, where $\mathcal{Y} = \mathcal{X}^{2(n^C+1)}$ and $\mathcal{U} = \mathcal{X}^{n^C+1}$. We admit that (A, B) is stabilizable and that (A, C) is detectable, in the sense that there exist $G \in \mathcal{L}(\mathcal{Z}, \mathcal{U})$ and $F \in \mathcal{L}(\mathcal{Y}, \mathcal{Z})$ such that $A - BG$ and that $A - FC$ are the infinitesimal generators of two uniformly exponentially stable continuous semigroups. It follows that for each $z_0 \in \mathcal{Z}$, the LQR problem (4.2) admits a unique solution

$$u^* = -Kz \tag{4.3}$$

where $K = S^{-1} B^* P z$, and P is the unique self-adjoint nonnegative solution of the operational Riccati equation

$$\left(A^* P + PA - PBS^{-1} B^* P + C^* C\right) z = 0, \tag{4.4}$$

for all $z \in D(A)$, see [56]. The adjoint A^* of the unbounded operator A is defined from $D(A^*) \subset \mathcal{Z}$ to $\mathcal{Z}$ by the equality $(A^* z, z')_{\mathcal{Z}} = (z, Az')_{\mathcal{Z}}$ for all $z \in D(A^*)$ and $z' \in D(A)$. The adjoint $B^* \in \mathcal{L}(\mathcal{Z}, U)$ of the bounded operator B is defined by $(B^* z, u)_{\mathcal{U}} = (z, Bu)_{\mathcal{Z}}$, the adjoint $C^* \in \mathcal{L}(\mathcal{Y}, \mathcal{Z})$ is defined similarly.

4.1.2 Derivation of Semi-decentralized Approximation Method

This section is devoted to formulate the approximation method. Its mathematical derivation has been introduced in the paper [39] and detailed in the thesis [40] where many illustrating examples have been presented.

Matrices of functions of a self-adjoint operator

We denote by Λ, the mapping: $\Lambda : f \longrightarrow w$, where w is the unique solution of $\partial^4_{x\cdots x} w = f$ in Γ with the boundary conditions $w = \partial_x w = 0$ for $x = \{0, L_B\}$. The spectrum σ of Λ is discrete and made up of real eigenvalues λ_k. They are solutions to the eigenvalue problem $\Lambda\phi_k = \lambda_k\phi_k$ with $||\phi_k||_{L^2(\Gamma)} = 1$. In the sequel, $I_\sigma = (\sigma_{\min}, \sigma_{\max})$ refers to an open interval that includes the complete spectrum. For a given real valued function g, continuous on I_σ, $g(\Lambda)$ is the linear self-adjoint operator on the space $\mathcal{X}$ defined by $g(\Lambda)z = \sum_{k=1}^{\infty} g(\lambda_k) z_k \phi_k$, where $z_k = \int_\Gamma z\phi_k \, dx$.

Factorization of K by a Matrix of Functions of Λ

In this part, we introduce the factorization of the controller K under the form of a product of a matrix of functions of Λ. To do so, we introduce the operators of change of variables $\Phi_Z = \begin{pmatrix} \Lambda^{\frac{1}{2}} & 0 & 0 & 0 \\ 0 & Id & 0 & 0 \\ 0 & 0 & Id & 0 \\ 0 & 0 & 0 & Id \end{pmatrix} \in \mathcal{L}\left(\mathcal{X}^{2(n^C+1)}, \mathcal{Z}\right)$, $\Phi_U = Id \in \mathcal{L}\left(\mathcal{X}^{n^C+1}, \mathcal{U}\right)$ and $\Phi_Y = \begin{pmatrix} \partial^2_{xx}\Lambda^{\frac{1}{2}} Id & 0 & 0 & 0 \\ 0 & Id & 0 & 0 \\ 0 & 0 & Id & 0 \\ 0 & 0 & 0 & Id \end{pmatrix} \in \mathcal{L}\left(\mathcal{X}^{2(n^C+1)}, \mathcal{Y}\right)$, from which we introduce the matrices of functions of Λ, $a(\Lambda) = \Phi_Z^{-1} A \Phi_Z, b(\Lambda) = \Phi_Z^{-1} B \Phi_U, c(\Lambda) = \Phi_Y^{-1} C \Phi_Z$ and $s(\Lambda) = \Phi_U^{-1} S \Phi_U$, simple to implement on a semi-decentralized architecture. A straightforward calculation yields

$$a(\lambda) = \begin{pmatrix} 0 & 0 & \Lambda^{-\frac{1}{2}} & 0 \\ 0 & 0 & 0 & Id \\ -\frac{R^B}{\rho^B}\Lambda^{-\frac{1}{2}} & 0 & 0 & 0 \\ \frac{R^B \bar{\phi}_k^T}{\rho^B}\Lambda^{\frac{1}{2}} & -\frac{r^{C0}}{(L_C^0)^4} diag(\lambda_k^C + L_C^0 \ell_C^0 c_k) & 0 & 0 \end{pmatrix}, \; b(\lambda) = \begin{pmatrix} 0 \\ M_{array}^{-1} \end{pmatrix},$$

$$c(\lambda) = \begin{pmatrix} Id & 0 \\ 0 & 0 \end{pmatrix}, \text{ and } s(\lambda) = Id.$$

Endowing $\mathcal{Z}$, $\mathcal{U}$ and $\mathcal{Y}$ with the inner products $(z,z')_{\mathcal{Z}} = \left(\Phi_Z^{-1}z, \Phi_Z^{-1}z'\right)_{\mathcal{X}^{2n^C+2}}$, $(u,u')_{\mathcal{U}} = \left(\Phi_U^{-1}u, \Phi_U^{-1}u'\right)_{\mathcal{X}^{n^C+1}}$, and $(y,y')_{\mathcal{Y}} = \left(\Phi_Y^{-1}y, \Phi_Y^{-1}y'\right)_{\mathcal{X}^{2n^C+2}}$, we find the subsequent factorization of the controller K in (4.3) which plays a central role in the approximation.

Proposition 4 *The controller K admits the factorization*

$$K = \Phi_U q(\Lambda) \Phi_Z^{-1},$$

where $q(\lambda) = s^{-1}(\lambda) b^T(\lambda) p(\lambda)$, and where for all $\lambda \in \sigma$, $p(\lambda)$ is the unique self-adjoint nonnegative matrix solving the algebraic Riccati equation.

$$a^T(\lambda) p + pa(\lambda) - pb(\lambda) s^{-1}(\lambda) b^T(\lambda) p + c^T(\lambda) c(\lambda) = 0. \tag{4.5}$$

Proof. The algebraic Riccati equation can be found after replacing A, B, C and S by their decomposition

$$A = \Phi_Z a(\Lambda) \Phi_Z^{-1}, B = \Phi_Z b(\Lambda) \Phi_U^{-1}, C = \Phi_Y c(\Lambda) \Phi_Z^{-1} \text{ and } S = \Phi_U s(\Lambda) \Phi_U^{-1}.$$

in the Riccatti equation (4.4). ■

Remark 5 *In this example, Φ_U and Φ_Z are some matrices of functions of Λ, and so is K,*

$$K = k(\Lambda). \tag{4.6}$$

Thus, the approximation is developed directly on $k(\Lambda)$, but we emphasize that in more generic situations it is pursued on $q(\Lambda)$.

Remark 6 *Introducing the isomorphisms Φ_Z, Φ_Y, and Φ_U allows to consider a broad class of problems where the operators A, B, C and S are not strictly functions of a same operator. In this particular application, the observation operator C is composed with the operator ∂_{xx}^2. This is taken into account in Φ_Y in a manner in which $\Phi_Y^{-1} C \Phi_Z$ is a function of Λ only.*

Remark 7 *We indicate how the isomorphisms Φ_Z, Φ_Y, and Φ_U have been chosen. The choice of Φ_Z comes directly from the expression of the inner product $(z,z')_Z = \left(\Phi_Z^{-1}z, \Phi_Z^{-1}z'\right)_{(L^2(\Gamma))^{2N}}$ and from*

$$(z_n, z_n')_{H_0^2(\Gamma)} = \left((\Delta^2)^{\frac{1}{2}} z_n, \quad (\Delta^2)^{\frac{1}{2}} z_n'\right)_{L^2(\Gamma)}$$

with $n = 1, .., N$. For Φ_Y, we start from $C = \Phi_Y c(\Lambda) \Phi_Z^{-1}$ and from the relation

$$(y,y')_Y = \left(\Phi_Y^{-1} y, \Phi_Y^{-1} y'\right)_{(L^2(\Gamma))^{2N}}$$

which implies that $\partial_{xx}^2 = (\Phi_Y)_{i,i} c_{i,i}(\Lambda) \Lambda^{-\frac{1}{2}}$ and $0 = (\Phi_Y)_{j,j} c_{j,j} \Lambda$ with $i = 1, .., N$ and $j = N+1, .., 2N$. The expression of Φ_Y follows. Choosing Φ_U is straightforward.

Approximation of Functions of Λ

Our approximation method is based on the Cauchy integral formula from functional calculus, see [57], representing a function of an operator. We build the approximation in two steps. Since the function $k(\Lambda)$ is not known, the spectrum σ cannot be easily determined, so firstly, the function is approximated by a highly accurate rational approximation. We notice that $k(\lambda)$ may be a singular function when λ approaches to 0, (see Figure 4.1).

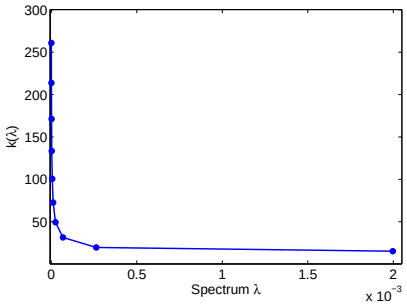

Figure 4.1: One component of the function $k(\lambda)$

To avoid the singularity of $k(\lambda)$, for each component $k_{ij}(\lambda)$, we introduce a componentwise rational approximation, operating on the logarithm of λ instead of on λ as done in [39], [40]

$$k_R(\lambda) = \frac{\sum_{m=0}^{R^N} d_m (\ln \lambda)^m}{\sum_{m'=0}^{R^D} d'_{m'} (\ln \lambda)^{m'}}, \tag{4.7}$$

where d_m, $d'_{m'}$ are two coefficient matrices, and $R = \left(R^N, R^D\right)$ is a couple of matrices of polynomial degrees. Now, we approximate $k_R(\lambda)$ by another function $k_{R,M}(\lambda)$ which is simple to discretize. To do so, we use the Cauchy integral formula,

$$k_R(\Lambda) = \frac{1}{2i\pi} \int_{\mathcal{C}} k_R(\zeta) \left(\zeta Id - \Lambda\right)^{-1} \, d\zeta, \tag{4.8}$$

because it involves only the resolvent $(\zeta I - \Lambda)^{-1}$, which may be simply and accurately approximated. We apply it to the rational approximation with a path $\mathcal{C}$ tracing out an ellipse including I_σ but no poles. It is chosen to be an ellipse parameterized by

$$\zeta(\theta) = \zeta_1(\theta) + i\zeta_2(\theta), \text{ with } \theta \in [0, 2\pi],$$

(see Figure 4.2). The parametrization is used as a change of variable, so the integral can be approximated by a quadrature formula involving M nodes $(\theta_l)_{l=1,..,M} \in [0, 2\pi]$, and M weights $(\omega_l)_{l=1,..,M}$,

$$I_M(g) = \sum_{l=1}^{M} g(\theta_l)\,\omega_l.$$

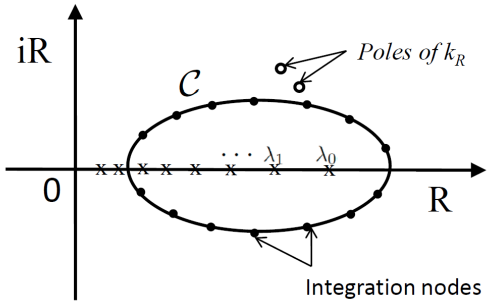

Figure 4.2: The contour in the Cauchy integral formula

So, for each $z \in \mathcal{X}^{2(n^C+1)}$ and $\zeta \in \mathcal{C}$, we introduce the $2(n^C+1)$-dimensional vector field

$$v^\zeta = -i\zeta' k_R(\zeta)\,(\zeta Id - \Lambda)^{-1} z.$$

Decomposing v^ζ into its real part v_1^ζ and its imaginary part v_2^ζ, the couple (v_1^ζ, v_2^ζ) is solution of the system

$$\begin{cases} \zeta_1 v_1^\zeta - \zeta_2 v_2^\zeta - \Lambda v_1^\zeta = Re\left(-i\zeta' k_R(\zeta)\right) z, \\ \zeta_2 v_1^\zeta + \zeta_1 v_2^\zeta - \Lambda v_2^\zeta = Im\left(-i\zeta' k_R(\zeta)\right) z. \end{cases} \tag{4.9}$$

Thus, combining the rational approximation k_R and the quadrature formula yields an approximate realization $k_{R,M}(\Lambda)$ of $k(\Lambda)$,

$$k_{R,M}(\Lambda)\, z = \frac{1}{2\pi} \sum_{l=1}^{M} v_1^{\zeta(\theta_l)} \omega_l. \tag{4.10}$$

This formula is central in the method, so it is the center of our attention in the simulations. A fundamental remark is that, a "real-time" realization, $k_{R,M}(\Lambda)\, z$, requires solving M systems like (4.9) corresponding to the M quadrature nodes $\zeta(\theta_l)$. The matrices $k_R(\zeta(\theta_l))$ could be computed "off-line" once and for all, and stored in memory, so their determination would not penalize a rapid real-time computation. In total, the ultimate parameter responsible of accuracy in a real-time computation, apart from spatial discretization, is M the number of quadrature points.

Spatial Discretization

The final step in the approximation consists in a spatial discretization and synthesis of equation (4.9). The interval Γ is meshed with regularly spaced nodes separated by a distance h, we introduce Λ_h^{-1} the finite difference discretization of Λ^{-1}, associated with the clamping boundary condition. In practice, the discretization length h is chosen small compared to the distance between cantilevers. Then, z_h denoting the vector of nodal values of z, for each ζ we introduce $(v_{1,h}^{\zeta}, v_{2,h}^{\zeta})$, a discrete approximation of $(v_1^{\zeta}, v_2^{\zeta})$, solution of the discrete set of equations,

$$\zeta_1 v_{1,h}^{\zeta} - \zeta_2 v_{2,h}^{\zeta} - \Lambda_h v_{1,h}^{\zeta} = Re\left(-i\zeta' k_R\left(\zeta\right)\right) z_h, \tag{4.11}$$

$$\zeta_2 v_{1,h}^{\zeta} + \zeta_1 v_{2,h}^{\zeta} - \Lambda_h v_{2,h}^{\zeta} = Im\left(-i\zeta' k_R\left(\zeta\right)\right) z_h. \tag{4.12}$$

Finally, an approximate optimal control, intended to be implemented in a set of spatially distributed actuators, could be estimated from the nodal values at mesh nodes,

$$k_{R,M,h} z_h = \frac{1}{2\pi} \sum_{l=1}^{M} v_{1,h}^{\zeta_l} \omega_l.$$

- Analog Computation of $\Lambda_h v_1$ and $\Lambda_h v_2$

We propose a synthesis of (4.11-4.12) by a distributed electronic circuit that could be integrated in a physical device. For this purpose, the system is rewritten under the manageable form

$$v_1 = \frac{\zeta_1}{\zeta_1^2 + \zeta_2^2}\left(\alpha + \Lambda_h v_1\right) + \frac{\zeta_2}{\zeta_1^2 + \zeta_2^2}\left(\beta + \Lambda_h v_2\right), \tag{4.13}$$

$$v_2 = \frac{\zeta_1}{\zeta_1^2 + \zeta_2^2}\left(\beta + \Lambda_h v_2\right) - \frac{\zeta_2}{\zeta_1^2 + \zeta_2^2}\left(\alpha + \Lambda_h v_1\right), \tag{4.14}$$

where we use the notations $\alpha = Re\left(-i\zeta' k_R\left(\zeta\right)\right) z_h$, $\beta = Im\left(-i\zeta' k_R\left(\zeta\right)\right) z_h$, $v_1 = v_{1,h}^{\zeta}$, and $v_2 = v_{2,h}^{\zeta}$. The analog computation of $\Lambda_h v_1$ and $\Lambda_h v_2$ are made by Periodic Network of Resistances (PNR) circuits [54]. These electronic circuits have been developed to solve a large class of PDEs by analog computation. More exactly, PNR circuits compute the finite difference solution of a PDE. PNR circuits are gathering of cells (Figure 4.3), the interior cells are indexed by $k = 1, \ldots, N-1$, while the boundary cells correspond to $k = -1, 0, N$ and $N+1$. We will show that the circuits solve the equations $Au_1 = i_1$. If the current sources i_1 are replaced by voltage controlled current sources defined by $i_1 = gv_1$ (with g is a real number), the voltage outputs of the circuits u_1 solve $g(\Lambda_h v_1)$ and so $\Lambda_h v_1$. The computation of $\Lambda_h v_2$ is done in the same way. The interior cell k which computes $(\Lambda_h v_1)_k$ is

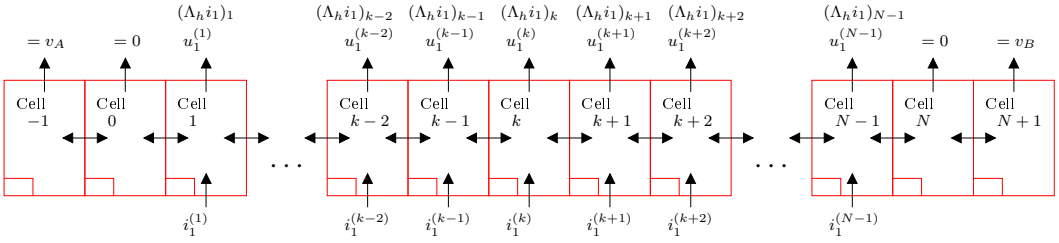

Figure 4.3: Analog computation of $\Lambda_h v_1$.

represented on Figure 4.4 with its two adjacent cells on each side. We call ρ_1 the resistance value between the potentials $u_1^{(k)}$ and $u_1^{(k\pm 2)}$, and ρ_2 the resistance value between the potentials $u_1^{(k)}$ and $u_1^{(k\pm 1)}$. By applying the Kirchhoff Current Law

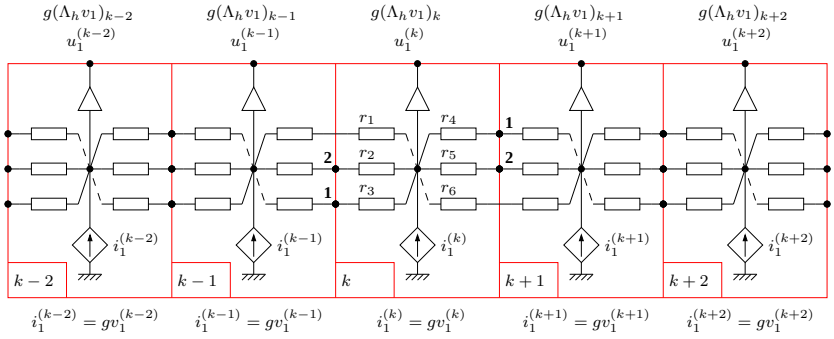

Figure 4.4: Five adjacent interior cells.

(KCL) at node $u_1^{(k)}$, rearranging some terms and dividing by h^4, the equation of the cell k can be written under the form:

$$\begin{aligned}\tfrac{1}{h^4} - \tfrac{1}{\rho_1}u_1^{(k-2)} - \tfrac{1}{\rho_2}u_1^{(k-1)} + 2u_1^{(k)}\left(\tfrac{1}{\rho_1}+\tfrac{1}{\rho_2}\right)\\ -\tfrac{1}{\rho_2}u_1^{(k+1)} - \tfrac{1}{\rho_1}u_1^{(k+2)} = \tfrac{1}{h^4}i_1^{(k)}.\end{aligned}$$

If one choose the negative potential $\rho_1 = -h^4\rho_0$ and the positive potential $\rho_2 = h^4\rho_0/4$, then the potential at node $u_1^{(k)}$ is expressed as a function of its neighbor voltages as

$$\frac{1}{h^4}u_1^{(k-2)} - 4u_1^{(k-1)} + 6u_1^{(k)} - 4u_1^{(k+1)} + u_1^{(k+2)} = \rho_0 i_1^{(k)},$$

which is the stencil of the differential operation Λ^{-1}. Consequently, the whole electronic circuit composed of $N-1$ cells computes the finite differences approximation

$u_1 = \Lambda_h i_1 = g(\Lambda_h v_1)$. The numerical value of ρ_0 only changes the magnitude of the voltages $u_1^{(k)}$. The values of the resistances inside a cell depend only on the circuit topology and are easily expressed as a function of ρ_1 or ρ_2. Here the resistances of the cells can be taken as $r_1 = r_3 = r_4 = r_6 = \rho_1/4$ and $r_2 = r_5 = \rho_2/2$.

The Voltage Controlled Current Source (VCCS) $i_1^{(k)}$ of Figure 4.4 is controlled by the voltage $v_1^{(k)}$ through the equation $i_1^{(k)} = g v_1^{(k)}$. The four boundary cells are represented on Figure 4.5. The imposed values of the voltages correspond to the clamping boundary condition. Remark that the terminals denoted by a cross are not connected, so the resistances which are linked by one side at them can be removed without changing the behavior of the circuits. They are saved to show clearly the real difference between interior cells and boundary cells.

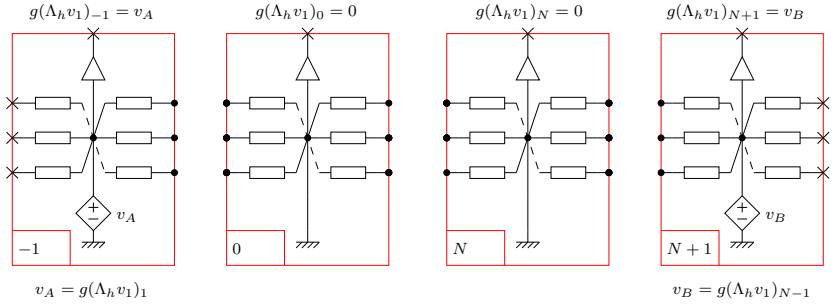

Figure 4.5: Four boundary cells.

- Analog Computation of Equation (4.13)

The analog computation of (4.13) can be made by an array of classical non inverting summing amplifiers of Figure 4.6. Notice that there is no current exchange between these circuits and PNR inputs and outputs, see buffers in Figure 4.4. Analysis of the circuit of Figure 4.6 leads to (4.15). With a proper choice of resistances, Figure 4.6 solves (4.13),

$$v_1^{(k)} = \frac{R_1 + R_2}{R_1}\frac{R_u}{R_a}\alpha + \frac{R_u}{R_b} g(\Lambda_h v_1)_k + \frac{R_u}{R_c}\beta + \frac{R_u}{R_d} g(\Lambda_h v_2)_k , \tag{4.15}$$

where $\frac{1}{R_u} = \frac{1}{R_a} + \frac{1}{R_b} + \frac{1}{R_c} + \frac{1}{R_d}$.

- Analog Computation of Equation (4.14)

In a very similar way, the analog computation of equation (4.14) can be made by an array of classical difference summing amplifiers of Figure 4.7.

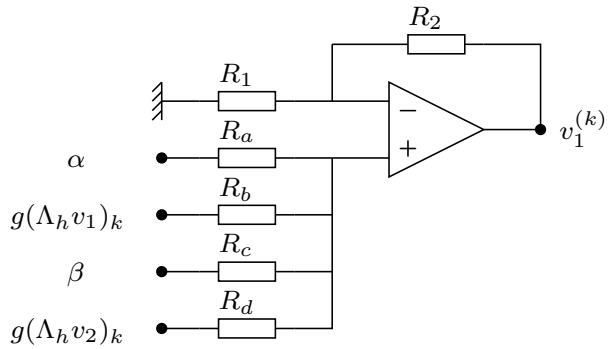

Figure 4.6: Analog computation of the k-th equation (4.13).

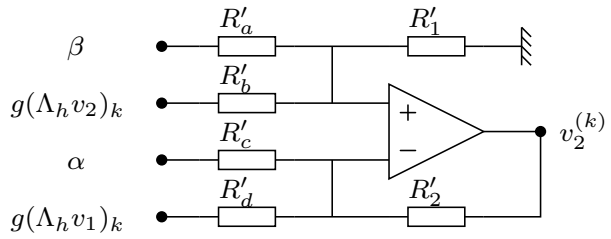

Figure 4.7: Analog computation of the k-th equation (4.14).

Analysis of the circuit of Figure 4.7 leads to (4.16). With a proper choice of resistances, Figure 4.7 solves (4.14),

$$v_2^{(k)} = \frac{R_v}{R_w}\frac{R'_2}{R'_a}\beta + \frac{R_v}{R_w}\frac{R'_2}{R'_b} g\left(\Lambda_h v_2\right)_k - \frac{R'_2}{R'_c}\alpha - \frac{R'_2}{R'_d} g\left(\Lambda_h v_1\right)_k , \tag{4.16}$$

where $\frac{1}{R_v} = \frac{1}{R'_a} + \frac{1}{R'_b} + \frac{1}{R'_1}$ and $\frac{1}{R_w} = \frac{1}{R'_c} + \frac{1}{R'_d} + \frac{1}{R'_2}$.

4.2 H_∞ Filtering Problem Based on Functional Calculus

In this section, we extend our semi-decentralized approximation method to a modern control theory, i.e. a robust H_∞ control problem. We focus on an H_∞ filtering problem using interferometry measurements of the displacements for AFM arrays which has been introduced in chapter 3. Here, we improve the quadrature rule used for the Cauchy integral thanks to the approach presented in [58]. This significantly improves the computation of the function $k(\lambda)$ when λ is closed to 0 and improves the accuracy of the quadrature rule.

4.2.1 Statement of H_∞ Filtering Problem

For the filtering problem in AFM array application we take into account unknown noise associated to interferometry measurements as well as other noise sources as air or liquid environment, thermal effect, electromagnetic noise. To deal with these uncertainties, we uses an H_∞ theory which is based on the worst case approach. According to the dynamic equation of (4.1) stated in section 4.1.1, we set the state variable $z^T = \begin{pmatrix} \overline{u} & (\widetilde{u}_k)_{k=1,\cdots,n^C} & \partial_t\overline{u} & \partial_t(\widetilde{u}_k)_{k=1,\cdots,n^C} \end{pmatrix}$, the state operator A and $B = \begin{pmatrix} 0 & Id \end{pmatrix}^T$ the perturbation operator. The perturbations in the state system being denoted by $w_1 \in \mathcal{W}_1 = \mathcal{X} \times \mathcal{X}^{n^C}$, the state equation is

$$\partial_t z = Az + Bw_1 \text{ for } t \in \mathbb{R}^+ \text{ and } z(0) = z_0. \tag{4.17}$$

Here A is the infinitesimal generator of a continuous semigroup on the separable Hilbert space $\mathcal{Z} = H_0^2(\Gamma) \times \mathcal{X}^{n^C} \times \mathcal{X} \times \mathcal{X}^{n^C}$ with dense domain $D(A) = H^4(\Gamma) \cap H_0^2(\Gamma) \times \mathcal{X}^{n^C} \times H_0^2(\Gamma) \times \mathcal{X}^{n^C}$. The perturbations operator $B \in \mathcal{L}(\mathcal{W}_1, \mathcal{Z})$.

The observation comes from interferometry measurement but takes into account an additional unknown noise w_2. We observe the phase of base profile plus a very small constant which has not effect on the observation in normalized domain, as introduced in section 3.1.2. Then, using the modal decomposition with respect to y_2, the noise disturbed measurement turns to be given by

$$Y = Cz + Dw_2 \in \mathcal{Y} = \mathcal{X}$$

the space of measurements, with the observation operator

$$C = \begin{pmatrix} -\frac{4\pi}{\bar{\lambda}} Id & -\frac{4\pi}{\bar{\lambda}} \varphi_k(y_2^{0,1})_{k=1,..,n^C} & 0 & 0 \end{pmatrix} \in \mathcal{L}(\mathcal{H}, \mathcal{Y}), w_2 \in \mathcal{W}_2,$$

with $\bar{\lambda}$ is the light wave length and the weight operator for the measurement noise $D = Id \in \mathcal{L}(\mathcal{W}_2, \mathcal{Y})$. We assume that (A, B) is stabilizable and that (C, A) is detectable. The output operator is $L : \mathcal{Z} \longrightarrow \mathcal{Z}^N$, and the partial state to be estimated is

$$Z = Lz.$$

Here, we estimate the displacement at base, so $L = \begin{pmatrix} Id & 0 & 0 & 0 \end{pmatrix}$ and $\mathcal{Z}^N = H_0^2(\Gamma)$. We define the estimation $\widehat{Z}$ of Z and the worst-case performance measures as

$$J = \sup_{(z_0, \mathcal{W}_1 \times \mathcal{W}_2)} \frac{||Z - \widehat{Z}||^2_{\mathcal{Z}^N}}{||w_1||^2_{\mathcal{W}_1} + ||w_2||^2_{\mathcal{W}_2}}.$$

The filtering problem is stated as: Given $\gamma > 0$, find a filter $Y \longrightarrow Z$, such that $J < \gamma^2$. This problem has a solution if and only there exists a unique self-adjoint non-negative solution P to the operational Riccati equation, [59].

$$(AP + PA^* - PC^*CP + \frac{1}{\gamma^2} PL^*LP + BB^*)y = 0, \tag{4.18}$$

for all $y \in D(A^{N*})$. The filter $Y \mapsto \hat{Z}$ is given as follows

$$\begin{aligned} \partial_t \hat{z} &= A\hat{z} + Ky, \\ \hat{Z} &= L\hat{z} \quad \text{for } t \in \mathbb{R}^+, \end{aligned} \tag{4.19}$$

where the filter gain is $K = P\mathcal{C}^{N*}$ and $y = Y - C\hat{z}$.

4.2.2 Functional Calculus Based Approximation

As introduced in section 4.1.2, we have the factorization of the filter gain K under the form of a product of a matrix of functions of Λ. Here, we introduce the change of variable operators

$$\Phi_H = \begin{pmatrix} \Lambda^{\frac{1}{2}} & 0 & 0 & 0 \\ 0 & Id & 0 & 0 \\ 0 & 0 & Id & 0 \\ 0 & 0 & 0 & Id \end{pmatrix} \in \mathcal{L}\left(\mathcal{X}^{2(n^C+1)}, \mathcal{Z}\right),$$

$\Phi_W = Id \in \mathcal{L}\left(\mathcal{X}^{n^C+1}, \mathcal{W}_1\right)$, $\Phi_Z = \Lambda^{\frac{1}{2}} \in \mathcal{L}\left(\mathcal{X}, \mathcal{Z}^N\right)$, and $\Phi_Y = Id \in \mathcal{L}\left(\mathcal{X}, \mathcal{Y}\right)$, from which we introduce the matrices of functions of Λ, $a(\Lambda) = \Phi_H^{-1} A \Phi_H$, $b(\Lambda) = \Phi_H^{-1} B \Phi_W$, $c(\Lambda) = \Phi_Y^{-1} C \Phi_H$ and $\ell(\Lambda) = \Phi_Z^{-1} L \Phi_H$, simple to implement on a semi-decentralized architecture. We note that the filter gain K in (4.19) is function of operator Λ.

Proposition 8 *The filter gain K admits the factorization $K = \Phi_H q(\Lambda) \Phi_Y$, where $q(\lambda) = p(\lambda) c^T(\lambda)$, and where for all $\lambda \in \sigma$, $p(\lambda)$ is the unique symmetric non-negative matrix solving the algebraic Riccati equation*

$$ap + pa^T - p(\bar{c}^T \bar{c} - \frac{1}{\gamma^2} \bar{\ell}^T \bar{\ell}) p + \bar{b}\bar{b}^T = 0.$$

where $\bar{\ell}(\lambda) = \Phi_Z(\lambda)\ell(\lambda)$, $\bar{c}(\lambda) = \Phi_Y^{-1}(\lambda) c(\lambda)$ and $\bar{b}(\lambda) = b(\lambda)\Phi_W^{-1}(\lambda)$.

Approximation of Functions of Λ

We refer to the same rational approximation and Cauchy integral formula as stated in section 4.1.2. In order to improve the accuracy of the approximation, before computing $k_R(\Lambda)$, a slight change should be done for the formula (4.8),

$$k_R(\Lambda) = \frac{\Lambda}{2i\pi} \int_{\mathcal{C}_\zeta} \zeta^{-1} k_R(\zeta) (\zeta Id - \Lambda)^{-1} \, d\zeta. \tag{4.20}$$

We introduce a new variable $\omega = \zeta^{1/2}$, and $d\zeta = 2\omega d\omega$, then the above formula becomes

$$k_R(\Lambda) = \frac{\Lambda}{i\pi} \int_{\mathcal{C}_\omega} \omega^{-1} k_R(\omega^2) \left(\omega^2 Id - \Lambda\right)^{-1} \, d\omega. \tag{4.21}$$

Thus we have a new contour integral problem, where the contour maps from ζ-plane to ω-plane and encloses $[\lambda_{\min}^{1/2}, \lambda_{\max}^{1/2}]$, (see Figure 4.8). The integral can be approximated by a quadrature formula involving M nodes.

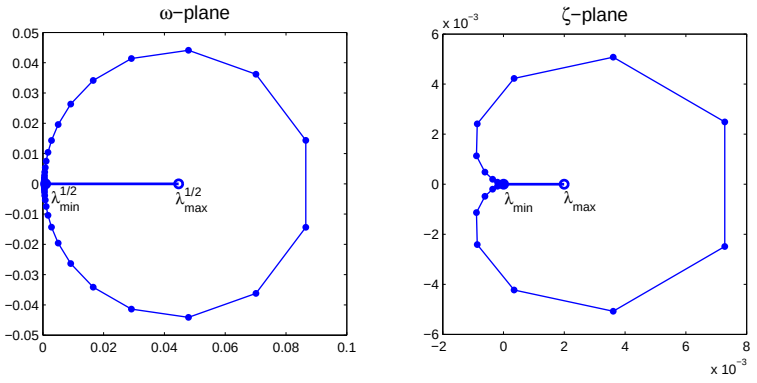

Figure 4.8: The contour in the Cauchy integral formula

We apply the trapezoid rule with M equally spaced nodes in $(-K_p + iK_p'/2, K_p + iK_p'/2)$, the Cauchy integral formula for the method applied to Λ can be written as

$$k_{R,M}(\Lambda) = \frac{-8K_p\Lambda(\lambda_{\min}\lambda_{\max})^{1/4}}{iMk_p} \operatorname{Im} \sum_{l=1}^{M} \frac{k_R(\omega^2(t_l)) \left(\omega^2(t_l)I - \Lambda\right)^{-1} cn(t_l)dn(t_l)}{\omega(t_l)(k_p^{-1} - sn(t_l))^2},$$

where $t_l = -K_p + \frac{iK_p'}{2} + 2\frac{(l-\frac{1}{2}K_p)}{M}$, $1 \le l \le M$, the values of K_p and K_p' are the complete elliptic integrals associated with the parameters k_p

$$k_p = \frac{(\lambda_{\max}/\lambda_{\min})^{1/4} - 1}{(\lambda_{\max}/\lambda_{\min})^{1/4} + 1}.$$

The Jacobi elliptic function

$$u = sn(t_l) = sn(t|k_p^2),$$

and the combination of the further Jacobi elliptic functions

$$cn(t_l)dn(t_l) = \sqrt{1 - k_p^2u^2}\sqrt{1 - u^2}.$$

Finally, the transformation

$$\omega = (\lambda_{\min}\lambda_{\max})^{1/4}\frac{(k_p^{-1} + sn(t))}{(k_p^{-1} - sn(t))}.$$

We decompose ζ into their real part ζ_1 and their imaginary part ζ_2, and we define the function

$$h^\zeta = \frac{8K_p(\lambda_{\min}\lambda_{\max})^{1/4}cn(t_l)dn(t_l)}{Mk_p(\zeta^l)^{1/2}(k_p^{-1} - sn(t_l))^2}.$$

So, for each $y = Y - C\hat{z} \in \mathcal{X}^{2(n^C+1)}$ and $\zeta \in \mathcal{C}_\zeta$, we introduce the $2(n^C + 1)$-dimensional vector field

$$v^\zeta = \Lambda h^\zeta k_R(\zeta)(\zeta I - \Lambda)^{-1} y$$

and its real part v_1^ζ and its imaginary part v_2^ζ, the couple (v_1^ζ, v_2^ζ) is solution of the system

$$\begin{cases} \Lambda^{-1}\zeta_1 v_1^\zeta - \Lambda^{-1}\zeta_2 v_2^\zeta - v_1^\zeta = Re(h^\zeta k_R(\zeta))y, \\ \Lambda^{-1}\zeta_2 v_1^\zeta + \Lambda^{-1}\zeta_1 v_2^\zeta - v_2^\zeta = Im(h^\zeta k_R(\zeta))y. \end{cases} \tag{4.22}$$

Thus, combining the rational approximation k_R and the contour integration formula yields an approximate realization $k_{R,M}(\Lambda)\, y$ of $k(\Lambda)\, y$,

$$k_{R,M}(\Lambda)\, y = \sum_{l=1}^{M} v_1^{\zeta_l}. \tag{4.23}$$

where M is the number of quadrature points.

Spatial Discretization

The final step in the approximation consists in a spatial discretization and synthesis of Equation (4.22). The interval Γ is also meshed with regularly spaced nodes separated by a distance h. Denoting by y_h the vector of nodal values of y, for each ζ we introduce $(v_{1,h}^\zeta, v_{2,h}^\zeta)$, a discrete approximation of (v_1^ζ, v_2^ζ), solution of the discrete set of equations,

$$\begin{cases} \Lambda_h^{-1}\zeta_1 v_{1,h}^\zeta - \Lambda_h^{-1}\zeta_2 v_{2,h}^\zeta - v_{1,h}^\zeta = Re(h^\zeta k_R(\zeta))y_h, \\ \Lambda_h^{-1}\zeta_2 v_{1,h}^\zeta + \Lambda_h^{-1}\zeta_1 v_{2,h}^\zeta - v_{2,h}^\zeta = Im(h^\zeta k_R(\zeta))y_h. \end{cases} \tag{4.24}$$

Finally, an approximate optimal filter could be estimated from the nodal values,

$$k_{R,M,h}y_h = \sum_{l=1}^{M} v_{1,h}^{\zeta_l}.$$

4.3 Conclusion

We have presented the derivation of a semi-decentralized approximation method and its applications to an LQR control problem and an H_∞ filtering problem for one-dimensional cantilever arrays. The resulting semi-decentralized control can be realized by PNR circuits. We notice that the entire approach is general and it can be extended to other linear optimal control problems, e.g. LQG or H_∞ controls. It may apply or be adapted to other systems including a cantilever array, for instance to parallel AFMs or to storage devices, like the millipede, see [5].

Chapter 5

CONCLUSIONS AND PERSPECTIVES

A two-scale model of cantilever arrays in dynamic regime has been presented. Its derivation, previously carried out, uses a theory of strongly heterogeneous homogenization in which the cantilevers play the role of soft parts. In the resulting model, only the transverse displacement was retained. We analyzed it and compared it to ordinary finite element simulations from the viewpoint of modal structure. A special emphasis was placed on the distinction between modes dominated by base deformation and those dominated by cantilever deformation. We observe that this concept can be met in various kinds of arrays of coupled systems, so the analysis methodology could be re-used in other applications.

The two-scale model and the direct finite element model provide comparable results but some modes are not absolutely correct. A possible way to improve the current model would be to take into account the three mechanical displacements rather than the transverse displacement only. The different phases of the design optimization problem of AFM arrays have been described. For a static design problem based on a two-scale model of AFM arrays, the design variables space X is defined, as well as the response feature space S, the design objective functions $F_i(x)$ and the design nonlinear constraints space C. We have demonstrated that it is possible to:

1. Select a set of influential design variables based on sensitivity analysis.

2. Find an optimal solution of the constrained design problem using both mono-objective and multi-objective optimization algorithms.

3. Quantify the impact of manufacturing uncertainties on the performance characteristics of the AFM array.

The implemented tools provide an effective means for supporting the decision making process in arrays of AFM design.

The measurement of cantilever displacements is done by an interferometric readout method. We have presented an effective global phase computation algorithm based on the least square method . Positive results of sample surface topographic scan application for an array of AFMs have been reported.

Our semi-decentralized approximation method has been applied to a LQR problem and H_∞ filtering problem of a cantilever array. The system was represented through a validated two-scale model. We have proposed a possible implementation of the semi-decentralized controller as a set of distributed electronic circuits. The method has been validated, and all sources of errors have been quantified. We arrive to the conclusion that the main limitation comes from the spatial mesh size h which need to be quite small to reach a good resolution. Conversely, the number M of quadrature nodes is not needed to be large. This may be interpreted in terms of analog circuit implementation by saying that a large number of resistors is needed in the circuit, and a relatively small number of global analog computations is required to get accurate results. Further applications are now possible, for instance to more complex systems, as two-dimensional arrays, and to more sophisticated optimal control laws involving Riccati equations or inequalities.

We remark the future research works in the following:

1. Complete the validation of the whole control loop: from physical domain to two-scale domain then back to physical domain.

2. Choose the control objectives for different applications, for instance apply LQR control to an array of AFMs.

3. Extend this approach to other linear optimal control problems, LQG and H_∞ control for an array of AFMs operating in contact mode or tapping mode.

4. More design problems, such as dynamics design problem and control design problem, will be solved by the toolbox SIMBAD presented in this dissertation. Hence the limitations of the current version of AFMLab will be overcomed in the new version. The method developed in this work is sufficiently general to apply to multi-physics and multi-scale modeling for a broad range of arrays of microsystems and nanosystems whose components present some (wanted or unwanted) couplings.

Appendix A

Two-scale Model Parameters and Cell Problem

A.1 Approximations in the Physical System

The two-scale approximation of the transverse mechanical displacement field is derived following a similar principle as for the *Simple Model*, but we also take into account the lateral displacements. This requires additional scaling in the in-plane displacements. Denoting by $u^P = (u_1^P, u_2^P, u_3^P)$ the elastic displacements in the model of a Kirchhoff-Love thin plate interacting with objects, the two-scale approximation is applied to (u_1^P, u_2^P, u_3^P) in the base and to $(\varepsilon^* u_1^P, \varepsilon^* u_2^P, u_3^P)$ in the cantilevers and in objects. Precisely,

$$\begin{aligned} (\widehat{u}_1^{P\epsilon}, \widehat{u}_2^{P\epsilon}, \widehat{u}_3^{P\epsilon}) &= (u_1^A, u_2^A, u_3^A) + O(\varepsilon^*) \text{ in the base and} \\ (\varepsilon^* \widehat{u}_1^{P\epsilon}, \varepsilon^* \widehat{u}_2^{P\epsilon}, \widehat{u}_3^{P\epsilon}) &= (u_1^A, u_2^A, u_3^A) + O(\varepsilon^*) \text{ in the cantilevers and in the objects.} \end{aligned}$$

Conversely, the two-scale approximation in the physical domain is

$$u \approx \overline{u}^A \text{ in the base and } u \approx (\frac{\overline{u}_1^A}{\varepsilon^*}, \frac{\overline{u}_2^A}{\varepsilon^*}, \overline{u}_3^A) \text{ in the cantilevers and in the objects.}$$

A.2 Strains and Stresses

Once u^A together with second order corrector u^B (coming from two-scale approximation of second order derivatives) are known, the strains are approximated by

$$s_{\alpha\beta}(u) \approx -\frac{x_3}{\varepsilon^{*2}} \overline{\partial^2_{y_\alpha y_\beta} u_3^A}$$

in cantilevers. In the base their expression involve u^B,

$$s_{\alpha\beta}(u) \approx -x_3(\overline{\partial^2_{x_\alpha x_\beta} u_3^A} + \overline{\partial^2_{y_\alpha y_\beta} u^B}). \tag{A.1}$$

Moreover, in case of isotropic materials, with Young modulus E and Poisson coefficient ν, plane stresses are approximated by

$$\sigma_{\alpha\beta} \approx -\frac{x_3 h_C^2 E}{24(1+\nu)\varepsilon^{*2}}(\overline{\partial^2_{y_\alpha y_\beta} u^A} + \frac{\nu}{(1-\nu)}\overline{\Delta_{\widetilde{y}} u^A}\delta_{\alpha\beta})$$

in cantilevers, and

$$\sigma_{\alpha\beta} \approx -\frac{x_3 h_B^2 E}{12(1+\nu)}[\overline{\partial^2_{x_\alpha x_\beta} u_3^A} + \overline{\partial^2_{y_\alpha y_\beta} u^B} + \frac{\nu}{(1-\nu)}(\overline{\Delta_{\widetilde{x}} u_3^A} + \overline{\Delta_{\widetilde{y}} u^B})\delta_{\alpha\beta}] \tag{A.2}$$

in the base.

A.3 Problem $\mathcal{P}^B$

The following cell problem is used to compute $\mathcal{L}^B$ in (1.14) and u^B in (A.1,A.2). For a 2×2 symmetrical matrix ζ, we say that a field w^B, independent of y_3, solves the problem $\mathcal{P}^B$ if it solves the partial differential equation,

$$div_{\widetilde{y}}(div_{\widetilde{y}}(M^{B0}(w^B))) = -div_{\widetilde{y}}(div_{\widetilde{y}}(r^B : \zeta)) \text{ in } \widetilde{Y}_B \tag{A.3}$$

with $M^{B0} = r^B : \nabla_{\widetilde{y}}\nabla_{\widetilde{y}}^T w^B$, endowed with the following boundary conditions. The free base boundary and the base-cantilever interface are subjected to the same boundary conditions

$$\begin{aligned} \nabla_{\widetilde{y}}(n_{\widetilde{y}}^T M^{B0}(w^B)\tau_{\widetilde{y}}).\tau_{\widetilde{y}} + div_{\widetilde{y}}(M^{B0}(w^B)).n_{\widetilde{y}} &= -\nabla_{\widetilde{y}}(n_{\widetilde{y}}^T(r^B:\zeta)\tau_{\widetilde{y}}).\tau_{\widetilde{y}} \\ -div_{\widetilde{y}}(r^B:\zeta).n_{\widetilde{y}} \text{and } n_{\widetilde{y}}^T M^{B0}(w^B)n_{\widetilde{y}} &= -n_{\widetilde{y}}^T(r^B:\zeta)n_{\widetilde{y}}. \end{aligned}$$

The rest of the base boundary, which is its boundary common with this of the whole cell Y, is subjected to periodicity conditions

$$w^B,\ n_{\widetilde{y}}^T M^{B0}(w^B)n_{\widetilde{y}} \text{ are } \widetilde{Y}-\text{periodic}, \tag{A.4}$$

$$\text{and } \nabla_{\widetilde{y}} w^B.n_{\widetilde{y}},\ \nabla_{\widetilde{y}}(n_{\widetilde{y}}^T M^{B0}(w^B)\tau_{\widetilde{y}}).\tau_{\widetilde{y}} + div_{\widetilde{y}}(M^{B0}(w^B)).n_{\widetilde{y}} \text{ are } \widetilde{Y}-\text{antiperiodic}. \tag{A.5}$$

Calculation of $\mathcal{L}^B$ and of $\nabla_{\widetilde{y}}\nabla_{\widetilde{y}}^T u^B$ The linear mapping which transforms the matrix ζ into the matrix of functions $\nabla_{\widetilde{y}}\nabla_{\widetilde{y}}^T w^B$ defines a linear operator denoted by $\mathcal{L}^B$,

$$(\nabla_{\widetilde{y}}\nabla_{\widetilde{y}}^T w^B)_{\alpha\beta} = \sum_{\gamma,\rho=1}^{2} \mathcal{L}^B_{\alpha\beta\gamma\rho}\zeta_{\gamma\rho}. \tag{A.6}$$

Once u_3^A is known, $\nabla_{\widetilde{y}}\nabla_{\widetilde{y}}^T u^B$ is computed using the linear operator $\mathcal{L}^B$,

$$\nabla_{\widetilde{y}}\nabla_{\widetilde{y}}^T u^B = \mathcal{L}^B \nabla_{\widetilde{x}}\nabla_{\widetilde{x}}^T u^A \text{ in } \omega \times \widetilde{Y}_B. \tag{A.7}$$

Appendix B

AFMALab: A Simulator of an Array of AFMs

AFMALab is our new developed interactive environment which is dedicated to perform various analysis for an array of cantilevers based on the two-scale model that has been presented in chapter 1. Within AFMALab environment, you can solve different kinds of model-based problems, such as modal computation, static, quasi-static and dynamic problems for an array of cantilevers. Moreover, it can be used for design optimization of arrays of AFMs by integrating with SIMBAD®. AFMALab requires less computation effort comparing with a standard Finite Element Method analysis environment, namely COMSOL®. Thanks to an easy-to-use graphical user interface (GUI), such as menus and buttons built on MATLAB® environment, it is flexible and convenient to configure and modify material properties, loads, geometry, scanner and parameters of postprocessing.

The script of AFMALab is written in the MATLAB language. It can be integrated as a toolbox into MATLAB environment. AFMALab can run on any platform supported by MATLAB. In addition, a compiled run-time version is also available which can be operated without MATLAB.

B.1 Introduction

Using AFMALab toolbox, the user can perform different types of analysis based on our two-scale model of an array of cantilevers. The following applications are available for the current version:

- Modal computation

  Compute the global eigenvalue λ^A and eigenvector ψ^A.

- Static Analysis

Solve the static problem by applying various types of loads, such as concentrated loads at tips, face loads and body loads.

- Dynamic Analysis

  Solve the dynamic problem by exciting a single cantilever with concentrated loads oscillating to a frequency, i.e. the first base eigenfrequency or the first cantilever eigenfrequency.

- Design Optimization

  A robust optimization toolbox SIMBAD is interfaced with AFMALab and provides GUI to perform optimization analysis for designing arrays of AFM before the microfabrication process.

Remark 9 *The following typographical conventions have been used throughout:*
- Sans Serif All GUI labels, for instance: Project or Model
*- **Bold** Names of buttons, such as the **OK** button.*

B.2 Graphical User Interface

This section describes the major components in the AFMALab environment. When starting AFMALab, the main interface of AFMALab appears as shown in FigureB.1.

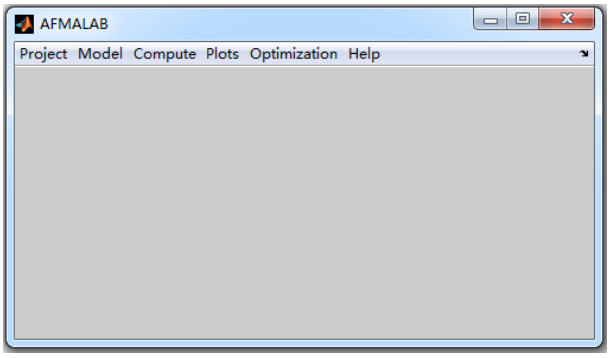

Figure B.1: The main interface of the software AFMALab.

The main interface of AFMALab includes 6 menus, namely Project, Model, Compute, Plots, Optimization and Help. We describe each sub-menu in the following sections.

Remark 10 *Most GUI objects in the AFMALab environment have a tooltip associated with them to provide a more detailed description of their function. The*

tooltip is automatically displayed when the mouse pointer is placed over the object of interest.

B.2.1 Project

Here the user can begin a new application or import an existing application into AFMALab, see Figure B.2.

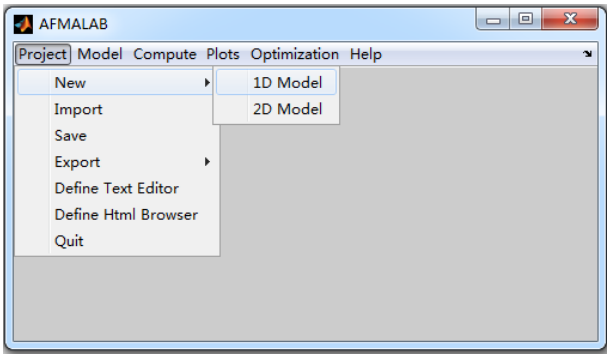

Figure B.2: Menu of Project in AFMALab

The user can also save the configuration and the result of their current application in this menu. The Export generates the geometry description file for COMSOL and the files for mode shapes, static and dynamic displacement at user-defined points.

B.2.2 Model

The Model menu allows the user to define and modify the parameters associated to the material, geometry, loads, scanner, tip-sample interaction and optical devices, as seen in Figure B.3.

Example 11 *Define and modify the material parameters, see Figure B.4*

1. *Click on menu Model, select sub-menu Material Parameters then click.*
2. *Define or modify the parameters.*
3. *Click on **OK**.*

Example 12 *Define and modify the loads, see Figure B.5*

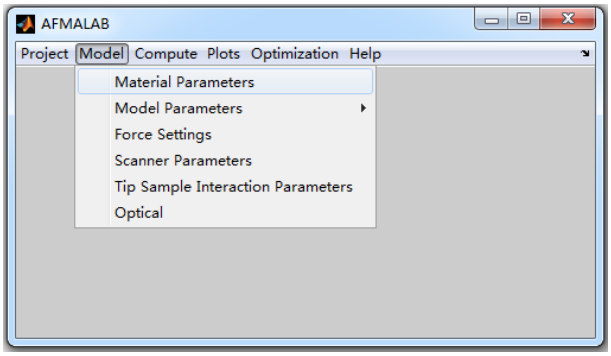

Figure B.3: Menu of Model in AFMALab

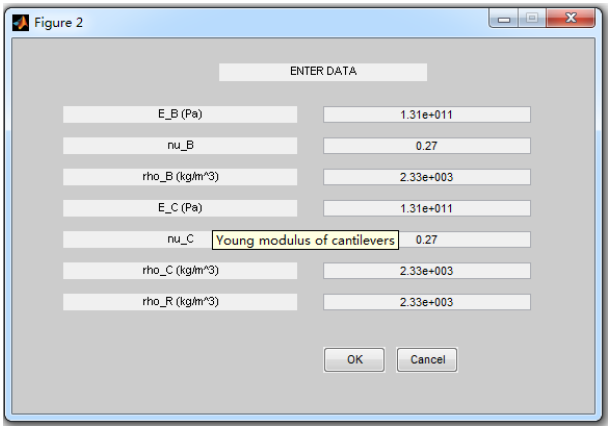

Figure B.4: Material parameter settings.

1. *Click on menu* Model*, select sub-menu* Force Settings *then click.*
2. *Define or modify the loads. The loads can be expressed as constant or as an expression of the coordinates* (x, y, z)*.*
3. *Close the edit window, the changes will be saved automatically.*

B.2.3 Compute

The Compute menu allows the user to perform the modal, static and dynamic analyses, see Figure B.6. Each analysis involved in Compute has its own sub-menu with which the user can configure and modify the parameters of the solver.

Example 13 *Modify the modal analysis solver properties and perform modal analysis.*

```
%% This file is used for setting static and dynamic forces. The forces applied to the system are functions of (t,x,y,z),
%% where t is the time variable and (x,y,z) are the space coordinates. Each force f(t,x,y,z) is expressed as a product of a function f1(t)
%% and a function f2(x,y,z): f(t,x,y,z) = f1(t)*f2(x,y,z)).
%% The function f1 and f2 can be any Matlab expression e.g. f1(t)=sin(t) and f2(x,y,z)=(y*sin(x)+z*cos(x)).
%% This choice has been made to speed-up computations and could be released in the future if necessary.
%% For static computation f1 is taken equal to 1: f1(t) = 1.

%% Body load applied to the base is function of x e.g: f(x) = sin(x). Unit: 'N/m^3'.

****** Base body force: function of (x) e.g. f(x)=sin(x) *****
0
***** Cantilever body force: function of (x) e.g. f(y)=sin(y) *****
[0 0 0 0 0 0 0 0 0 0]

%% Setting of top and bottom face loads on base and on cantilevers. Unit: 'N/m^2'.

***** Base top surface force: function of (x) e.g. f(x)=sin(x) *****
0
***** Base bottom face force: function of (x) e.g. f(x)=sin(x) *****
0
***** Cantilever top surface force: function of (x) e.g. f(y)=sin(y) *****
[0 0 0 0 0 0 0 0 0 0]
***** Cantilever bottom face force: function of (x) e.g. f(y)=sin(y) *****
[0 0 0 0 0 0 0 0 0 0]

%% Setting of point loads at the tips. Unit 'N'. With tips: applied at tip spheres.
%% Without tips: applied at the middle point of cantilever free ends

***** Point forces: function of (x,y,z) e.g. f(x,y,z)=(y*sin(x)+z*cos(x)) *****
[0 0 0 0 0 0 0 0 0 0]
```

Figure B.5: Load settings file

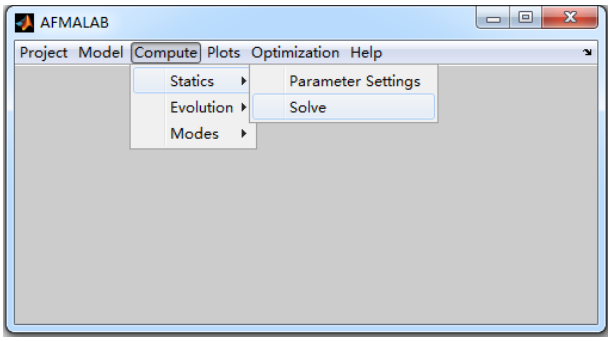

Figure B.6: Menu of Compute in AFMALab

1. *Click on menu* Compute*, select sub-menu* Parameters Settings *then click.*
2. *Keep the default parameters of modal analysis solver or modify them.*
3. *Click on* ***OK****.*
4. *Click on menu* Compute*, select sub-menu* Solve *then click it to execute the analysis.*

The user can modify the static and dynamic analyses solver properties and perform their analysis by following the same steps as indicated for modal analysis.

B.2.4 Plots

The Plots menu allows the user to display the solution of the analysis after its execution. It provides the postprocessing plots for the static solutions in two-

dimension (2D) and the modal, static and dynamic solutions in three-dimension (3D), see Figure B.7.

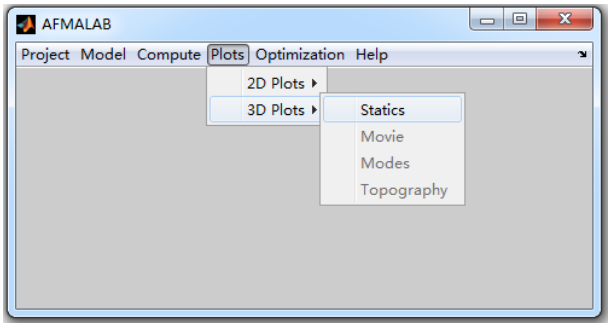

Figure B.7: Menu of Plots in AFMALab

Example 14 *Static solution plots in 2D.*

1. *Click on menu* Plots*, select sub-menu* 2D Plots*.*
2. *Click on its sub-menu* Statics*. A figure appears to display the static solutions in the base, the free end of cantilevers and the tips (in case of an array of cantilevers has tips), see Figure B.8 (a).*
3. *Click on* ***OK****.*

Example 15 *Static solution plots in 3D*

1. *Click on menu* Plots*, select sub-menu* 3D Plots*.*
2. *Click on its sub-menu* Statics*. A menu appears to let the user configure the parameters of the 3D display.*
3. *Keep the default parameters of 3D plots or modify them, then click* ***OK****, as seen in Figure B.8 (b).*

Example 16 *Modal solution plots in 3D*

1. *Click on menu* Plots*, select sub-menu* 3D Plots*.*
2. *Click on its sub-menu* Modes*. A menu appears to let the user configure the parameters of the 3D display.*

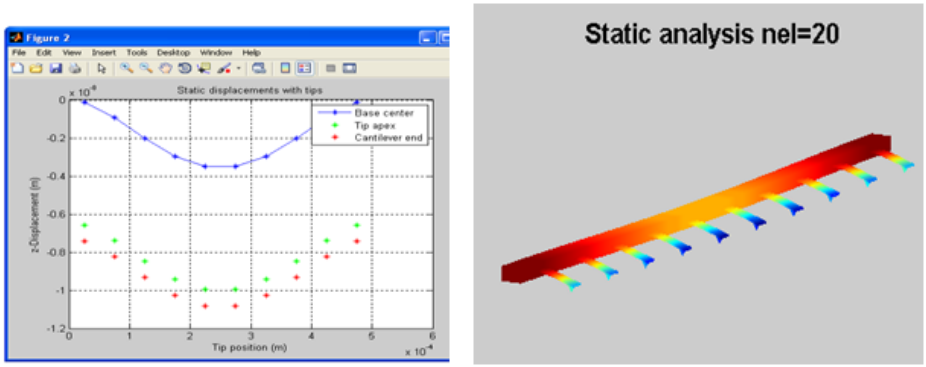

(a) (b)

Figure B.8: (a) 2D plot and (b) 3D plot of static analysis.

3. *Keep the default parameters of 3D plots or modify them, then click* ***OK****, as seen in Figure B.9.*

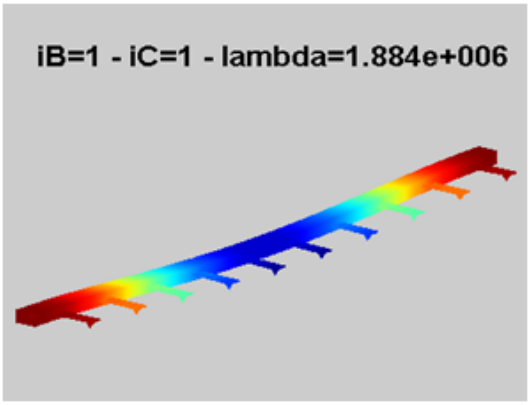

Figure B.9: Mode plot of modal analysis.

Example 17 *Dynamic solution plots in 3D.*

1. *Click on menu* Plots*, select sub-menu* 3D Plots*.*

2. *Click on its sub-menu* Movies*. A menu appears to let the user configure the parameters of the 3D movie.*

3. *Keep the default parameters of 3D plots or modify them, then click* ***OK****.*

B.2.5 Optimization

The Optimization menu contributes to the interface between AFMALab and SIMBAD which is an interactive program dedicated to simulation-based design applications. It allows the user to define different types of arrays of AFMs on a single wafer, as shown in Figure B.10.

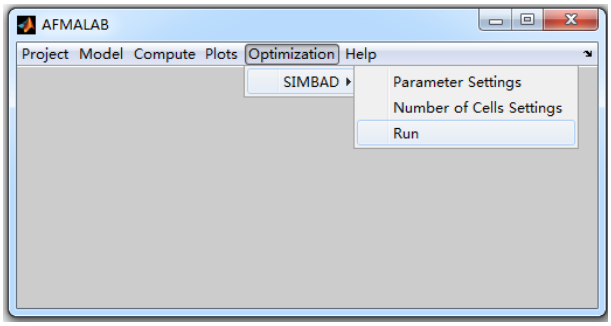

Figure B.10: Menu of Optimization in AFMALab

Example 18 *Define and modify the parameters for arrays of AFMs.*

1. *Click on menu Optimization, select sub-menu Parameters Settings then click.*
2. *Keep the default parameters of arrays of AFMs or modify them.*
3. *Click on* ***OK****.*

Example 19 *Run SIMBAD in AFMALab environment.*

1. *Click on menu Optimization, select sub-menu Run.*
2. *The main interface of SIMBAD appears, see Figure B.11. A design optimization application has been reported in section 2.3.*

B.2.6 Help

The Help menu allows the user open the AFMALab help documentations in *html* format, as shown in Figure B.12. It provides the descriptions of the main functions of AFMALab. The presentation of the two-scale approximation theory and modal description are also included in the documentation.

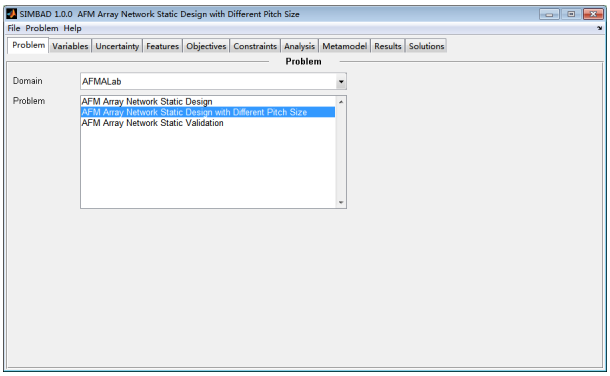

Figure B.11: Main interface of SIMBAD.

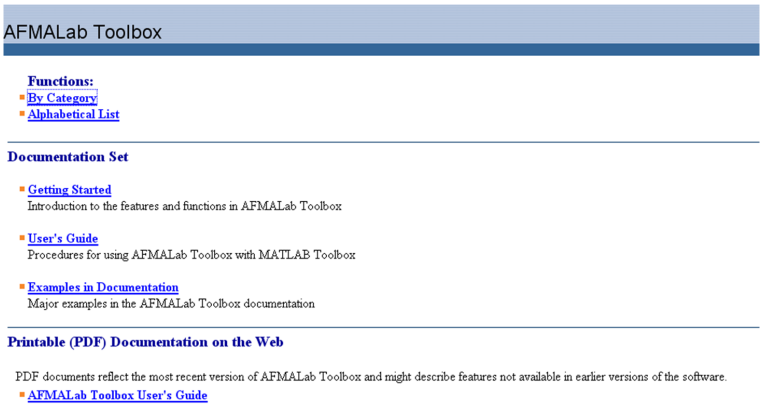

Figure B.12: The main page of AFMALab help documentation.

The AFMALab is a pre-alpha version for performing the simulations of array of cantilevers based on the two-scale model. It is designed for satisfying the basic requirements of using this tool. More sophisticated object-oriented graphics in MATLAB environment and more functionalities will be integrated into the next version of AFMALab.

Bibliography

[1] G. Binnig, C.F. Quate, and C. Gerber. Atomic force microscope. *Physical Review Letters*, 56(9):930 – 3, 1986.

[2] I. W. Rangelow, Tzv. Ivanov, K. Ivanova, B. E. Volland, P. Grabiec, Y. Sarov, A. Persaud, T. Gotszalk, P. Zawierucha, M. Zielony, D. Dontzov, B. Schmidt, M. Zier, N. Nikolov, I. Kostic, W. Engl, T. Sulzbach, J. Mielczarski, S. Kolb, Du P. Latimier, R. Pedreau, V. Djakov, S. E. Huq, K. Edinger, O. Fortagne, A. Almansa, and H. O. Blom. Piezoresistive and self-actuated 128-cantilever arrays for nanotechnology applications. *Microelectron. Eng.*, 84(5-8):1260–1264, 2007.

[3] L. Aeschimann, A. Meister, T. Akiyama, B. W. Chui, P. Niedermann, H. Heinzelmann, N. F. De Rooij, U. Staufer, and P. Vettiger. Scanning probe arrays for life sciences and nanobiology applications. *Microelectronic Engineering*, 83(4-9):1698 – 1701, 2006.

[4] P Vettiger, G Cross, M Despont, U Drechsler, U Duerig, B Gotsmann, W Haberle, M Lantz, HE Rothuizen, R Stutz, et al. The" millipede"- nanotechnology entering data storage. *IEEE Transactions on nanotechnology*, 1(1):39–55, 2002.

[5] E Eleftheriou, T Antonakopoulos, GK Binnig, G Cherubini, M Despont, A Dholakia, U Duerig, MA Lantz, H Pozidis, HE Rothuizen, et al. Millipede-a mems-based scanning-probe data-storage system. *Magnetics, IEEE Transactions on*, 39(2):938–945, 2003.

[6] A Pantazi, A Sebastian, TA Antonakopoulos, P Bächtold, AR Bonaccio, J Bonan, G Cherubini, M Despont, RA DiPietro, U Drechsler, et al. Probe-based ultrahigh-density storage technology. *IBM Journal of Research and Development*, 52(4.5):493–511, 2008.

[7] M. Lutwyche, C. Andreoli, G. Binnig, J. Brugger, U. Drechsler, W. Haberle, H. Rohrer, H. Rothuizen, P. Vettiger, G. Yaralioglu, and C. Quate. 5x5 2d

afm cantilever arrays a first step towards a terabit storage device. *Sensors and Actuators, A: Physical*, 73(1-2):89 – 94, 1999.

[8] Y.-S. Kim, H.-J. Nam, S.-M. Cho, J.-W. Hong, D.-C. Kim, and J. U. Bu. Pzt cantilever array integrated with piezoresistor sensor for high speed parallel operation of afm. *Sensors and Actuators, A: Physical*, 103(1-2):122 – 129, 2003.

[9] K. Kakushima, T. Watanabe, K. Shimamoto, T. Gouda, M. Ataka, H. Mimura, Y. Isono, G. Hashiguchi, Y. Mihara, and H. Fujita. Atomic force microscope cantilever array for parallel lithography of quantum devices. *Japanese Journal of Applied Physics, Part 1: Regular Papers and Short Notes and Review Papers*, 43(6 B):4041 – 4044, 2004.

[10] X. Yu, D. Zhang, T. Li, X. Wang, Y. Ruan, and X. Du. Fabrication and analysis of micromachined cantilever array. *Pan Tao Ti Hsueh Pao/Chinese Journal of Semiconductors*, 24(8):861 – 865, 2003.

[11] G.-W. Hsieh, C.-H. Tsai, W.-C. Lin, C.-C. Liang, and Y.-W. Lee. Bond-and-transfer scanning probe array for high-density data storage. *IEEE Transactions on Magnetics*, 41(2):989 – 991, 2005.

[12] Z. Yang, Y. Yu, X. Li, and H. Bao. Nano-mechanical electro-thermal probe array used for high-density storage based on nems technology. *Microelectronics Reliability*, 46(5-6):805 – 810, 2006.

[13] D. Bullen, S.-W. Chung, X. Wang, J. Zou, C. A. Mirkin, and C. Liu. Parallel dip-pen nanolithography with arrays of individually addressable cantilevers. *Applied Physics Letters*, 84(5):789 – 791, 2004.

[14] J.-B. D. Green and G. U. Lee. Atomic force microscopy with patterned cantilevers and tip arrays: Force measurements with chemical arrays. *Langmuir*, 16(8):4009 – 4015, 2000.

[15] Z. Yang, X. Li, Y. Wang, H. Bao, and M. Liu. Micro cantilever probe array integrated with piezoresistive sensor. *Microelectronics Journal*, 35(5):479 – 483, 2004.

[16] J. Haaheim, V. Val, J. Bussan, S. Rozhok, J.-W. Jang, J. Fragala, and M. Nelson. Self-leveling two-dimensional probe arrays for dip pen nanolithography®. *Scanning*, 32(1):49–59, 2010.

[17] I. W. Rangelow, T. Ivanov, Y. Sarov, A. Schuh, A. Frank, H. Hartmann, J.-P. Zöllner, D. L. Olynick, and V. Kalchenko. Nanoprobe maskless lithography. *SPIE Proceedings*, 7637:76370V–76370V–10, 2010.

[18] M. Napoli, Bamieh B., and K. Turner. A capacitive microcantilever: Modelling, validation, and estimation using current measurements. *Journal of Dynamic Systems, Measurement, and Control*, 126(2):319–326, 2004.

[19] S. M. Salapaka, T. De, and A. Sebastian. A robust control based solution to the sample-profile estimation problem in fast atomic force microscopy. *International Journal of Robust and Nonlinear Control*, 15(16):821–837, 2005.

[20] M. Sitti. Atomic force microscope probe based controlled pushing for nanotribological characterization. *IEEE/ASME Transactions on Mechatronics*, 9(2):343 – 348, 2004.

[21] G. Schitter, P. Menold, H. F. Knapp, F. Allgower, and A. Stemmer. High performance feedback for fast scanning atomic force microscopes. *Review of Scientific Instruments*, 72(8):3320–3327, 2001.

[22] G. Schitter and A. Stemmer. Model-based signal conditioning for high-speed atomic force and friction force microscopy. *Microelectronic Engineering*, 67-68:938–944, 2003.

[23] G. Schitter, R. W. Stark, and A. Stemmer. Fast contact-mode atomic force microscopy on biological specimen by model-based control. *Ultramicroscopy*, 100(3-4):253–257, 2004.

[24] M. Napoli, W. Zhang, K. Turner, and B. Bamieh. Characterization of electrostatically coupled microcantilevers. *Journal of Microelectromechanical Systems*, 14(2):295 – 304, 2005.

[25] A. Sarwar, P. G Voulgaris, and S. M Salapaka. On the control design and robustness analysis for high-density microcantilever arrays. *Journal of Vibration and Control*, 17(8):1195–1210, 2011.

[26] M. Lenczner and R. C. Smith. A two-scale model for an array of afmï¿½s cantilever in the static case. *Mathematical and Computer Modelling*, 46(5-6):776–805, 2007.

[27] M. Lenczner. A multiscale model for atomic force microscope array mechanical behavior. *Applied Physics Letters*, 90:091908, 2007.

[28] M. Lenczner and H. Hui. A model for two-dimensional arrays of cantilevers in the dynamic regime. Submitted.

[29] M. Lenczner. Homogénéisation d'un circuit électrique. *C. R. Acad. Sci. Paris Sér. II b*, 324(9):537–542, 1997.

[30] M. Lenczner and D. Mercier. Homogenization of periodic electrical networks including voltage to current amplifiers. *Multiscale Model. Simul.*, 2(3):359–397, 2004.

[31] D. Cioranescu, A. Damlamian, and G. Griso. Periodic unfolding and homogenization. *C. R. Math. Acad. Sci. Paris*, 335(1):99–104, 2002.

[32] P. G. Ciarlet. *Mathematical elasticity. Vol. I*, volume 20 of *Studies in Mathematics and its Applications*. North-Holland Publishing Co., Amsterdam, 1988.

[33] P. Destuynder and M. Salaun. *Mathematical analysis of thin plate models*, volume 24 of *Mathématiques & Applications*. Springer-Verlag, Berlin, 1996.

[34] B. Bamieh, F. Paganini, and M.Dahleh. Distributed control of spatially invariant systems. *IEEE Transactions on Automatic Control*, 47(7):1091–1107, 2002.

[35] F. Paganini and B. Bamieh. Decentralization properties of optimal distributed controllers. *Proceedings of the IEEE Conference Decision and Control*, 2(9):1877 – 1882, 1998.

[36] R. D'Andrea and G. E. Dullerud. Distributed control design for spatially interconnected systems. *IEEE Trans. Automat. Control*, 48(9):1478–1495, 2003.

[37] M. Kader, M. Lenczner, and Z. Mrcarica. Approximation of an optimal control law using a distributed electronic circuit: application to vibration control. *Comptes Rendus de l'Academie des Sciences Serie II b/Mecanique*, 328(7):547 – 53, 2000.

[38] M. Kader, M. Lenczner, and Z. Mrcarica. Distributed optimal control of vibrations: a high frequency approximation approach. *Smart Materials and Structures*, 12(3):437 – 446, 2003.

[39] M. Lenczner and Y. Yakoubi. Semi-decentralized approximation of optimal control for partial differential equations in bounded domains. *Comptes Rendus Mécanique*, 337:245–250, 2009.

[40] Y. Yakoubi. *Deux Méthodes d'Approximation pour un Contrôle Optimal Semi-Décentralisé pour des Systèmes Distribués*. PhD thesis, Université de Franche-Comté, Besançon, 2010.

[41] H. Hui, Y. Yakoubi, M. Lenczner, and N. Ratier. Control of a cantilever array by periodic networks of resistances. pages 1 – 6, Bordeaux, France, 26-28 April 2010. Thermal, Mechanical & Multi-Physics Simulation, and Experiments in Microelectronics and Microsystems (EuroSimE), 2010 11th International Conference on.

[42] J Polesel-Maris, L. Aeschimann, A. Meister, R. Ischer, E. Bernard, T. Akiyama, M. Giazzon, P. Niedermann, U. Staufer, R. Pugin, NF. de Rooij, P. Vettiger, and H. Heinzelmann. Piezoresistive cantilever array for life sciences applications. *J. Phys: Conf*, Ser. 61:955–959, 2007.

[43] M. Favre, J. Polesel-Maris, T. Overstolz, P. Niedermann, S. Dasen, G. Gruener, R. Ischer, P. Vettiger, M. Liley, H. Heinzelmann, and A. Meister. Parallel afm imaging and force spectroscopy using two-dimensional probe arrays for applications in cell biology. *Journal of Molecular Recognition*, 24(3):446–452, 2011.

[44] G. Allaire. Homogenization and two-scale convergence. *SIAM J. Math. Anal.*, 23(6):1482–1518, 1992.

[45] H. Hui, Y. Yakoubi, M. Lenczner, S. Cogan, A. Meister, M. Favre, R. Couturier, and S. Domas. Modeling, filtering and optimization for afm array. *Thermal, Mechanical and Multi-Physics Simulation and Experiments in Microelectronics and Microsystems (EuroSimE), 2011 12th International Conference on*, pages 1/6 – 6/6, 18-20 April 2011.

[46] D. A. Wismer and R. Chattergy. *Introduction to nonlinear optimization System.* North-Holland series in system science and engineering, 1978.

[47] R. Couturier, S. Domas, G. Goavec-Merou, M. Favre, M. Lenczner, and A. Meister. A new approach based on a least square method for real-time estimation of cantilever array deflections with an fpga. *Design, Control and Software Implementation for Distributed MEMS (dMEMS), 2012 Second Workshop on*, pages 30–37, 2-3 April 2012.

[48] M. B. Sinclair, M. P. de Boer, and A. D. Corwin. Long-working-distance incoherent-light interference microscope. *Applied Optics*, 44(36):7714–7721, 2005.

[49] F. dell'Isola, C. Maurini, and M. Porfiri. Passive damping of beam vibrations through distributed electric networks and piezoelectric transducers: prototype design and experimental validation. *Smart materials and Structures*, 13(2):299, 2004.

[50] M. Collet, M. Ouisse, M. Ichchou, M. Ruzzene, S. Moisan, JP Rigault, M. Acher, P. Collet, P. Lahire, N. Briez, et al. Semi-active optimization of 2d wave's dispersion into mechanical systems by the mean of periodically distributed shunted piezoelectric patches: a new class of adaptive metamaterials. *SPIE Smart Structures/NDE, San-Diego (CA)*, 2011.

[51] M. Collet, K.A. Cunefare, and M.N. Ichchou. Wave motion optimization in periodically distributed shunted piezocomposite beam structures. *Journal of Intelligent Material Systems and Structures*, 20(7):787–808, 2009.

[52] M. Collet, M. Ouisse, MN Ichchou, and R. Ohayon. Semi-active optimization of 2d wave dispersion into shunted piezo-composite systems for controlling acoustic interaction. *Smart Materials and Structures*, 21(9):094002, 2012.

[53] N. Ratier. Analog computing of control laws by periodic network of resistances. In *Hardware and Software Implementation and Control of Distributed MEMS (DMEMS), 2010 First Workshop on*, pages 64–71. IEEE, 2010.

[54] N. Ratier, NE Mastorakis, V. Mladenov, Z. Bojkovic, S. Kartalopoulos, A. Varonides, and M. Jha. Towards 2 d electronic circuits in the spatial domain. In *WSEAS International Conference. Proceedings. Mathematics and Computers in Science and Engineering*, number 13. World Scientific and Engineering Academy and Society, 2009.

[55] H. Hui, Y. Yakoubi, M. Lenczner, and N. Ratier. Semi-decentralized approximation of a lqr-based controller for a one-dimensional cantilever array. In *Proceedings of the 18th IFAC World Congress, 2011*, volume 18, pages 1422–1428, 2011.

[56] R. F. Curtain and H. Zwart. *An introduction to infinite-dimensional linear systems theory*. Texts in Applied Mathematics. Springer-Verlag, 1995.

[57] K. Yosida. *Functional analysis*. Classics in Mathematics. Springer-Verlag, reprint of the sixth edition edition, 1980.

[58] N. Hale, N. J. Higham, and L. N. Trefethen. Computing a^{α}, $log(a)$ and related matrix functions by contour integrals. *SIAM journal on numerical analysis*, 46(5):2505¨C2523, 2009.

[59] K.M. Nagpal and P.P. Khargonekar. Filtering and smoothing in an h_{∞} setting. *Automatic Control, IEEE Transactions on*, 36(2):152–166, 1991.

Abstract:

We establish a two-scale model both for one-dimensional and two-dimensional Cantilever Arrays in elastodynamic operating regime with possible applications to Atomic Force Microscope (AFM) Arrays. Its derivation is based on an asymptotic analysis for thin elastic structures, a two-scale approximation and a scaling used for strongly heterogeneous media homogenization. We present the method used for its discretization, and report results of its numerical validation with FEM. A robust optimization toolbox is interfaced to aid for design before the microfabrication process. A model based algorithm of static state estimation using measurement of mechanical displacements by interferometry is presented. We also synthesize a controller based on LQR methodology for a one-dimensional cantilever array with regularly spaced actuators and sensors. With the purpose of implementing the control in real time, we propose a semi-decentralized approximation that may be realized by PNR. The control approximation method is based on two general concepts, namely on functions of operators and on the Dunford-Schwartz representation formula. This approximation method is extended to solve a robust H_∞ filtering problem of the coupled cantilevers.

Keywords: Cantilever arrays, Two-scale modeling, Homogenization, Model verification, Optimization design, Interferometry measurements, Semi-decentralized control, Functional calculus, Cauchy integral formula

Résumé :

Nous établissons un modèle à deux échelles à la fois pour des matrices de cantilevers unidimensionnels et bidimensionnels en régime de fonctionnement élastodynamique avec des applications possibles aux réseaux de microscopes à force atomique (AFM). Son élaboration est basée sur une analyse asymptotique pour les structures minces élastiques, une approximation à deux échelles et une mise à l'échelle utilisée pour l'homogénéisation des milieux fortement hétérogènes. Nous présentons une méthode de discrétisation du modèle et effectuons sa vérification numérique en la comparant avec des résultats de simulation par FEM. Une boîte à outils d'optimisation robuste est interfacée avec le modèle permettant d'optimiser un design avant micro-fabrication. Un algorithme d'estimation de l'état statique combinant la mesure de déplacements mécaniques par interférométrie et le modèle a été introduit. Nous avons également synthétisé un LQR pour un réseau de cantilevers en mode dynamique comprenant actionneurs et capteurs régulièrement espacées. Dans le but de mettre en œuvre le contrôle en temps réel, nous proposons une approximation semi-décentralisée qui peut être réalisé par un PNR. La méthode d'approximation de commande est basée sur deux concepts généraux, à savoir sur un calcul fonctionnel et sur la formule de représentation d'une fonction d'opérateur de Dunford-Schwartz. Cette méthode d'approximation est étendue pour la résolution d'un problème de filtrage optimal robuste de type H_∞ de la dynamique d'un réseau de leviers couplés.

Mots-clés : Matrice de levier, modélisation à deux échelles, homogénéisation, vérification de modèle, conception par optimisation robuste, mesures d'interférométrie, contrôle semi-décentralisé, calcul fonctionnel, formule intégrale de Cauchy

SPIM

■ École doctorale SPIM 16 route de Gray F - 25030 Besançon cedex

■ tél. +33 (0)3 81 66 66 02 ■ ed-spim@univ-fcomte.fr ■ www.ed-spim.univ-fcomte.fr

UFC UNIVERSITÉ DE FRANCHE-COMTÉ